Modelling Fuel and Emissions Reduction for a WASP-Equipped Heavy Marine Transport Vessel

A.T. van Gelderen

Delft University of Technology

TU Delft

Boskalis

Modelling Fuel and Emissions Reduction for a WASP-Equipped Heavy Marine Transport Vessel

by

A.T. van Gelderen

to obtain the degree of Master of Science
at the Delft University of Technology,
to be defended publicly on Monday, March 30, 2026 at 12:45.

Report number:	MT.25/26.023.M	
Student number:	5866480	
Project duration:	May 26, 2025 – March 30, 2026	
Thesis committee:	Dr. ir. P. de Vos,	TU Delft, supervisor
	Ir. D. Noffke,	TU Delft
	Dr. A. A. Kana,	TU Delft
	Ir. M. Kom,	Boskalis
	Ing. G. Visch,	Boskalis

Cover: Boskalis Brandcenter (Modified)

An electronic version of this thesis is available at http://repository.tudelft.nl/.

TU Delft

Boskalis

Preface

This Master's Thesis is written for the partial fulfilment of the Master Marine Technology at TU Delft in cooperation with Boskalis. This document is written to help Boskalis achieve more sustainable operations. It is intended for researchers, students, and professionals working on sustainable technologies within the maritime sector. I hope the results and conclusions show valuable insights.

I started my maritime journey in 2017. After secondary school, I was eager to start my successive study after middle school in 2017: HBO Maritieme Techniek in Rotterdam. I would never have thought that I still would be a student in 2026, but my growing curiosity into the maritime world has always caused me to continue studying. I became fascinated by the energy transition and sustainable solutions in the maritime sector. The topic of wind-assisted ship propulsion has sparked my interest during this study, even though I never learned how to sail. I look forward to learning more about this and other sustainable maritime technologies in my further career.

During my time at Boskalis, I would like to acknowledge the use of an in-house Boskalis version of chatGPT (Boskalis, 2026a) and Microsoft 365 Copilot (Microsoft, 2026) to assist me with coding and to refine the grammar, structure, and clarity of the contents in the thesis. Furthermore, I used NotebookLM (Google, 2026) to improve my understanding of the literature I reviewed in this study.

I would like to thank Peter for arranging a graduation internship at Boskalis and for his kind and clear guidance. His feedback helped me to keep the right direction during my research. Furthermore, I would like to thank Deborah for her guidance throughout my process. She was always available for questions.

I would also like to thank Guido and Martijn for their guidance. They helped me with keeping track of the main purpose of my study, my understanding of specific topics within my study, and their in-depth questions always caused me to dive deeper into my work.

Last, but certainly not least, I would like to thank my friends and my family. My study friends kept me motivated and increased my interest in the maritime world. My personal friends helped me relax when I needed it, and my girlfriend always showed genuine interest in my study and supported me during busy periods. My brother always has been a role model to me, keeping me motivated as well. Most importantly, I would like to thank my parents, who have always supported me and guided me throughout my life.

Abram Teunis 'Bart' van Gelderen
Delft, March 2026

Summary

The increasing numbers of anthropogenic emissions within the maritime sector has caused a growing attention for emission-reducing technologies. The International Maritime Organization has set targets to address the climate crisis through regulatory measures for decarbonisation. This is triggering the maritime industry to reduce its emissions, leading to a transition in marine propulsion methods. A promising contributor to emission-reducing options is Wind-Assisted Ship Propulsion (WASP). A WASP system creates additional forward thrust, assisting the main engine during sailing. Modern sail technologies are in development due to the renewed interest in wind propulsion, grabbing the attention of the merchant shipping sector. Boskalis, as an operator of specialised vessels in technical operations, is also exploring emission-reducing technologies. The integration of WASP technology within the fleet and its resulting impact on fuel consumption and emissions is however difficult due to the versatility of the fleet and the technical operations of the vessels.

A fleet analysis is conducted using a multiple-criteria decision analysis which shows that the heavy marine transport and subsea rock installation vessels are interesting vessel types for WASP. A performance analysis and a general comparison of the existing WASP technologies showed that the rotor sail is a suitable technology for these vessel types. The heavy marine transport vessel fleet appears to be a more logical choice for WASP, because of its operational profile. Due to the relatively straightforward rotor sail placement options, the Triumph is chosen as a case study.

Daily reported data of ship speed and engine power, and an estimation of the propeller characteristics and other required parameters, are used to develop a 1-degree-of-freedom stead-state model for the original vessel. This model predicts the resistance and consumed fuel during a typical voyage. The required parameters for the calculation of the thrust performance of the rotor sails are estimated using data from existing literature. After picking a representative voyage using historical voyage data, the wind conditions on this route are determined using statistics. A steady-state model and a time-domain model including rotor sail forces are developed to show the impact of the rotor sails on the engine operating points of the Triumph. The steady-state model uses year-round wind conditions as input, whereas the time-domain model applies Beaufort 5–6 conditions. This information is used to calculate fuel and energy consumption during the voyage. Emission factors, as provided by the International Maritime Organization, are used to convert fuel and energy consumption into emissions.

Results indicate that the integration of rotor sails on the Triumph reduces fuel consumption and emissions. Fuel consumption and CO_2 and SO_X emissions reductions reach up to 5% for the steady-state model and 8.2% for the time-domain model, with additional reductions observed for other emission types. The difference in savings is caused by the variation in input wind conditions, with more favourable wind conditions in the time-domain model. The results suggest that the steady-state model is more suitable for estimating annual performance, while the time-domain model is suited for evaluating more specific operational scenarios.

The Triumph could benefit from rotor sail installation in terms of fuel consumption and emission reductions. However, the accuracy of the results are limited by the use of a single-degree-of-freedom model and the absence of detailed relationships between engine operating conditions and emissions. Further development is recommended to improve the accuracy of these findings, allowing for a more precise assessment of the operational and environmental impact of WASP systems.

Contents

List of Figures

List of Tables

Nomenclature

AIS Automatic Identification System. 39
AR Aspect Ratio. 28, 53
AWA Apparent Wind Angle. 4, 33, 57
AWS Apparent Wind Speed. 4, 6, 62, 63

BC Black Carbon. 19, 20, 63
BDF Backward Differentiation Formula. 66

CAPEX Capital Expenditures. 28
CFD Computational Fluid Dynamics. 17
CH_4 methane. 19, 63
CO carbon monoxide. 19, 20, 63
CO_2 carbon dioxide. 1, 15, 19–21, 63

DoF Degree-of-Freedom. 14, 16–18, 41, 59, 78, 79
DP Dynamic Positioning. 25, 36

EEDI Energy Efficiency Design Index. 60
EMSA European Maritime Safety Agency. 20

FOM Figure of Merit. 26
FPP Fixed Pitch Propeller. 37, 74

GHG Greenhouse Gas. 19, 20
GT Gross Tonnage. 33, 38

HC hydrocarbons. 19, 20
HMTV Heavy Marine Transport Vessel. 26, 27, 35–37, 43, 49, 60, 77–79

IMO International Maritime Organization. 1, 2, 14, 17, 19, 20, 52, 60
ITTC International Towing Tank Conference. 8, 15–17, 59
IWSA International Windship Association. 8

LCB Longitudinal Centre of Buoyancy. 47
LSMGO Low Sulphur Marine Gas Oil. 42

MCDA Multiple-Criteria Decision Analysis. 2, 23, 25, 26, 37, 77
MCR Maximum Continuous Rating. 38, 42, 43, 45, 50, 51, 57, 66, 68, 74
MGO Marine Gas Oil. 45, 52

N_2O dinitrogen oxide. 19, 63

NED North-East-Down. 41, 61

nm nautical miles. 16

NMVOC Non-Methane Volatile Organic Compound. 19, 63

NO nitrogen monoxide. 19, 20

NO_2 nitrogen dioxide. 19

NO_x nitrogen oxides, a group of gases including NO, NO_2, and N_2O. 19, 20, 63

NWU North-West-Up. 41, 61

ODE Ordinary Differential Equations. 66, 71

PM Particulate Matter. 19, 20, 63

PPP Performance Prediction Program. 15–18, 35, 39, 41, 59

rpm revolutions per minute. 14, 46, 56

SFOC Specific Fuel Oil Consumption. 14, 51, 75

SO_2 sulphur dioxide. 19

SO_x sulphur oxides. 19, 20, 63

TSHD Trailing Suction Hopper Dredger. 15, 20, 24

TWA True Wind Angle. 4, 62, 63, 70

TWS True Wind Speed. 4, 71

VLCC Very Large Crude Carrier. 14, 17

WASP Wind-Assisted Ship Propulsion. 1–3, 5–8, 11–21, 23, 25–29, 32, 33, 35–38, 41, 54–57, 59–65, 67–69, 71, 74–79

Symbols

Symbol	Unit	Description
$(1 + k_2)$	(-)	Form factor
A	(m^2)	Area
A_{BT}	(m^2)	Bulbous bow transverse area
A_T	(m^2)	Submerged transom area
A_{wp}	(m^2)	Waterplane area
C_{BTO}	(-)	Bow thruster coefficient
C_D	(-)	Drag coefficient
C_D	(-)	Delivered power coefficient
C_L	(-)	Lift coefficient
C_M	(-)	Midship coefficient
C_{WP}	(-)	Waterplane coefficient
C_X	(-)	Thrust force coefficient
c_B	(-)	Block coefficient
D	(N)	Drag
D_e/D	(-)	Ratio of end plate diameter to rotor sail diameter
F	(N)	Force
h^L	(kJ/kg)	Lower heating value
h_B	(m)	Height of centre of bulbous bow
I_{tot}	$(\mathrm{kg\,m}^2)$	Moment of inertia of total propulsion system
I_p	$(\mathrm{kg\,m}^2)$	Moment of inertia of propeller
I_s	$(\mathrm{kg\,m}^2)$	Moment of inertia of shaft
J	(-)	Advance coefficient
K_Q	(-)	Torque coefficient
K_T	(-)	Thrust coefficient
L	(N)	Lift
L_{oa}	(m)	Length over all
L_{pp}	(m)	Length between perpendiculars
L_{wl}	(m)	Waterline length
M_B	$(\mathrm{N\,m})$	Engine torque
M_p	$(\mathrm{N\,m})$	Propeller torque
m_f	(g)	Consumed fuel
m_{ship}	(kg)	Ship mass & added mass in surge direction
n_e	(rps)	Engine rotational speed
n_p	(rps)	Propeller rotational speed
P_B	(W)	Brake power
P_D	(W)	Delivered power
P_E	(W)	Effective towing power
P_O	(W)	Open water propeller power
R	(N)	Resistance
Re	(-)	Reynolds number
ρ	$(\mathrm{kg/m}^3)$	Density
S	(m^2)	Wetted area
S_{app}	(m^2)	Wetted area of appendages
$sfoc$	(g/kWh)	Specific fuel oil consumption
T	(N)	Thrust
T	(m)	Draft
t	(-)	Thrust deduction factor
v_A	(m/s)	Advance speed
v_s	(m/s)	Ship speed
W_e	(kWh)	Effective work
$W_{i,j}$	(-)	Global wind probability matrix
w	(-)	Wake fraction

Symbol	Unit	Description
Δ	(kg)	Displacement
η_H	(-)	Hull efficiency
η_S	(-)	Shaft efficiency
η_D	(-)	Propulsive efficiency
η_O	(-)	Propeller open water efficiency
η_R	(-)	Relative rotative efficiency
μ	$(N\,s/m^2)$	Dynamic viscosity

1

Introduction

Over recent years, attention has grown to decrease the emissions within to the maritime sector. According to the latest International Maritime Organization (IMO) greenhouse gas study, the share of maritime emissions in global anthropogenic emissions has increased from 2.76% to 2.89% from 2012 to 2018 (IMO, 2020). The increment of carbon dioxide (CO_2) emissions in the international maritime sector has been 5.6% from 2012 to 2018, and is predicted to grow even further until the year 2050. The IMO has set clear, increasingly stringent targets to address the climate crisis following these worrying emission values to finally achieve a full-scale decarbonisation by 2050. To support this transition, the IMO has implemented multiple regulatory measures. The maritime industry is now embarking on a transition to full decarbonisation for this reason. The transition has grabbed interest of multiple energy-saving technologies, of which Wind-Assisted Ship Propulsion (WASP) stands out as a particularly promising contributor to emission reductions by 2030 and is considered one of the technologies with the greatest long-term potential (IMO, 2024).

Wind propulsion is not exactly a new form of shipping propulsion. For centuries, the international shipping sector was only driven by wind propulsion, until it was replaced by steam and diesel engines during the industrial age. Due to this innovation, the shipping sector was less dependent on the weather conditions during a voyage, increasing options for the sector (Vance et al., 2026), but it came at a cost: consumption of fossil fuels leading to harmful emissions. For decades, these emissions remained largely unaddressed, but growing regulatory pressure and increased climate awareness have refocused attention on alternative propulsion strategies (IMO, 2017). This has caused the come-back of wind propulsion in the form of an assistance to the existing propulsion system (Kolodziejski & Sosnowski, 2025). Modern WASP technologies are mainly implemented in the merchant shipping sector, showing a steadily increasing number of system installations (IWSA, 2026). Various types of innovative technologies are developed, designed to optimise for different purposes with regard to the traditional sails. Examples of these are to decrease operational regard, to increase created thrust forces per area, or to decrease the required installation time. However, all systems have the same goal: to harvest wind for propulsion to decrease the need for fossil fuels during a voyage (IMO, 2024).

Boskalis is also exploring options to decrease fuel consumption and emissions within its marine operations (Boskalis, 2026b). As a Dutch company with a leading position in both the global dredging industry and the wider marine services sector, Boskalis operates a highly diverse fleet (Boskalis, 2025). The vessels often have equipment on board used during operations, or are designed for certain operations that require a large area of free deck space. The unique versatility of the Boskalis fleet makes it difficult for integrating innovative technologies such as wind-propulsion and estimating the resulting impact of this.

1.1. Aim of the research

The aim of this research is to find a suitable vessel within the Boskalis fleet for the application of WASP, and to find the resulting impact of this technology on the fuel consumption and on the emissions. The following main research question is addressed:

What is the impact on fuel consumption and emissions when retrofitting an existing heavy marine transport vessel with wind-assisted ship propulsion?

To find an answer to this question, first, a suitable vessel class within the Boskalis fleet and an appropriate existing WASP technology for this vessel class should be selected. Then, a specific vessel within the Boskalis fleet should be picked to develop a case study. The addition of a WASP system causes a deviation of usual engine operations, given that these systems contribute to the vessel propulsion. The conventional engine operations and propulsive power conversion efficiencies of this vessel should therefore be known in order to make an estimation of the impact of WASP on these operations. A representative operating profile in connection with WASP leads to an estimation of the impact on fuel consumption and emissions. The emission factors described by the IMO (IMO, 2020) are used to predict the impact of WASP on the emissions of the vessel.

The following sub-questions are raised:

1. For the Boskalis fleet, which vessel class is most suitable for integrating WASP, and which technology is optimal for that case, based on explicit criteria?
2. Which specific vessel within the selected class is most suitable to develop a case study?
3. What are the expected changes in the propulsion efficiencies when integrating WASP, and how can each of these changes be estimated?
4. Which input data are required to parameterise the propulsion chain estimates and to determine the vessel's wind-assisted engine operations, and how can these inputs be calculated for the selected case vessel?
5. Using a representative operating profile and data from previous questions, what is the predicted impact of WASP on the engine operations of the vessel?
6. Based on the impact on engine operations, what differences are predicted in exhaust emissions with and without WASP using the IMO emission factors?

1.2. Research outline

The chapter following the introduction intends to discuss relevant literature for the research questions. The contents in chapter 3 discuss an Multiple-Criteria Decision Analysis (MCDA) of the Boskalis fleet and a current WASP systems analysis. A specific case is decided in chapter 4. The development of the required components for the ship model, including WASP, is shown in chapter 5. In chapter 6, a representative shipping route is chosen, and the performance results of the vessel with and without WASP are given using a steady-state model. Results from the time-domain simulation are given in chapter 7. The conclusions of this study are discussed in chapter 8, which includes the discussion of the validity and limitations. A diagram for the outline of this study is shown in Figure 1.1.

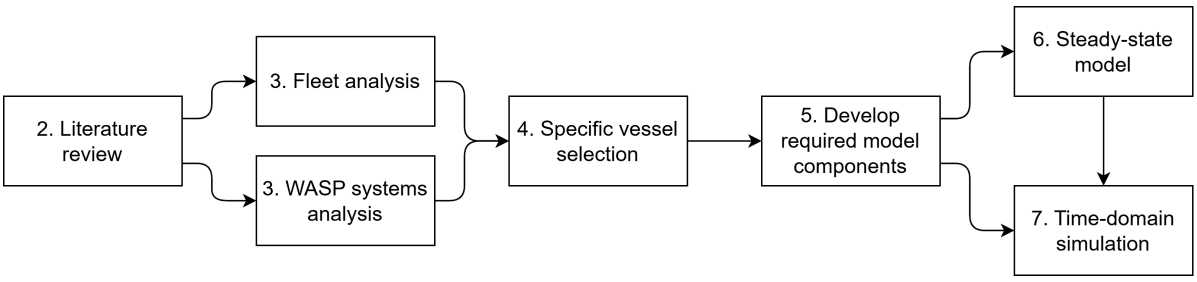

Figure 1.1: Research design diagram.

2

Literature review

This chapter discusses the state-of-the-art in the research, development, and application of WASP, selected based on the relevance to the main research question. The literature is organised by the sub-questions. Several sources are cited more than once, as these address multiple topics relevant to this study.

2.1. WASP vessels and systems

The first sub-question concerns the identification of the most suitable vessel type for the application of WASP and the specific system to be implemented. The first section of the review examines the various available WASP systems on the market, and research on the applications of systems.

Seven predominant categories of wind propulsion systems have been identified: rotor sails, hard sails, suction sails, kite sails, soft sails, turbines, and hull form design (Werner et al., 2024). The first four systems have been installed on operational sea-going ships. Rotor sails are the most adopted, whereas suction wings account for the highest number of systems on order. The systems are most commonly installed on general cargo vessels, tankers, and bulk carriers (FinOcean, 2024; IMO, 2024; IWSA, 2025), as shown in Figure 2.1. These ship types are particularly interesting due to their large, unobstructed deck areas. Figure 2.1 also shows a relatively large 'other' category; the vessels inside this category consists of different types of vessels. For instance, other than merchant ships, WASP systems have been retrofitted on a heavy lift vessel (Buitendijk, 2024b), a heavy load carrier (HANSA, 2024), and an offshore supply vessel.

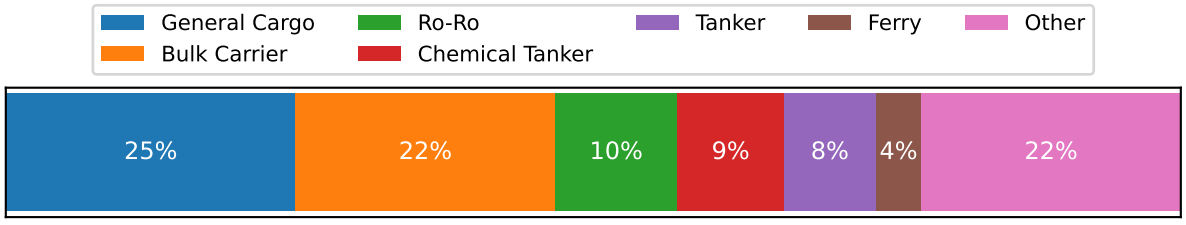

Figure 2.1: WASP systems applied on different vessels (Q3 2025). Based on IWSA (2025).

2.1.1. Physics of sailing

This section will briefly discuss the physics of sailing. The driving power of sails on a sailing vessel are generated by the apparent wind. The apparent wind is the air flow experienced by an observer in motion. The apparent wind conditions are determined using the true wind conditions and the ship speed. The relation between true wind, ship speed, and apparent wind, is shown in Figure 2.2 (Reche-Vilanova et al., 2021).

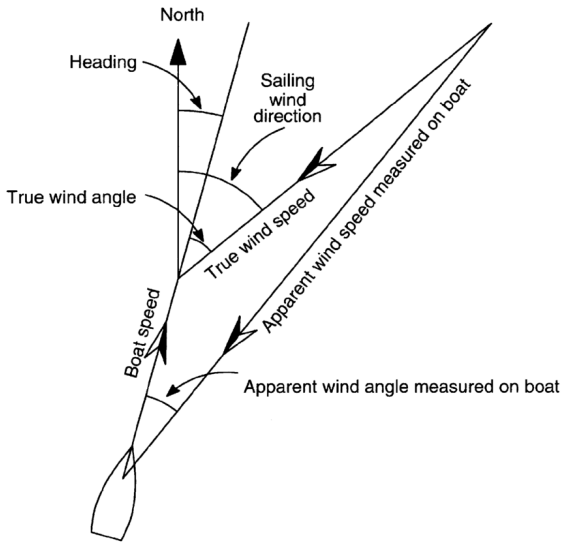

Figure 2.2: True wind and apparent wind in sailing (Chisnell, 1992).

The True Wind Speed (TWS) and True Wind Angle (TWA) can be converted into the Apparent Wind Speed (AWS) and Apparent Wind Angle (AWA) by applying trigonometry to Figure 2.2, known as the velocity triangle. The following equations convert the TWS and TWA into AWS and AWA:

$$AWS = \sqrt{v_s^2 + TWS^2 + 2 \cdot v_s \cdot TWS \cdot \cos(TWA)} \tag{2.1}$$

$$AWA = \arccos \frac{TWS \cos(TWA) + v_s}{AWS} \tag{2.2}$$

Or, using vector notation,

$$AW = [TWS \cos(TWA) + v_s, TWS \sin(TWA)]^T \tag{2.3}$$

$$AWS = \sqrt{AW(x)^2 + AW(y)^2} \tag{2.4}$$

$$AWA = \arctan\left(\frac{AW(y)}{AW(x)}\right) \tag{2.5}$$

Where AW is the apparent wind condition vector, which is used to calculate the AWS and the AWA. This velocity triangle highly depends on the ship's heading.

When the sails experience apparent wind, they generate aerodynamic forces due to the pressure differences between the leeward and windward sides (see Figure 2.3) of the sails. This aerodynamic force is composed of a lift and a drag force. Lift is defined to be the force perpendicular to the incoming flow (Equation 2.6), while drag is the force parallel to the incoming flow (Equation 2.7). The lift and drag coefficients (C_L and C_D, respectively) depend on the angle of attack (see Figure 2.3) and the sail shape. The total aerodynamic force (R, Equation 2.8) depends on the lift and drag coefficients, sail area (A), air density (ρ_{air}) and apparent wind speed.

$$L = \frac{1}{2} \cdot \rho_{air} \cdot AWS^2 \cdot A \cdot C_L \tag{2.6}$$

$$D = \frac{1}{2} \cdot \rho_{air} \cdot AWS^2 \cdot A \cdot C_D \tag{2.7}$$

$$R = \sqrt{L^2 + D^2} \tag{2.8}$$

The total aerodynamic force can be decomposed into a driving force and a side force. When sailing, the sail will always be trimmed in such a way that the lift force is in the direction of the driving force. When sailing downwind, the drag force is in the direction of the driving force, while sailing into the wind, the drag force is in the opposing direction of the driving force. The aerodynamic side force leads to drift or heel angles. This will be further explained in section 2.2.

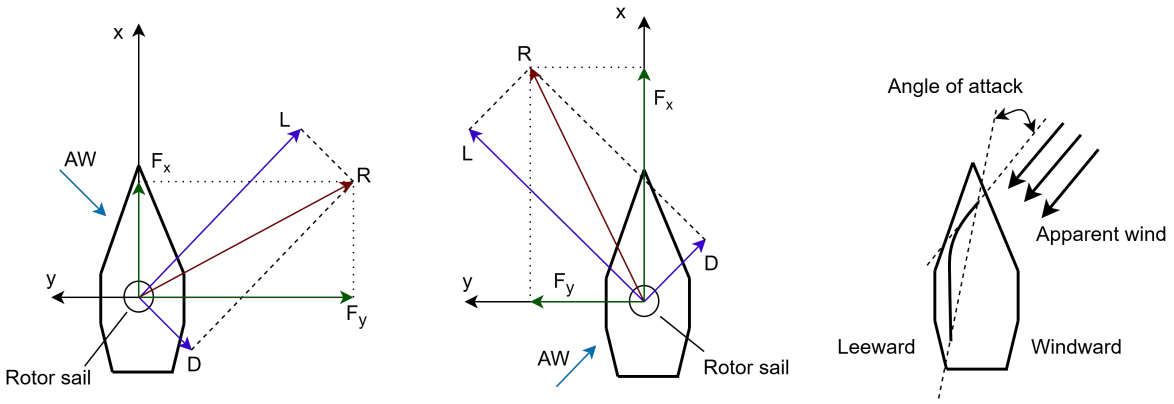

Figure 2.3: Visualisation of aerodynamic forces of a rotor sail, leeward and windward sides, and angle of attack.

The thrust force coefficient can be defined using the lift and drag force coefficients. This coefficient aligns with F_x in Figure 2.3 and is calculated using the following equation.

$$C_x = C_L * \sin(AWA) - C_D * \cos(AWA) \quad \text{when} \quad AWA <= \pi \tag{2.9}$$

$$C_x = -C_L * \sin(AWA) - C_D * \cos(AWA) \quad \text{when} \quad AWA > \pi \tag{2.10}$$

2.1.2. Wing sails

Wing sails (also called hard or rigid sails) consist of rigid materials and designs. Different types exist, with some wing sails consisting of multiple bodies with steerable flaps for enhancing the maximum lift power. The technology provides proved fuel savings on the applied vessels. The operation of these systems are the rotating of the mast such that the optimum angle of attack for given desired operation is achieved. The thrust is then generated through the effect of Bernoulli's principle. This is essentially very similar to aircraft wings (Kolodziejski & Sosnowski, 2025). This principle is illustrated in Figure 2.4a. Many companies provide different concepts of wing sails, with BAR Technologies being the market leader as of August 2024 (FinOcean, 2024). The first vessel retrofitted with two modern wing sails for WASP is the Pyxis Ocean, equipped with WindWings from BAR Technologies (BAR Technologies, 2025). The Pyxis Ocean is shown in Figure 2.4b.

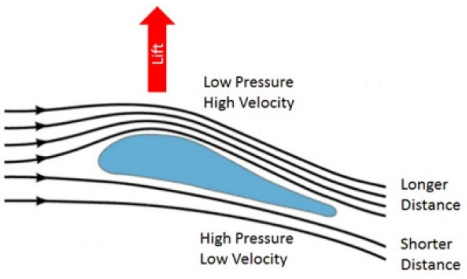

(a) Wing sail working principle (Lisitsin, 2020).

(b) Pyxis Ocean (Buitendijk, 2023).

Figure 2.4: Wing sails.

2.1.3. Suction wings

Suction wings are similar to wing sails, being vertical wing-shaped sails, and the angle of attack can be adjusted for desirable conditions. However, the suction wings include an internal fan that creates a suction force which pulls the boundary layer around the wing. This enhances the lift force significantly (Kolodziejski & Sosnowski, 2025). The parameter for the intensity of the applied suction is known as the suction coefficient. The working principle is illustrated in Figure 2.5a. This internal fan requires power input, and higher suction coefficient requires an increased fan power (IMO, 2024). There are fewer companies providing suction wings. As of August 2024, Econowind is the market leader for this technology (Econowind, 2026), and suction wings in general are the most ordered type of WASP technology (FinOcean, 2024). The MV Ankie, a cargo vessel retrofitted in 2020 with Econowind Ventifoils, is shown in Figure 2.5b.

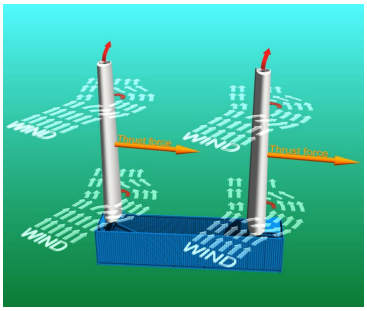

(a) Suction wings working principle (Econowind, 2025).

(b) MV Ankie (Buitendijk, 2020).

Figure 2.5: Suction wings.

2.1.4. Rotor sails

Rotor sails (also called Flettner rotors, after its inventor Anton Flettner) are vertical rotating cylinders with a top disc and possibly a bottom disc. The cylinder is spun using an electrically powered motor. The rotation rate of the rotor is known as the spin ratio, which is a dimensionless parameter defined as the ratio between the tangential velocity of the rotor surface to the AWS (Kolodziejski & Sosnowski, 2025). This parameter is identified as the most important operational controlling parameter for lift and drag generation (Lv et al., 2022). The thrust generated by this sail is created due to the principle of the Magnus effect; the wind encountering the cylinder is pulled along one side of the cylinder, creating a pressure difference, which leads to a force perpendicular to the wind direction (IMO, 2024). This principle is illustrated in Figure 2.6a. Multiple companies provide these rotor sails, which all are rotating cylinders, but with different aspect ratios, top plate sizes, and smoothness of cylinders. As of August 2024, this type of WASP technology is the most installed, with Norsepower (Norsepower, 2026) as market leader (FinOcean, 2024). An example vessel retrofitted with Norsepower rotor sails is shown in Figure 2.6b.

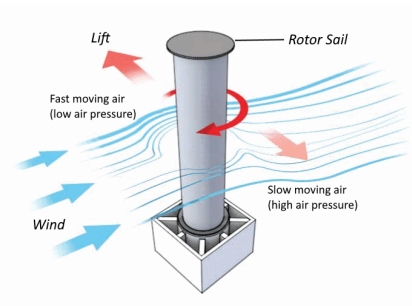

(a) Rotor sail working principle.

(b) Maersk Pelican.

Figure 2.6: Rotor sails (Patowary, 2021).

2.1.5. Other forms of WASP

Three of the seven predominant wind propulsion technologies have been discussed, which leaves four to be: soft sails, kites, turbines, and hull forms. These four types are less popular in the WASP market and will be discussed briefly.

Soft sails have been widely used for primary wind propulsion for many decades. Despite this long operational history, their use is far less common in the WASP sector for merchant vessels. Possible reasons for this include the low lift coefficient per square meters, operational expenditures, or the handling complexity compared to other technologies (Werner et al., 2024).

Kites have been applied on two vessels as of August 2024, of which one commercial vessel (FinOcean, 2024). The advantage of kites above the other WASP technology is the fact that these systems can make use of higher wind speeds found at higher altitudes compared to systems that are positioned on deck. Furthermore, kites are suitable for vessels with very limited deck space. However, the dynamic operations of the kites are complex and could lead to great effort in motion controlling. The deployment and recovery of kites also adds complexity (LR, 2024; Werner et al., 2024).

Wind turbines can be used in a number of different forms. One could be coupled directly to a generator for electricity production, or could be directly coupled to a shaft for thrust production. An advantage of wind turbines compared to other technologies is that it can produce electrical power for zero ship speed. However, the stability of the vessel should be carefully considered. As of September 2024, there are no full-scale commercial vessels sailing with wind turbines (Werner et al., 2024).

A different approach to the design of the hull form could also generate lift that could be used as an additional thrust source. A current concept design implementing this idea is the Vindskip design (Lade, 2022). The hull is shaped like a very large sail, generating thrust through the same principle as conventional sails.

2.1.6. General considerations for WASP installation

Before installing a WASP system on a vessel, several general considerations should be addressed. First, the addition of any extra equipment increases the ship weight, thereby reducing the available deadweight. Moreover, the forces generated by a WASP system can influence both the manoeuvrability and the stability of the ship. The installation also requires sufficient deck space and clearance, as the sails depend on unobstructed airflow to operate effectively. The operational efficiency of these technologies is inherently variable, as it depends on prevailing wind conditions. Most systems additionally require a power supply, which introduces further demands on onboard energy resources. Beyond the system and installation costs, integrating a WASP system into the structure and operational profile may lead to additional expenses, for example, the cost of power supply or steelwork for the foundations. Furthermore, the presence of wind-assisted propulsion systems may obstruct lines of sight and interfere with cargo-handling or evacuation operations (DNV, 2025; LR, 2024). A study on adoption barriers for retrofitting rotor sails, wing sails, and suction wings, showed that the financial incentives are the largest barrier for adopting wind propulsion (Chica et al., 2023). Another large barrier for the uptake of wind propulsion is the operational regard (IMO, 2024).

2.1.7. On the evaluation of WASP across different vessels

There is limited published literature on the evaluation of WASP technology across a fleet of various types of vessels. Hüllein (2022) conducted a feasibility study on the integration of WASP within the vessel fleet used in Norwegian aquaculture. In this study, vessel types were screened primarily based on available deck area and principal dimensions. The discussion of vessel suitability was not based on a systematic set of criteria, but on available deck space. Regarding the selection of a specific WASP system, the study favoured the Flettner rotor for its efficiency relative to sail area, referencing Lu and Ringsberg (2020) and Reche-Vilanova et al. (2021). It is worth noting that these referenced studies did not include suction wings in their comparative evaluations, which suggests that the technology selection was shaped by the set of technologies considered in those particular studies.

2.1.8. Literature reviews and main takeaways on the application of WASP systems

Although the evaluation of WASP across different vessel types is limited, sufficient information is available to allow comparisons between WASP systems applied to individual vessels. Kolodziejski and Sosnowski (2025) presented a recent review article of studies on WASP systems, the different aspects of using sail applications in the maritime industry, and the types of WASP systems. The authors concluded that most studies have been carried out on the saving potential of Flettner rotors, showing validated fuel savings. The available information of the fuel saving potential of wing sails remain limited. For suction wings, the authors found a significant deviation between predicted and reported fuel savings.

Khan et al. (2021) presented a review paper published in the Journal of the Wind Propulsion Conference. The references cited ranged from as early as 1934 to more recent works, with the majority being current at the time of publication. The review focused on three primary WASP technologies: sails, rotors, and kites. The aerodynamic principles, performance potential, and implementation challenges are discussed. The authors describe that WASP has the highest potential of energy savings amongst energy saving technologies. This same conclusion is also found in a more recent study carried out by the International Windship Association (IWSA) (IMO, 2024).

Lele and Rao (2016) identified five different wind energy strategies for ship propulsion, that are, kites, wing sails, Flettner rotors, wind turbines, and airborne wind turbines. Each strategy is accompanied by a chronological list of relevant studies. Most of the reviewed literature focused on kite-based systems.

Werner et al. (2024) is an International Towing Tank Conference (ITTC) document provided by the ITTC Wind Powered and Wind Assisted Ships Committee. This committee is relatively new and includes several prominent figures in the WASP research industry. The document outlined the tasks assigned at the previous ITTC convention in 2021. These included reviewing different WASP technologies, evaluating methods for performance prediction, and analysing long-term statistics. The committee was also tasked with developing guidelines for fuel consumption prediction, establishing performance indicators for WASP, investigating effects on propulsive factors, and formulating the ITTC for wind-propulsion ships.

Many studies have been conducted on the evaluation of different WASP systems on a vessel (Plessas & Papanikolaou, 2025; Reche-Vilanova et al., 2021; Thies & Ringsberg, 2021; Traut et al., 2014; Viken, 2022). The main takeaways from these studies are the following:

- The dimensions and number of systems influence performance (Tillig & Ringsberg, 2020; Viola et al., 2015).
- Slower vessels benefit more from WASP, as the contribution of the WASP system can be greater (Traut et al., 2014; Viola et al., 2015).
- No single non-dimensional coefficient can describe all the important characteristics of a WASP system (Reche-Vilanova et al., 2021; Traut et al., 2014; Werner et al., 2024).
- The forces generated by a WASP system depend on the vessel context (vessel type, routing), and certain aspects of WASP systems may be beneficial or unfavourable for specific vessel types (Traut et al., 2014).

2.2. Changes in propulsive efficiencies during WASP operation

Applying WASP introduces several operational challenges, as the system not only contributes to thrust but also generates a side force due to lift and drag effects. Research by van der Kolk (2020) illustrated the changes in hydromechanics and aerodynamics of a WASP-equipped vessel, and is indicated in Figure 2.7. As shown, the WASP system induces a leeway and heel angle, which alter the resistance. The prediction of the altered resistance due to leeway and heel angles will be further discussed in section 2.3. In addition, the inflow to the propeller changes, and the propeller loading differs from the design condition. These factors influence the efficiencies in the propulsion train.

The propulsion train is described by Klein Woud and Stapersma (2002) and illustrated in Figure 2.8. In this study, this chain was analysed using recent literature to identify potential changes when WASP is applied. This analysis begins at the ‘ship’ block in the upper-left corner of Figure 2.8.

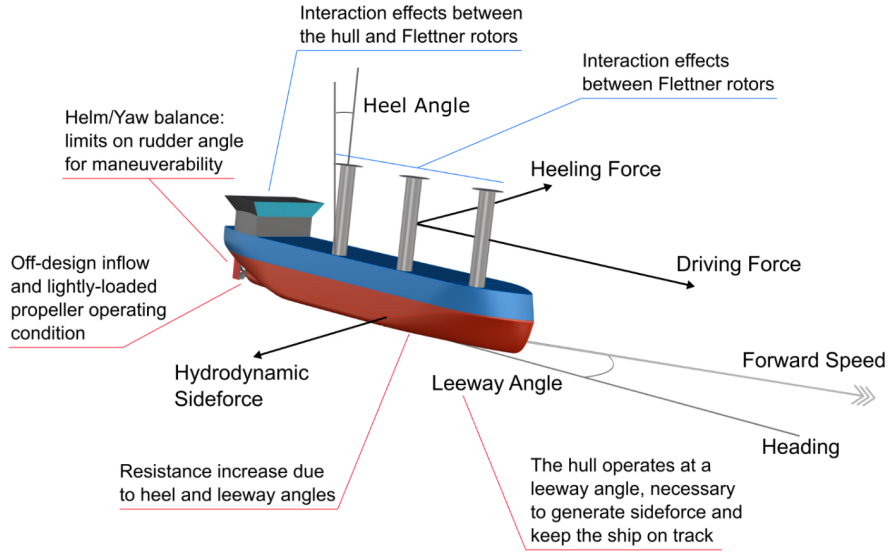

Figure 2.7: Changes in sailing while applying Flettner rotors (van der Kolk, 2020).

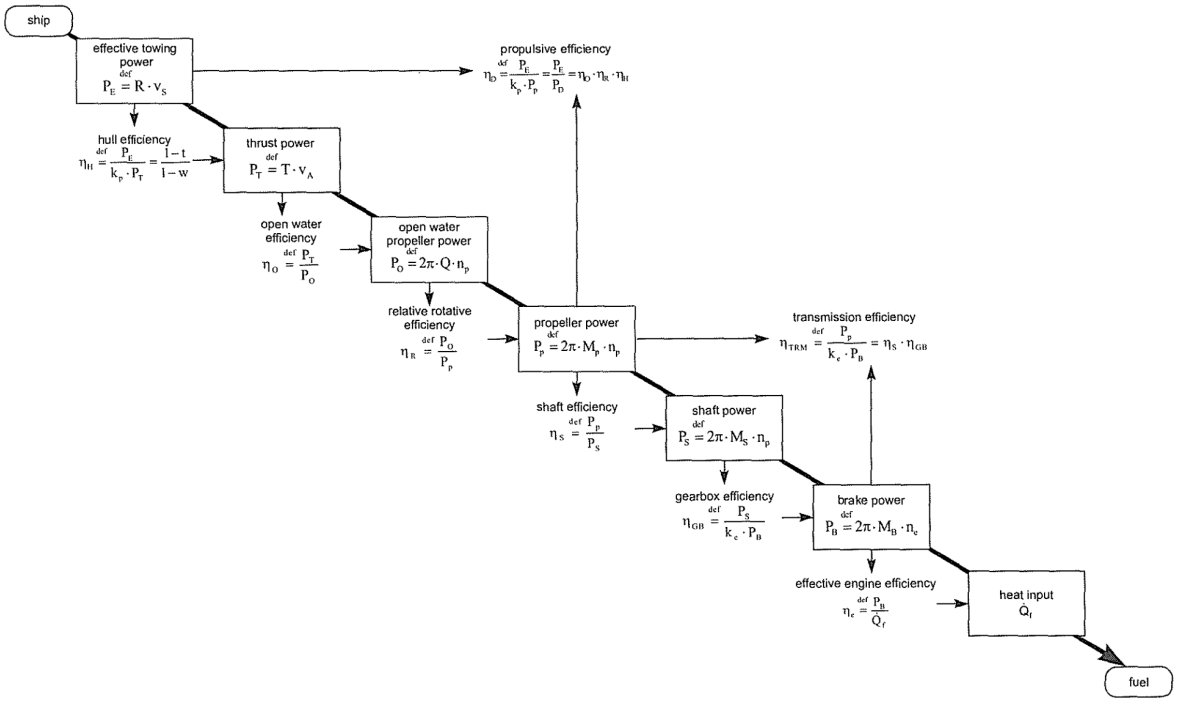

Figure 2.8: Propulsion chain (Klein Woud & Stapersma, 2002).

2.2.1. On hull efficiency

The hull efficiency is defined as the ratio of effective power to propulsive power and depends on the thrust deduction factor (t) and the wake factor (w). The thrust deduction factor represents the interaction between the operating propeller and the hull. The wake factor accounts for the reduction in water inflow velocity at the propeller compared to the ship's speed, due to the influence of the hull. The hull efficiency is calculated using Equation 2.11 (Klein Woud & Stapersma, 2002).

$$\eta_H = \frac{1-t}{1-w} \tag{2.11}$$

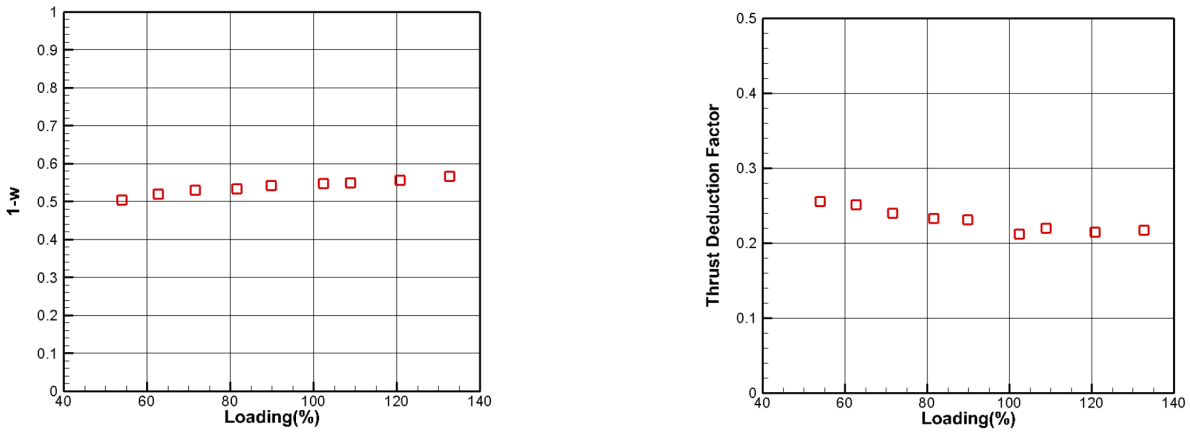

(a) Wake fraction $(1 - w)$.

(b) Thrust deduction factor (t).

Figure 2.9: Analysis of hull efficiency factors for different propeller loadings (Werner et al., 2024).

The propeller loading affects both the wake factor and the thrust deduction factor. These varying factors in propeller loading are illustrated in Figure 2.9. An increased wake factor contributes positively to hull efficiency, whereas an increased thrust deduction factor has a negative effect. The authors do not report the resulting total hull efficiency; however, they do provide the effects of t and w on the total propulsive efficiency, as discussed in subsection 2.2.4 (Werner et al., 2024).

Schot and Eggers (2019) researched the effect of leeway angle on the propulsive performance. The authors employed viscous flow calculations and model tests on three single-screw vessels and one twin-screw vessel. The results indicated that the changes in propulsive efficiency were sufficient to describe performance trends. The thrust deduction factor was held constant, as the aim was to isolate the effect on the wake factor. The authors reported that the wake field changes due to:

1. The change in mean axial velocity: when the vessel sails at a leeway angle, its velocity can be decomposed into an x- and y-component. The speed in the x-direction decreases and is described by the axial wake fraction. This fraction is further reduced by the hull shadowing effect, meaning that the leeway angle of the vessel also alters the inflow to the propeller.
2. The pre-swirl of flow due to the hull: the hull generates additional vortices in the flow, which contain pre-swirl. This changes the degree of rotation that the propeller can add to the flow.

2.2.2. On open-water efficiency

The open water efficiency (Equation 2.13) is defined as the ability of the propeller to convert shaft torque into thrust in open water. An open-water diagram can be used to determine the efficiency (η_O), the thrust coefficient (K_T), and the torque coefficient (K_Q) of a propeller, all of which are a function of the advance coefficient (J). The advance coefficient (Equation 2.12) is a dimensionless number expressing the ratio of the advance speed to the propeller's rotational speed and diameter. The thrust coefficient (Equation 2.14) represents the relationship between thrust, propeller rotational speed, and diameter. The torque coefficient (Equation 2.15) relates torque to the same parameters as the thrust coefficient (Klein Woud & Stapersma, 2002).

$$J = \frac{v_A}{n_p \cdot D_p} \tag{2.12}$$

$$\eta_0 = \frac{1}{2\,\pi} \frac{T \cdot v_A}{Q \cdot n_p} \tag{2.13}$$

$$K_T = \frac{T}{\rho \cdot n_p^2 \cdot D_p^4} \tag{2.14}$$

$$K_Q = \frac{Q}{\rho \cdot n_p^2 \cdot D_p^5} \tag{2.15}$$

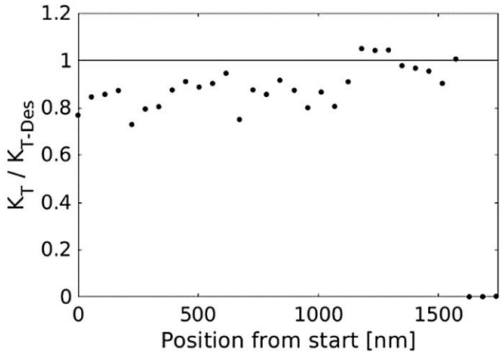

Figure 2.10: Propeller loading of WASP vessel (Tillig & Ringsberg, 2019).

Tillig and Ringsberg (2019) investigated the applicability of WASP for three different rotor sail sizes on two different vessels on a ship route in the Baltic Sea using realistic weather forecasts. The developed model in this study is based on empirical methods and standard hull and propeller series. For the ship motions, the study used a steady-state calculation to determine, for instance, the propeller load for a tanker sailing at a fixed speed. This K_T was compared to the normalised $K_{T,design}$, which represents the K_T for the tanker without WASP (see Figure 2.10). The environmental conditions varied along the route, leading to a fluctuation in WASP thrust contribution. This led to a fluctuation in the thrust force coefficient since this case assumed a constant ship speed. The results thus show that applying WASP will lead to varying propeller loadings.

The authors further noted that applying WASP could lead to backside (pressure-side) cavitation. In conventional vessels, cavitation typically occurs on the suction side due to the local pressure drop induced by the propeller (Carlton, 2018). However, the reduced propeller loading when WASP is applied may shift this pressure drop to the pressure side, potentially causing pressure-side cavitation. Conversely, Plessas and Papanikolaou (2025) examined cavitation in the context of a WASP vessel and suggested that lighter propeller loads would mitigate cavitation risks. This conclusion, however, appears to be from analyses restricted to suction-side cavitation, while the potential for pressure-side cavitation was not discussed.

Reche-Vilanova et al. (2023) developed a model to predict propeller and engine performance in calm-water conditions at a constant speed. In the model, the WASP contribution was expressed as a percentage of the required thrust to maintain the constant ship speed. The authors concluded that the open-water efficiency of the propeller increases as the net forward thrust contribution from the WASP system rises. This effect was explained by the increase in the advance coefficient resulting from reduced propeller loading, as the propeller's rotational speed decreases, which in turn leads to higher efficiency.

Figure 2.11 presents the variation in efficiency as a function of WASP contribution. Beyond a certain point, this efficiency gain ceases, as the propeller stalls. This result is also found in Eggers (2016) and in Plessas and Papanikolaou (2025).

It is well established that propeller loading influences propeller performance. A vessel operating at a drift angle can further modify the inflow conditions experienced by the propeller. For instance, oblique inflow has been shown to change open-water characteristics (Werner et al., 2024). In addition, Schot and Eggers (2019) reported that, under drift, changes in the mean axial velocity and the mean rotational components of the wake field play a dominant role in shaping the resulting propeller performance.

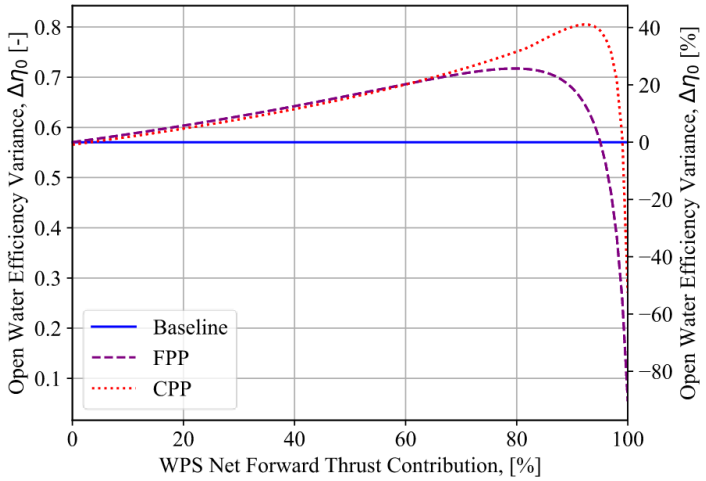

Figure 2.11: Open water efficiency variance to WASP contribution (Reche-Vilanova et al., 2023).

2.2.3. On relative rotative efficiency

The water velocity field at the propeller is non-uniform due to the influence of the hull, a phenomenon not accounted for in open-water efficiency. The relative rotative efficiency is used to represent this effect (Klein Woud & Stapersma, 2002).

Under straight sailing conditions, the relative rotative efficiency is determined by matching the measured thrust coefficient and the propeller open-water thrust coefficient. Differences between these two results in a relative rotative efficiency value. However, when sailing with a leeway angle, the hull could create a pre-swirl in the flow to the propeller, which can modify the effective rotational components experienced by the propeller. Schot and Eggers (2019) modelled this effect explicitly and reported that, for leeway angles between $-5°$ and $5°$, the resulting changes in relative rotative efficiency were minor.

2.2.4. On propulsive and transmission efficiency

The propulsive efficiency is the combined effect of hull efficiency, open-water propeller efficiency, and relative rotative efficiency. The influence of propeller loading on propulsive efficiency is shown in Figure 2.12, showing a trend of increasing propulsive efficiency with decreasing propeller loading. This behaviour can be associated with the improved propeller performance observed at lower loading conditions.

Schot and Eggers (2019) reported that, for twin-screw vessels, differences in propulsive efficiency between straight-sailing conditions and small leeway angles were generally minor. The reason for this is that the wake fields of twin-screw vessels is less altered by small leeway angles. Their analysis indicated that the effects become more noticeable at larger leeway angles, although such operating conditions are typically less relevant for wind-assisted sailing scenarios. For single-screw vessels, the study found that changes in propeller performance were more pronounced than for twin-screw vessels, and the effect increases with the apparent advance ratio. Additionally, the authors noticed that larger vessels tend to be less sensitive to leeway effects.

The transmission efficiency follows the propulsive efficiency in the propulsion train illustrated in Figure 2.8. Within the scope of this review, no literature was identified that explicitly investigates how WASP installation influences transmission efficiency. However, Schot and Eggers (2019) described that the side velocity of the water due to drift affects the propeller torque. This could lead to effects such as altered bearing loads, although these potential implications were not addressed in that study and fall outside the scope of this work. Transmission efficiency forms the link between propulsive and engine efficiency, the latter of which is discussed in the following section.

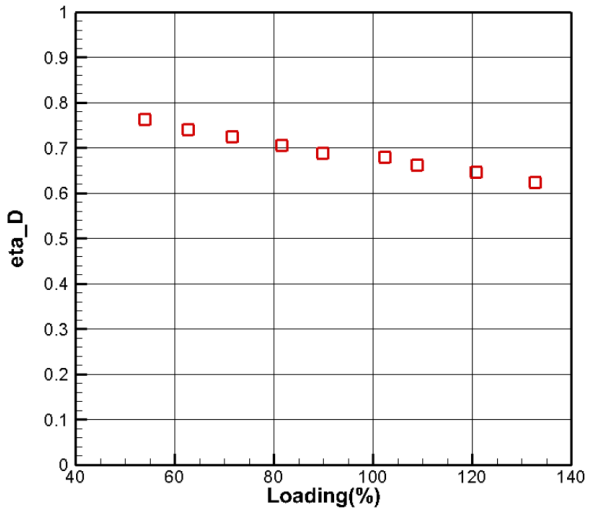

Figure 2.12: Propulsive efficiency for different propeller loadings (Werner et al., 2024).

2.2.5. On engine efficiency and operating conditions

Diesel engine efficiency is described in Klein Woud and Stapersma (2002) using the following equation:

$$\eta_e = \eta_{comb} \cdot \eta_q \cdot \eta_{td} \cdot \eta_m \tag{2.16}$$

In this equation, η_e is the total engine efficiency. The combustion efficiency (η_{comb}) represents losses due to incomplete combustion. The heat input efficiency (η_q) represents the heat that is lost inside an engine cylinder to the cylinder wall transporting its heat to the cooling water. The thermodynamic efficiency (η_{td}) accounts for the largest energy loss, representing the difference between the energy that is present in the combusted fuel, and the energy that is transferred to useful work for the engine. The mechanical efficiency (η_m) accounts for losses due to friction between engine components and pumping losses due to fuel, lubrication oil, and cooling water transportation.

The importance of modelling engine efficiency for WASP application to increase the accuracy of fuel consumption calculations is pointed out in Traut et al. (2014). However, only a limited number of studies appear to incorporate this aspect explicitly in their analyses, such as Viken (2022) and Kisjes (2017). Tillig and Ringsberg (2019) presented the engine operating points during a voyage of a tanker equipped with WASP. The authors reported that the engine occasionally operated under low power demand, and that the resulting low engine speed could approach stalling limits, necessitating further investigation. The corresponding results are shown in Figure 2.13.

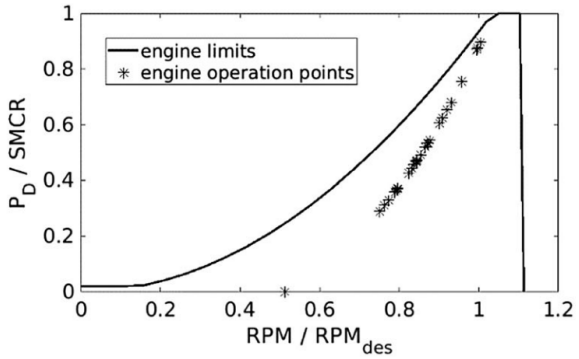

Figure 2.13: Engine loading of WASP vessel (Tillig & Ringsberg, 2019).

Eggers (2016) constructed engine load diagrams for a vessel with and without rotor sails on a selected route and included an indicative engine operating envelope. The diagrams are presented in Figure 2.14. In this figure, the operating points of the engine indicate that the titles could be inadvertently swapped. The stationary engine loads indicate that the engine works in many operating points, indicating a variable engine efficiency, especially in the wind-assisted case.

The engine operating envelope depicted in Figure 2.14 shows a lower rotational-speed limit of approximately 60 % of the maximum revolutions per minute (rpm), which is higher than what is typically observed for marine diesel engines (Klein Woud & Stapersma, 2002). This interpretation is supported by the distribution of the data points in the figure, several of which fall outside the indicated envelope, suggesting that the plotted limits may not fully represent the operational capability of the engine.

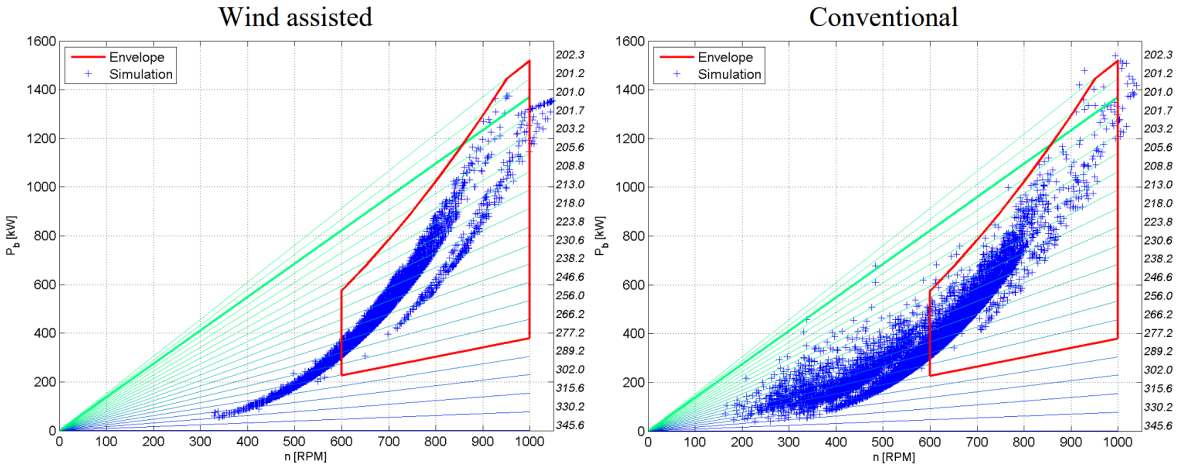

Figure 2.14: Engine load diagrams on a selected route (Eggers, 2016).

Reche-Vilanova et al. (2023) reported that the Specific Fuel Oil Consumption (SFOC) increases when the engine is partially loaded, operating under off-design conditions. However, as described earlier, they also found that the positive effect of increased propeller efficiency leads to lower fuel consumption. Based on these combined effects, the authors concluded that the overall variation in propeller and engine performance result in a positive effect. It is important to note, however, that their analysis was conducted using a 1-Degree-of-Freedom (DoF) method. This method does also not include leeway or heel effects. This modelling approach also does not account for additional resistance due to waves.

Plessas and Papanikolaou (2025) developed an engine layout diagram and a SFOC diagram for a vessel during a wind-assisted voyage. The IMO propulsion power requirements were applied to determine the necessary power for a concept design of a Very Large Crude Carrier (VLCC). As shown in Figure 2.15a the engine operating point without WASP lies at a relatively low engine operating point. This indicates slow-steaming conditions, although this is not explicitly discussed by the author. This interpretation is supported by the SFOC diagram shown in Figure 2.15, indicating an operating point below the most efficient value. The SFOC plot shows that the engine shifts to a less efficient operational condition. Furthermore, the operating points of the engine with and without sail in Figure 2.15a appear to lie on the same curve. This indicates that the author considered a constant propulsive efficiency.

The influence of dynamic engine behaviour due to WASP has received limited attention. Kuo (2020) addressed this gap by modelling the dynamic response of a diesel engine driving a fixed-pitch propeller on a rotor sail-equipped vessel. In this study, the effects of both wind and wave disturbances on the engine behaviour were considered. The results indicated that variations in engine rotational speed and torque were more sensitive to wave-induced wake disturbances than to fluctuations in wind speed. The governor was found to counteract changes in wind speed, keeping the engine speed relatively constant. Moreover, the dynamic engine operating points remained within the safe working limits during simulations, and the study concluded that the engine efficiencies under static and dynamic environmental conditions were similar.

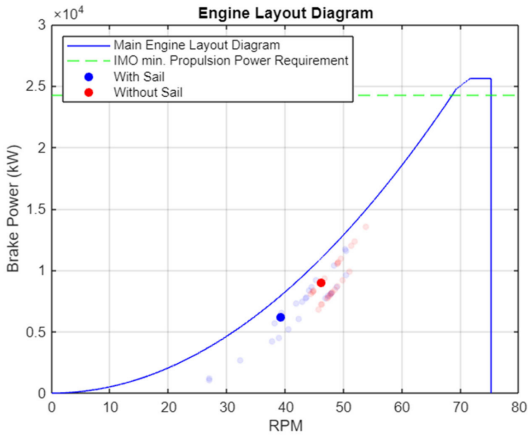

(a) Engine layout diagram.

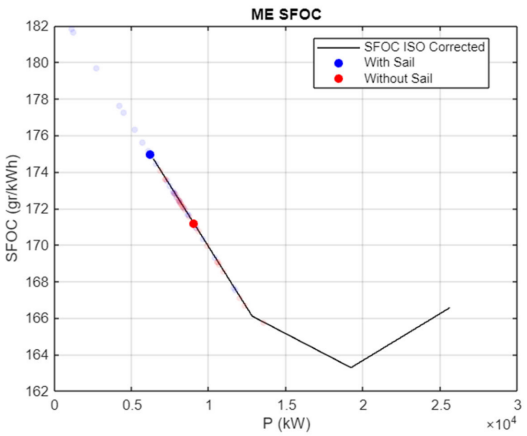

(b) Power vs. SFOC.

Figure 2.15: Engine characteristics of a ship during a journey with and without WASP (Plessas & Papanikolaou, 2025).

Outside the WASP domain, Shi (2013) investigated the influence of dynamic variations during the dredging cycle of a Trailing Suction Hopper Dredger (TSHD) on the behaviour of its energy system. Measurements conducted on board demonstrated that the diesel engine responded rapidly to changes in fuel supply during transient operating conditions. As a consequence, the study reported that the fuel consumption during these transient events was comparable to that observed under equivalent steady-state conditions.

The reviewed literature on the engine operating conditions during WASP operations shows that the operational points of the engine changes. This alters the efficiency of the engine. Furthermore, the dynamic response of the engine as an effect of WASP is not expected to result in substantial differences in engine efficiencies compared to the stationary case.

2.3. WASP performance prediction

Numerous models have been developed to predict the performance of WASP systems. However, few are commercially available or provided as open-source software (Charlou et al., 2023). Two comprehensive reviews of the existing Performance Prediction Program (PPP) methods are presented by Smeets (2024) and Werner et al. (2024). The PPPs mentioned in these studies are examined to gain insight into the type of modelling program required to address the research question.

The performance of different systems has been predicted using various forms of PPPs, using different modelling approaches, leading to varying results. However, as highlighted by Werner et al. (2024), clear guidelines on the results have only recently been established. Furthermore, discrepancies have been reported between measured and predicted performance values (Kolodziejski & Sosnowski, 2025). To address this, the ITTC specialist WASP committee was tasked with developing performance indicators to enable the comparison of WASP systems at the design stage (Werner et al., 2024):

- Power saving: Express the total propulsion power with and without WASP for the same route and speed. Assuming positive WASP thrust contribution, this indicates how much less the propulsion power the ship needs using wind propulsion. This represents the simplest means of expressing performance.
- Fuel saving: Calculate the fuel consumption with and without WASP for the same route and speed. This requires modelling the machinery efficiency.
- Energy saving: Determine the energy consumed by the propeller (propeller power multiplied by time on route) with and without WASP. This does not require modelling the engine and indicates saved propeller power.
- CO_2 saving: Calculate the CO_2 emissions with and without WASP. This can be achieved by using a conversion factor, assuming a linear relationship between fuel consumption and CO_2 emissions. Therefore, the fuel saving needs to be determined.

These different indicators require a different level of modelling effort. The power saving can be used for a straightforward idea of the impact of a WASP system compared to the total installed power. The energy consumed by the propeller shows the altered propulsive efficiency, where the fuel saving indicators shows the efficiencies in the total drive train.

Many simulation studies express the performance as a percentage of fuel savings. However, this representation could be misleading when the reference conditions are not clearly defined. This may create unclarity regarding what the reported savings are relative to, and may contribute to the discrepancies between predicted and measured fuel savings reported in Kolodziejski and Sosnowski (2025).

PPPs can be performed using different numbers of DoFs. Typically, the fuel consumption of a merchant vessel is determined using a 1-DoF method (surge). However, implementing WASP on a vessel introduces additional forces that influence the total force required to propel the vessel, as illustrated in Figure 2.7 (Charlou et al., 2023). Some studies emphasise the need for a 4-DoF approach (surge-sway-roll-yaw) when predicting the performance of WASP (Thies & Ringsberg, 2021; Tillig & Ringsberg, 2019). Others have adopted a 3-DoF method (surge-sway-yaw), assuming that the roll angle induced by the WASP systems is low (Viken, 2022; Viola et al., 2015). Reche-Vilanova et al. (2021) addressed this assumption by calculating the roll angle for a large-beam tanker using a 6-DoF model and found a maximum roll angle of 0.2 degrees. This study also reported that the difference in results between the 6-DoF and 4-DoF was minimal.

To illustrate the difference between a 1-DoF and a 4-DoF method, the results from Tillig and Ringsberg (2019) are summarised. In this study, an existing 1-DoF PPP was expanded to include sway, roll, and yaw, after which both models were used to evaluate a typical voyage with WASP. Figure 2.16 shows the predicted main engine power demand, normalised by the 4-DoF prediction without sails, for different sail areas. The comparison reveals that the 1-DoF method often overestimates the sail-assist benefit. For instance, at the start of the voyage, strong winds force the 4-DoF model to reef the sails due to excessive heel or rudder angles.

At approximately 500 nautical miles (nm), the apparent wind becomes a tailwind, resulting in negligible sail contribution. At 1300 nm, headwinds cause the rotor sails to induce drag, increasing the main engine's power demand. Accounting for heel and rudder constraints produces a maximum difference of 40% in power demand between the two models. Note that this is the same study as described in Figure 2.10, and the propeller loading variation can be recognised.

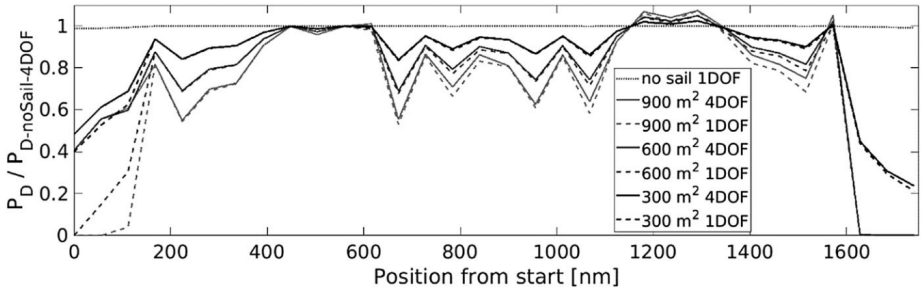

Figure 2.16: Simulation results with various sail configurations on the tanker (Tillig & Ringsberg, 2019).

Incorporating additional DoFs into the prediction programme brings both technical challenges and computational effort. In particular, accounting for the added resistance caused by the induced leeway angle remains a challenging task (Schot & Eggers, 2019; Tillig & Ringsberg, 2020). For a multiple DoF model, manoeuvrability models can be consulted to calculate induced drift resistance (Kisjes, 2017). The decision on the number of DoFs to include in a model depends on the scope and objectives of the study. To help standardise this process, the ITTC WASP Committee was tasked with proposing guidelines for the performance predictions of wind-assisted ships (Werner et al., 2024). According to the committee, estimating the expected fuel saving from a wind propulsion solution involves the following four principal steps:

1. Generating the background data required for the model input; more accurate input enables the development of more advanced models.
2. Generating models from these data to describe each sub-system's response to a change of state. For instance, the aerodynamic force of sails in different wind angles.
3. Derive steady-state force equilibrium using a PPP.
4. Conduct route studies with varying environmental conditions.

Following this, the committee defined several levels corresponding to the scope of a case study. An overview of this is given in Figure 2.17. In this table, *low fidelity* (*) methods refer to data or regression models, or lifting line methods. *High fidelity* (**) refers to case-specific Computational Fluid Dynamics (CFD), model test, or full-scale test.

While the IMO regards WASP as a large contributor to marine emission reductions, the ITTC WASP committee did not consider guidelines on the calculations of emissions for the case studies.

	Level 0	Level I	Level II	Level III	Level IV
Applicability ->	**WPS rated power**	**Early idea**	**Early business case assessment**	**Business case & Performance expectation**	**Advanced Business case & Performance expectation**
Force balance	1DOF	1DOF	3-4DOF	4DOF	4 DOF (at least)
Aerodynamics	Specific	Generic	Low/Mid fidelity*)	High fidelity**)	High fidelity
Hydrodynamics		Generic	Low/Mid fidelity	High fidelity	High fidelity
Machinery interaction			Generic SFOC + limitations	Specific SFOC + limitations	Specific SFOC + limitations
Weather on the route		EEDI or intended route	Intended route	Intended route	Intended route or weather routing
					Optional effects: e.g. ship motions and varying wind energy management optimisation

Figure 2.17: Overview of methods for prediction of power saving of wind propulsion technologies (Werner et al., 2024).

The ITTC guidelines are relatively recent (September 2024), and earlier studies have applied different argumentations for selecting the number of DoFs. Some notable statements regarding the choice of DoFs in these studies are listed below.

Plessas and Papanikolaou (2025) presented a 1-DoF method for designing a VLCC within a parametric, multi-objective optimisation framework. The authors cited Tillig and Ringsberg (2019) to justify their choice of a 1-DoF approach:

> A case study by Tillig and Ringsberg [11], examining the use of WAPSs on a tanker operating between Gothenburg and St. Petersburg in the Baltic Sea, found that fuel consumption estimates for wind-assisted vessels using a 1-DOF model differed from those using a 4-DOF model by between merely 2% (for smaller sail areas, e.g., 300 m2) to 7% (for larger sail areas, e.g., 900 m2), with the 4-DOF model providing more conservative saving predictions.

While the reported values are consistent with those presented by Tillig and Ringsberg (2019), the basis of the comparison used in Plessas and Papanikolaou (2025) requires some clarification. The underlying results in Figure 2.18 show fuel-saving estimates that are calculated relative to a no-sail reference case. For assessing differences between the 1-DoF and 4-DoF approaches, a more appropriate comparison may be found between the predictions of the two methods themselves, rather than between each method and the no-sail baseline. Consequently, for the $300\,\mathrm{m}^2$ sail, the percentage difference is $2/12 \times 100\% = 16.7\%$ with respect to the 4-DoF case. For the $900\,\mathrm{m}^2$ sail, the corresponding difference is $7/20 \times 100\% = 35\%$.

	No sail	300 m^2	600 m^2	900 m^2
1 DOF	0%	− 14%	− 23%	−27%
4 DOF	0%	− 12%	− 18%	−20%

Figure 2.18: Comparison of fuel consumption of the tanker with different sail configurations (Tillig & Ringsberg, 2019).

Reche-Vilanova et al. (2023) conducted a preliminary study on variations in propeller and engine performance with wind propulsion technologies using a 1-DoF method. The authors noted several simplifying assumptions in their modelling approach, including calm-water conditions, negligible added resistance associated with leeway, and a uniform, curl-free inflow at the propeller. They justified these simplifications explaining that the scope of the study was to examine the effects of a lightly loaded propeller and the engine on the overall propulsion system efficiency.

The analysis of the statements regarding the choice of number of DoFs in the study showed that this depends on the goal of the research. The guidelines given in Figure 2.17 shows a reasonable overview for the applicability of a certain method to achieve a certain goal. However, these guidelines lack the consideration of emissions calculations.

2.3.1. Input requirements for vessel and WASP characteristics

The review of existing PPP approaches provides insight into the parameters commonly required for predicting the performance of a vessel equipped with WASP. A concise and well-structured overview of these parameters is given by Reche-Vilanova et al. (2021). Based on the literature reviewed, the following information appears to be minimally necessary for constructing a 1-DoF PPP:

- Vessel mass.
- Hydrostatic properties.
- Hull resistance.
- WASP system thrust force.

For more advanced analyses, such as incorporating additional DoFs or accounting for other effects, more information may be required, including:

- Added resistance in waves or due to wind.
- Propeller characteristics (to account for variations in propeller efficiency).
- Aerodynamic characteristics of the superstructure.
- Rudder hydrodynamic forces.
- Added resistance in response to WASP.
- Influence of other hydrodynamic efficiencies, which include hull and relative rotative efficiency.
- Variable engine efficiency.

The following parameters are typically required to represent the WASP system itself:

- Working principles and corresponding governing equations.
- Lift and drag coefficients and system dimensions.
- Reference data for verification.
- Wind conditions.

More sophisticated prediction methods include interacting effects (Smeets, 2024), such as:

- Hull-system airflow interaction.
- System-system airflow interaction.
- Changing airflow speed over the height.

2.4. Diesel engine emissions

This section discusses the main mechanisms for different emissions caused by the combustion of fuel oil in a diesel engine, and the relation to WASP operations. A complete source for the explanation of emission mechanisms is Heywood (2018). The contents in subsection 2.4.1 are based on this work.

2.4.1. Emission mechanisms

Emissions such as CO_2 and sulphur oxides (SO_x) are governed primarily by the characteristics of the fuel itself. CO_2 is directly proportional to fuel consumption, while sulphur dioxide (SO_2) emissions are determined by the sulphur content of the fuel. These emissions can be calculated using fuel conversion factors, which depend on the type of fuel.

Other emissions also depend on the conditions in the cylinder, for instance nitrogen oxides, a group of gases including NO, NO_2, and N_2O (NO_x). The largest part of NO_x emissions is nitrogen monoxide (NO). The temperature and oxygen concentration mainly influence the NO emissions. A higher temperature and oxygen concentration generally lead to higher NO emissions. The contribution of dinitrogen oxide (N_2O) to total NO_x is relatively minor. The nitrogen dioxide (NO_2) can account for 10–30% of NO_x emissions from diesel engines, and grows for lighter engine loads.

Incomplete combustion can lead to carbon monoxide (CO) emissions. In these conditions, there is insufficient oxygen to fully oxidise the present carbon in the fuel to CO_2. Another emission resulting from incomplete combustion is Non-Methane Volatile Organic Compound (NMVOC) emissions. These are unburnt or partially burnt hydrocarbons (HC) (excluding methane (CH_4)), which under insufficient oxygen can not ignite properly. Furthermore, a low temperature at the cylinder wall engine can cause an extinguished flame, leading to unburnt fuels at these walls. Low cylinder wall temperatures are associated with light engine loading.

The mechanisms behind Black Carbon (BC) emissions, or soot, are difficult, and depend on multiple different influences. Soot formation is found to be occurring in locally fuel-rich mixtures. These conditions may arise for several reasons, but within the context of the engine operational envelope, the smoke limit of the engine is an important reason for soot formation. In this regime, despite the presence of overall excess air, the fuel sprays cannot find and mix with the remaining air quickly enough, resulting in widespread locally rich mixtures that produce excessive soot. The smoke limit of an engine is approached by an increment of the injected fuel per cycle.

The IMO provided conversion factors in IMO (2020) for the calculation of different emissions. The conversion factors are constant values that are used to calculate CO_2 and SO_x depending on the fuel type and fuel consumption, and NO_x, CH_4, CO, N_2O, and NMVOC depending on amount of energy consumed by the engine. The only constant factor that depends on the stationary engine load are the BC emissions. These guidelines also provide factors for determining Particulate Matter (PM) and CH_4. The PM emissions (PM_{10} in the document) are classified as a consequence of the amount of sulphur contents in the fuel. The CH_4 emissions are defined as the residual fraction of total hydrocarbon emissions. Within diesel engines, CH_4 are relatively low, but classified as a more potent Greenhouse Gas (GHG) compared to CO_2.

Using the IMO constant conversion factor may lead to indicative values of the emissions during a voyage, but the given information in this section shows that these values must be treated with care. The complex mechanisms behind emission formation lead to non-linear relations (except for CO_2 and SO_x) between fuel type, fuel consumption, and engine operations, and may not be accurately described using constant conversion factors.

2.4.2. On emissions under WASP operation

Although many studies acknowledge that applying WASP can reduce GHG emissions through decreased fuel consumption, relatively few quantify this. In several cases, reductions in CO_2 emissions are approximated by linearly scaling the modelled fuel savings using a fuel conversion factor (Hüllein, 2022; Reche-Vilanova et al., 2023; Viken, 2022).

Furthermore, the European Maritime Safety Agency (EMSA) reported the following (Laursen et al., 2023):

> '*As explained above, since the use of WASPs is expected to lower the ship's fuel consumption, the ship emits less GHG emissions but also other air pollutants (SO_x, NO_x, PM, etc.). The amount of air pollution that is reduced depends on how much less fuel is burned, the sulphur content of the fuel and the type of engine powering the ship.*'

This quote describes an assumption on direct proportionality between fuel savings and reductions in all air pollutants and GHG emissions. While the IMO describes constant conversion factors that imply a proportionality between consumed fuel or consumed energy and emissions (except for BC), the emission mechanisms discussed earlier suggest that this relationship is not universally valid.

Few studies in the WASP field have considered emissions other than CO_2. The study in Seddiek and Ammar (2021) considered the SO_x, CO, HC, NO_x, and CO_2 emission reductions due to WASP. The authors used constant conversion factors provided by the IMO in 2018 and 2019. These constants caused the relative emission savings to be identical to the relative energy savings.

While the study on dynamic engine operations due to WASP in Kuo (2020) did not study the resulting emissions from these operations directly, the results indicate changing in-cylinder behaviour during operations. Such changes imply that the resulting emission profile may differ from the stationary case.

The authors in Rakopoulos et al. (2009) investigated the effect of engine, load, and turbocharger parameters on the transient emissions of a diesel engine, focusing on NO and soot. The study reported that both pollutants exhibited peak values during transient load increases due to turbo lag. A sudden increase in engine load results in a reduced air-fuel equivalence ratio, leading to higher combustion temperatures that favour NO and soot formation. Furthermore, a large load increase (from 10% to 90%) requires more engine cycles to reach steady-state equilibrium, increasing the total cumulative mass of NO and soot. The authors did not study the emissions during transient load decreases.

Shi (2013) measured NO_x emissions aboard a TSHD during transient operations and found that the NO_x molar fraction followed the same general trend as engine load. The author stated that changes in NO_x molar fraction are a function of temperature, oxygen molar fraction, and pressure. For increasing loads, NO_x values were lower than in the corresponding static case. Even though higher combustion temperatures are reached during load increments, the drop in inlet pressure causes a local lack of oxygen, which results in an overall lower NO_x molar fraction. Conversely, for decreasing engine loads, the NO_x molar fraction increases.

The findings in Rakopoulos and Giakoumis (2009), resulting in increasing NO emissions during engine load increments, and the findings in Shi (2013), resulting in decreasing NO_x emissions during engine load increments, seem to be contradicting. Both studies agree that turbocharger lag causes a lower air excess ratio, leading to higher cylinder temperatures. However, the use of a constant engine speed by Shi may have caused a contradictory result from the results by Rakopoulos et al., who use a variable engine speed.

An additional conclusion from Shi (2013) is that the long-term effects of transient load changes on NO_x emissions are minimal. The increases and decreases during opposite load transitions cancel each other out, meaning that the mean NO_x emissions over extended operating periods show little to no impact from dynamic loading.

2.5. Research gap

The literature review reveals that, while wind propulsion is not a new concept, most of the systems currently under development remain in an early stage of maturity for merchant shipping application. Adoption is slowed by investment costs and operational regard. Discrepancies between predicted and reported fuel savings raise doubts about the reliability of current calculation methods, although increasingly accurate PPPs are being developed by multiple researchers. These programmes often express the performance of WASP systems in terms of fuel savings, with few studies also considering CO_2 emissions. The other types of emissions receive less attention. The guidelines on the applicability of different performance prediction methods also lack an assessment method for the emissions.

A research gap exists regarding the potential of WASP for versatile fleets consisting of special-purpose vessels, such as those operated by Boskalis. Most existing applications involve merchant ships, and only a limited number of special vessels have been retrofitted with WASP technologies. Consequently, the applicability and potential benefits of WASP for many special ship types remain unknown.

Furthermore, the existing literature consists mainly of individual case studies, with limited approaches for systematically evaluating WASP suitability across multiple vessel types. This lack of fleet-level assessment is particularly relevant for diverse operators such as Boskalis.

Outside the scope of this thesis, another research gap is identified in the relation between the affected emission characteristics of a diesel engine assisted with wind propulsion. Most recent studies on WASP focus on hydrodynamic or aerodynamic aspects, with only a few considering engine operating conditions.

3

Suitable vessel type & system for WASP

This chapter discusses the analysis of different vessel types within the Boskalis fleet for suitability of WASP. The wing sails, suction wings, and rotor sails discussed in section 2.1 will also be further analysed.

3.1. Fleet-level multiple-criteria decision analysis

An MCDA can be used to evaluate multiple conflicting criteria in decision-making. The analysis leads to a clarification in trade-offs between multiple objectives. The general approach steps for an MCDA are (Taherdoost & Madanchian, 2023):

- Identify and select the criteria
- Determine the weights of the resources
- Rank resources using a suitable method

The MCDA is defined as a distinct set of alternatives, a distinct set of criteria that are used to evaluate the alternatives, and a set of normalised weights assigning to each criterion based on importance. Different types of MCDA exist and the process of choosing an appropriate method depends on the use case. Whitcomb (1998) provides a set of different MCDA methods generally used in shipbuilding. The weighted sum method is used in this study, because of the simplicity of the formulation. This method gives quick results, but could, for complex analyses, lead to conflicting scores inside the matrix.

3.1.1. Fleet subdivision

The first step in the MCDA is to define the alternatives. For this research, the different categories of vessels inside the Boskalis fleet serve as alternatives. This fleet consists of various types of vessels, with some vessels being converted to another type during its operational time (Buitendijk, 2024a). The Boskalis equipment portal (Boskalis, 2025) and other internal information are used to divide the vessel fleet into main categories. The main categories are shown in Figure 3.1. Only the self-propelled vessel types are considered.

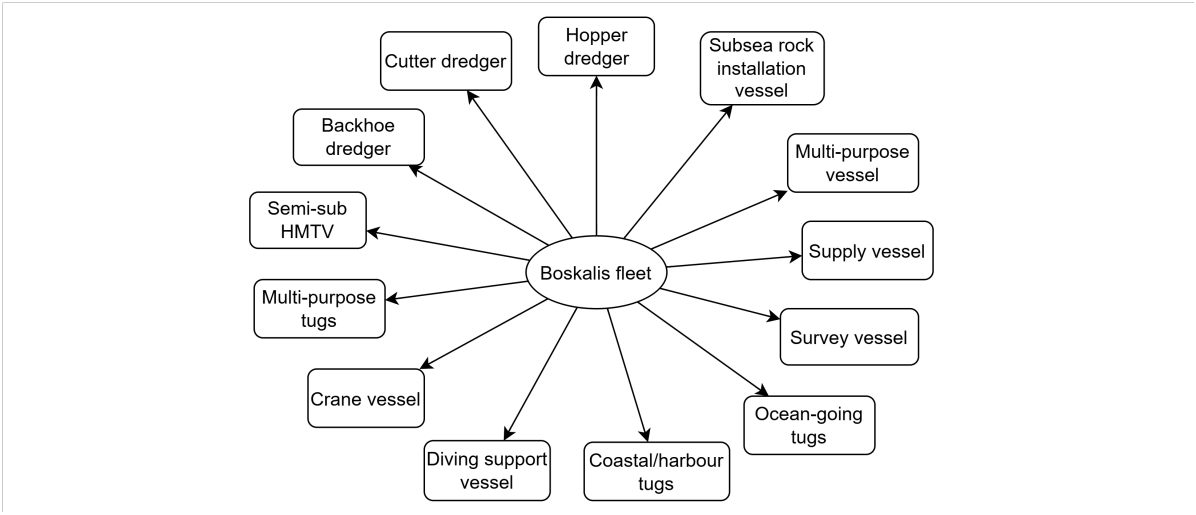

Figure 3.1: Boskalis fleet divided into various ship types.

These main categories are divided into more sub-categories to capture vessel-specific properties. Examples of these are vessel length, the equipment, or the hull form. Some discrete examples are:

- TSHD: the Medway is 121 meters long (medium) while the queen of the Netherlands is 230 meters long (large).
- Crane vessels: the Bokalift 1 is a crane vessel, while the Taklift 7 is a crane barge.
- Survey vessels: the vessels are of similar length in this class. In this example, the Braveheart Spirit is equipped with an a-frame, while the Horizon Geodrill has a drill tower. The operations of these equipment types require different installation locations on the deck.

These example vessels are given in Figure 3.2. The categorisation of every vessel is given in Appendix A.

(a) Medway

(b) Bokalift 1

(c) Braveheart spirit

(d) Queen of the Netherlands

(e) Taklift 7

(f) Horizon Geodrill

Figure 3.2: Fleet category subdivision example (Boskalis, 2025).

3.1.2. Criteria

Some common observations about factors affecting WASP technologies are an influence on the manoeuvrability, deck- and airspace, air draught, intermittence of WASP thrust, power demand, and (hidden) costs (LR, 2024). The criteria used in the MCDA method could therefore be extensive, but this would defy the use of a simple method. Only the effectiveness of the WASP system and the operational interference of such a system are considered. These are the main categories of criteria. The main categories are subdivided in criteria. This is shown in Figure 3.3.

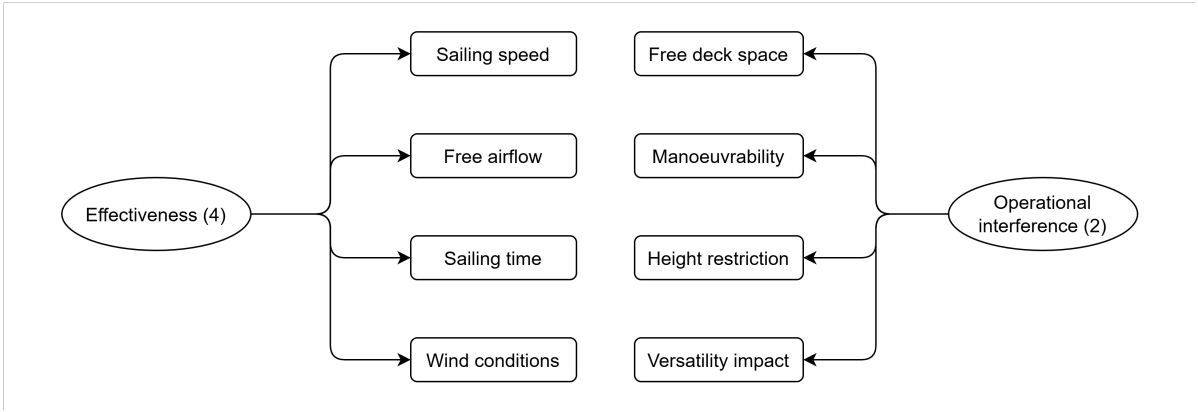

Figure 3.3: Criteria used for MCDA. Effectiveness weighs more heavily compared to operational interference.

The effectiveness and operational interference are both subdivided into four criteria.

- Effectiveness:
  - Sailing speed: a slower sailing vessel could benefit more from WASP since the apparent wind conditions will be more favourable for thrust production more often. Also, the power contribution of the system can be larger.
  - Free airflow: the WASP system works best in undisturbed airflow. Large equipments could for instance disturb this airflow. Disturbed airflow decreases the effectiveness of the system.
  - Sailing time: a vessel that could benefit the most from WASP is one that sails most of the operational time. A ship that remains stationary does not benefit from thrust production (assuming that a WASP system cannot be used during Dynamic Positioning (DP) operations).
  - Wind conditions: an inland vessel encounters lower wind speeds more often compared to a sea-going vessel.
- Operational interference:
  - Free deck space: a vessel with much free deck space has more options for the placement of new equipment, which makes it easier to assign a location where the operational interference is minimised.
  - Manoeuvrability: a WASP system will impose forces on the ship, influencing stability and manoeuvrability. A ship with a large mass moment of inertia suffers less from this effect.
  - Height restriction: a WASP system could negatively influence vessels that operate in areas with height restrictions.
  - Versatility impact: the strength of some vessels lies in the option to purposely fit a deck layout specifically for a project. This is influenced when a new type of equipment is added.

The weights of the effectiveness and operational interference are shown in Figure 3.3 (4 for effectiveness, 2 for operational interference). The effectiveness has a higher weight compared to operational interference. The effect on the operations of the vessel can be changed by considering multiple WASP system design concepts. There is some leverage on the deck layout; the sail system can be placed

such that the operational interference is minimised. The effectiveness of the sail is determined by external influences. For this reason, the effectiveness has a higher score compared to the operational interference.

Scores within the matrix are evaluated with the help of multiple professionals within Boskalis. Scoring examples are given in Figure 3.4. For instance, a semi-submersible Heavy Marine Transport Vessel (HMTV) (Figure 3.4a) has a higher score in free airflow compared to a large cutter dredger (Figure 3.4d) due to the lower chance in disturbed airflow. A barge class crane vessel (Figure 3.4b) has a lower score on free deck space compared to a medium class backhoe dredger (Figure 3.4e). A vessel class crane vessel (Figure 3.4c) has a lower score on versatility impact compared to a drilling survey vessel, because the mission of the survey vessel remains the same throughout different projects, while the deck layout of the crane vessel is very likely to change while switching projects.

One particularly difficult criterion to score is the wind conditions of a vessel. The self-propelled fleet of Boskalis consists largely of special purpose vessels whose operational locations vary substantially between projects and can be situated virtually anywhere worldwide. As a result, the wind environment experienced by each vessel is highly project-dependent rather than route-dependent, making it difficult to characterise with a single representative wind profile. Therefore, most ocean-going vessels have identical wind conditions scores.

(a) Semi-sub HMTV

(b) Crane vessel — barge

(c) Crane vessel — vessel

(d) Cutter dredger — large

(e) Backhoe dredger — medium

(f) Survey vessel — drilling

Figure 3.4: Category scoring example: free airflow (a & d), free deck space (b & e), versatility impact (c & f) (Boskalis, 2025).

These criteria exclude installation and operational costs, the main barrier to adopting WASP (IMO, 2024). Although capital costs can be estimated, operational costs and earnings are case-dependent, and a more expensive system may ultimately yield higher returns (Chica et al., 2023). Because these costs are highly uncertain in a simple MCDA, they are not considered.

The criteria also do not consider vessel-specific properties, such as vessel age and propulsion system layout. This is deemed to be less interesting in this stage of the project while the goal is to find an interesting vessel subtype for application of WASP.

The scoring of alternatives for each criterion is subjective and in principle, the discussion on this can be extended indefinitely. The scorings in the matrix are determined in close consultation with Boskalis professionals, and is deemed to be sufficiently correct for further analysis. The MCDA is given in Appendix B.

3.1.3. MCDA results

The result of the MCDA is a Figure of Merit (FOM), which can be used to rank the alternatives. The normalised FOM is given in Figure 3.5. Only the vessel subtypes with a normalised score higher than 0.8 are given in the figure. The total list with scores is given in Appendix C.

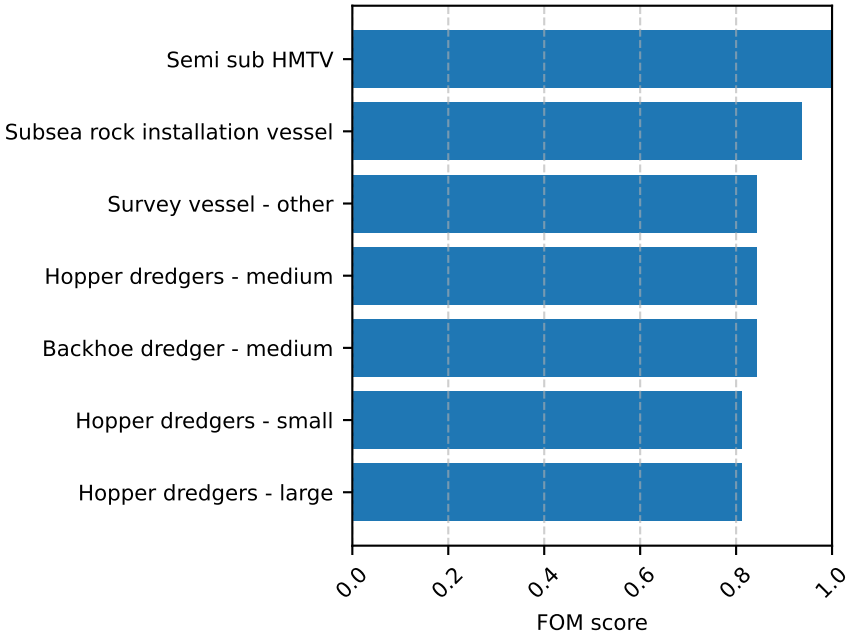

Figure 3.5: FOM scores from MCDA for highest-scoring vessel types.

Figure 3.5 indicates that the HMTV fleet is the most suitable type for WASP application according to the used method. This vessel type scores high in all criteria, except for the versatility impact, where the lowest score is given. The second vessel type is the subsea rock installation vessel, which in turn scores lower in all categories compared to the HMTV vessels, but high for the versatility impact. The survey vessels in this list are the ones that do not have signature equipment installed on deck. On this vessel type, it is relatively easy to fit new equipment, and the versatility impact is low. The medium backhoe dredger vessel type (Figure 3.4e) is one that came as a surprise in this list. It scores high for sailing speed since these vessels are very slow, and do not have much equipment on deck compared to the other backhoe dredger types, which makes it more favourable. At last, all hopper types are in the list. The medium type is scoring higher compared to the others. This vessel type is often operating along the Dutch coast, where wind conditions are favourable for WASP, since the wind will be sideways with respect to the vessel most of the time.

The HMTV and subsea rock installation fleets are most interesting according to the analysis. After checking with Boskalis' own professionals working more closely with the operations of these vessels, it is decided that there are no true showstoppers to apply WASP on either of these vessels. Therefore, no solid reason can yet be found to pick one of the types for further analysis. The choice for the specific vessel case will further be discussed in chapter 4.

3.2. WASP systems comparison

This section discusses a closer analysis of the wing sails, suction wings, and rotor sails. First, the general properties of the sails will be compared. After this, the performance of the sail types will be analysed by comparing lift and drag coefficients.

3.2.1. System specific properties

The literature review shows that the wing sails, suction wings, and rotor sails are all applied in practice. The fuel savings due to rotor sails are reported, but the data on wing sails and suction wings is limited to simulations or very few trial data (Kolodziejski & Sosnowski, 2025).

In general, the Capital Expenditures (CAPEX) for a suction wing is lower compared to a wing sail or rotor sail. This could make the choice for a suction wing easier since the investment barrier is lower. However, the CAPEX also depends on the type of system installation. For instance, to decrease cargo handling constraints, a shipowner could consider a foldable system (Chica et al., 2023).

The sizes and weights of the different systems also impose important differences. For instance, the wing sails are larger compared to suction wings or rotor sails (the reason for this will be discussed hereafter), which would increase the heeling moment of this system. This also means an increasing installation costs, since the foundation for this system is likely to be subjected to higher stresses due to the higher centre of effort. This also makes a wing sail less practical when it comes to bridge visibility.

The general differences between the wing sails, suction wings, and rotor sails are given inTable 3.1. The literature review reveals information about the maturity and the reported fuel savings of these technologies. This table also shows information about lift and drag. This is discussed in the following section.

Table 3.1: WASP system general properties.

Aspect	Wing Sail	Suction wing	Flettner rotor
Maturity of technology	+	+	++
Reported fuel savings	+	+	++
CAPEX	+	++	+
OPEX	++	+	+
Heeling moment	+	++	++
Maximum lift	+	++	++
Lift over drag	+++	++	+

3.2.2. Lift and drag coefficients

The lift and drag for different WASP systems are compared to show the possible thrust contributions of these. The coefficients are all compared by means of the 2-dimensional values; this means that the effects of the profile ends of the systems have been disregarded. In other words, the system designs are assumed to have an infinite Aspect Ratio (AR). This means that the lift coefficients will be overestimated and the drag coefficients underestimated. This eliminates the need for system dimensioning and gives a preliminary overview of performance differences across various WASP system designs.

Wing sails with flap

Firstly, wing sails will be analysed. The wing sail manufacturers provide various designs. Two leading wing sail providers are OceanWings (2026) and BAR Technologies (2025). OceanWings' wing sail consists of a two-element wing design, while BAR Technologies' wing sail consists of a three-element wing design. The advantage of a multi-element wing sail compared to a one-element wing sail is that the camber can be varied by controlling the angles of the flaps. This increases the lift of the system.

The lift and drag coefficients given in Kramer et al. (2016) are used to show the coefficients of a two-element wing sail with various flap angles for different angles of attack. The authors used a design with a leading element based on the NACA 0020 profile and the trailing element based on the NACA 0015 profile. They varied the flap angle from 0° to 15°. The flap angle significantly improves the lift coefficient as shown in Figure 3.6. The increasing flap angle also shows an increasing drag coefficient, leading to lower lift/drag ratios at higher flap angles.

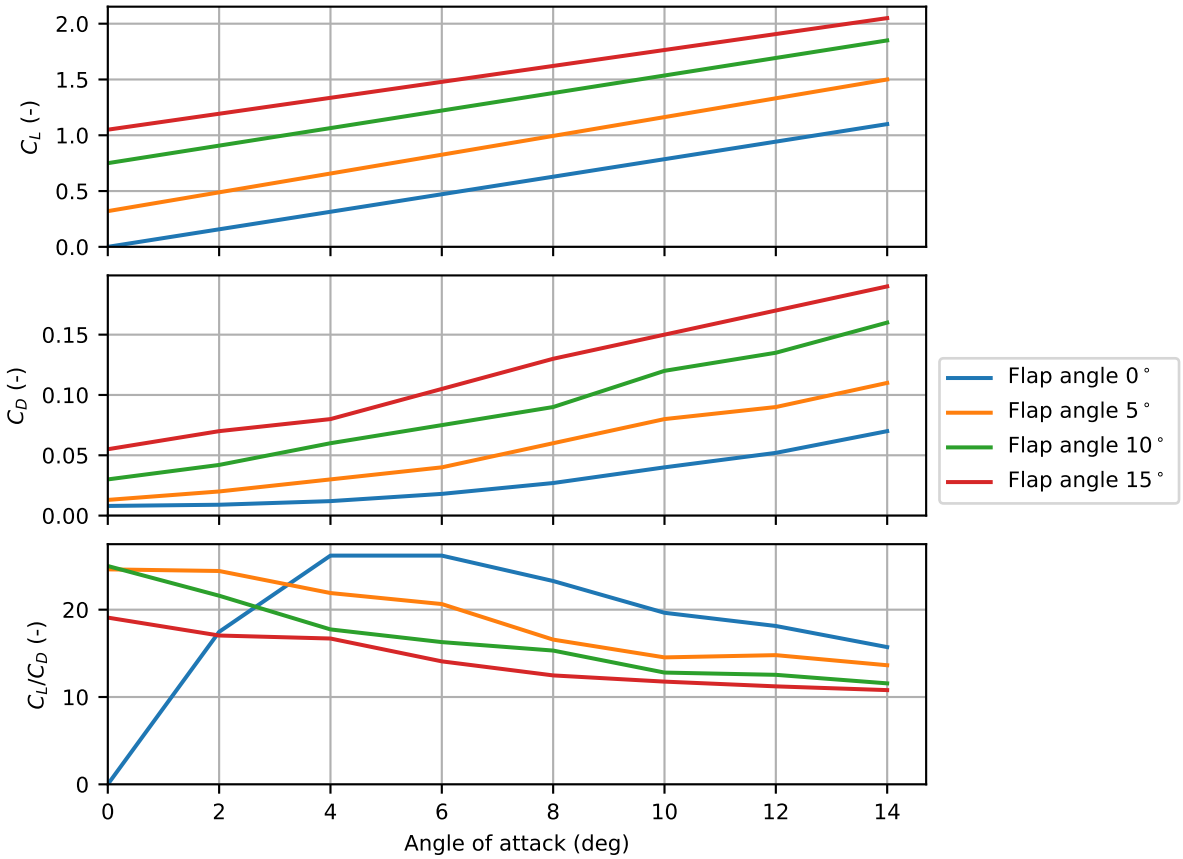

Figure 3.6: Wing sail lift, drag, lift/drag. Based on Kramer et al. (2016).

A flap angle of 15° is assumed for comparison to the other WASP systems, further discussed in subsection 3.2.3. The lift coefficient, drag coefficient, and lift/drag are given in Figure 3.7. The maximum lift for this two-element wing is used for further analysis, which is indicated in the figure. It should be noted that the scale of the different items, which is given in the legend.

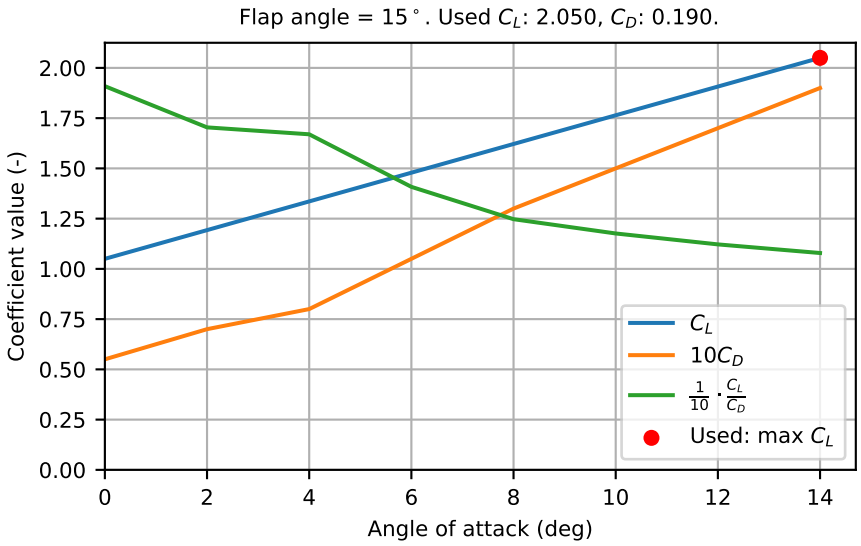

Figure 3.7: Used wing sail with flap coefficients for analysis. Note the scale of the elements, given in the legend. Based on Kramer et al. (2016).

Wing sail NACA profile

A single-element wing sail is also analysed for clarification in the difference between a two- and single-element wing sail. A NACA 0015 profile is used for this. The data for this specific profile is publicly available (Airfoil Tools, 2025). A comparison of the coefficient values in Figure 3.7 and Figure 3.8 shows that the flap imposes a larger lift coefficient with the cost of a lower lift/drag ratio. The maximum lift coefficient used for further comparison is also indicated in Figure 3.8.

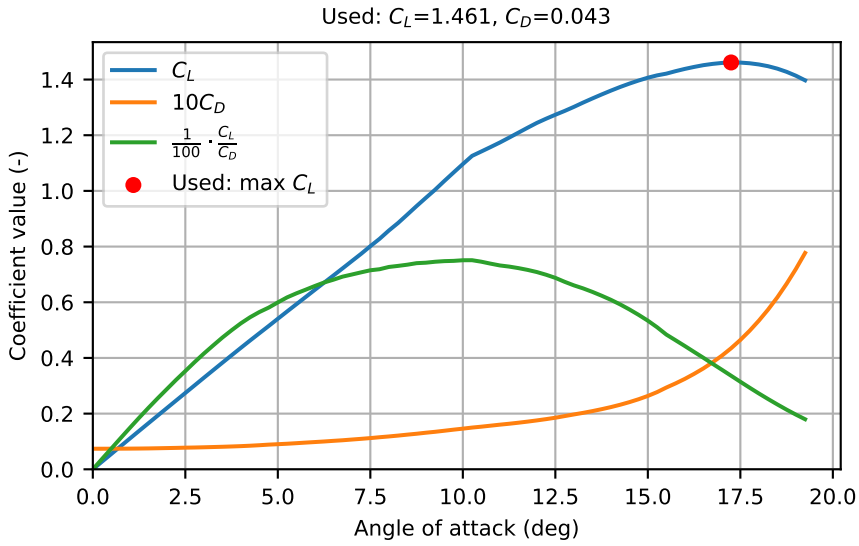

Figure 3.8: Wing sail NACA profile: lift, drag, lift/drag ratio. Based on Airfoil Tools (2025).

Suction wings

The lift and drag coefficients of the suction wings are reproduced from Charrier et al. (1985). The authors provided two figures: one showed the lift coefficient against different angles of attack, and one showed the lift coefficients against drag coefficients. Both these figures showed results for different suction coefficients. The reproduced graphs are given in Figure 3.9.

Figure 3.9 shows that, for a fixed suction coefficient, the lift coefficient increases almost linearly up to the stall point. The figure also indicates that higher suction coefficients delay the stall point to larger angles of attack. Comparing this behaviour with Figure 3.6 or Figure 3.8 confirms that active suction significantly increases the stall angle. At the same time, Figure 3.9 shows that the lift-to-drag ratio decreases as the suction coefficient increases.

Using the maximum suction coefficient, Figure 3.10 presents the resulting lift, drag, and lift-to-drag ratio for different angles of attack. Drag values are obtained through linear interpolation of the values in Figure 3.9. The maximum lift coefficient from this figure is used in further analyses. The figure also illustrates that the lift-to-drag ratio remains relatively high over a broad range of angles of attack.

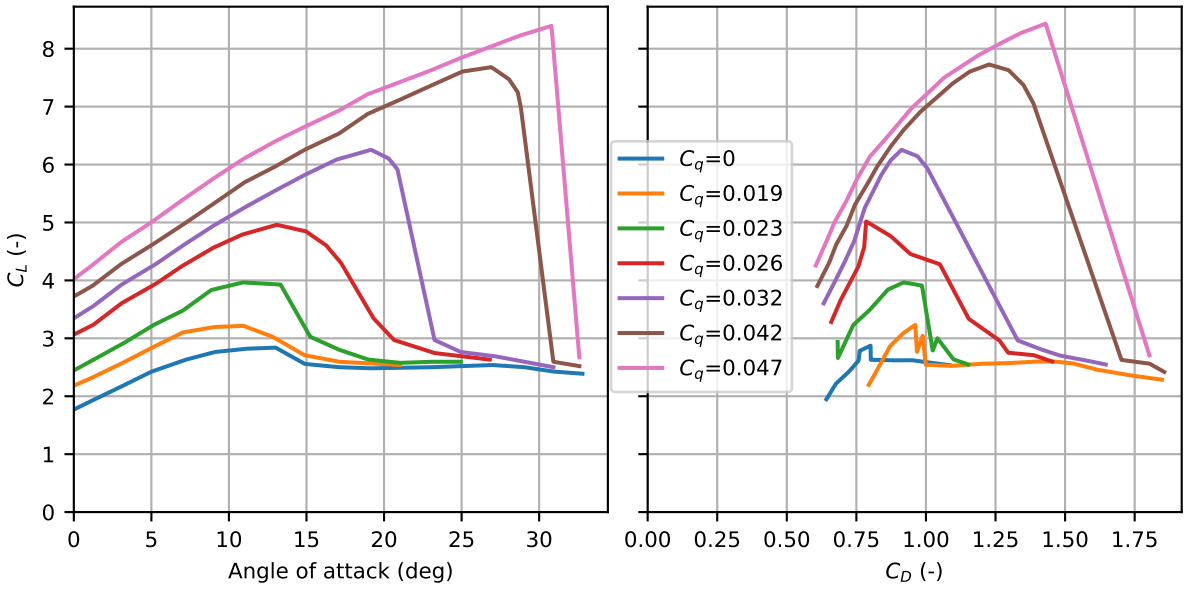

Figure 3.9: Suction wings lift and drag coefficients. Based on Charrier et al. (1985).

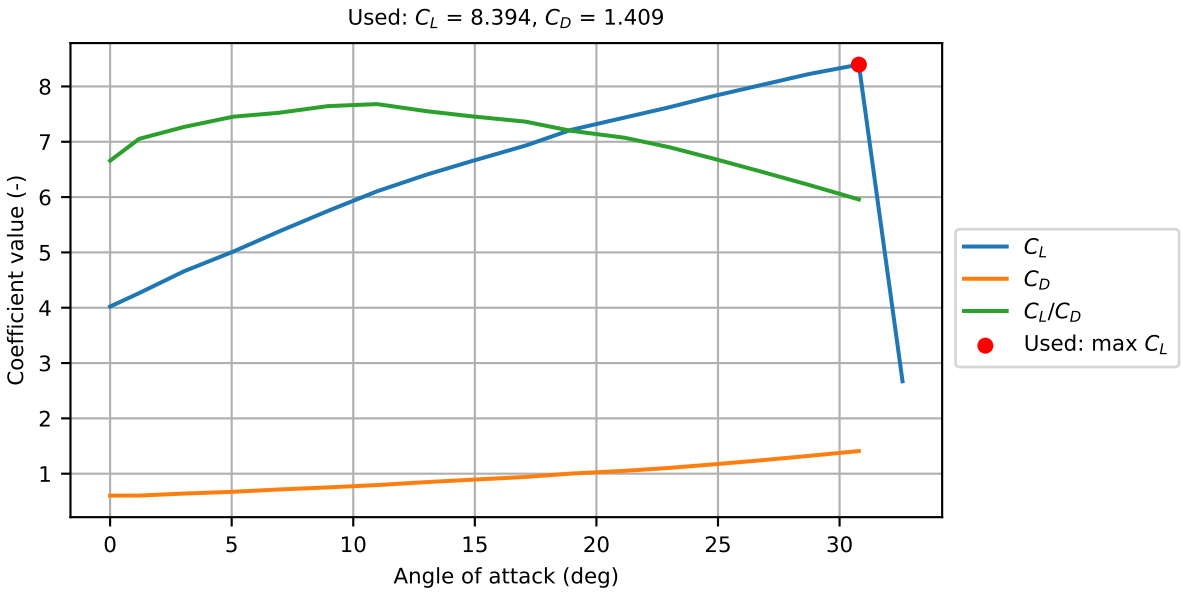

Figure 3.10: Suction wings used data for analysis. Based on Charrier et al. (1985).

Rotor sails

For the 2D rotor sail coefficients, this study adopts the data from Reid (1924). The results are shown in Figure 3.11. The coefficients are not plotted against angle of attack for the rotor sail, since the only controlling parameter is the spin ratio of the rotor. The results show a high lift coefficient with the cost of a lower lift/drag ratio compared to the other discussed WASP system types.

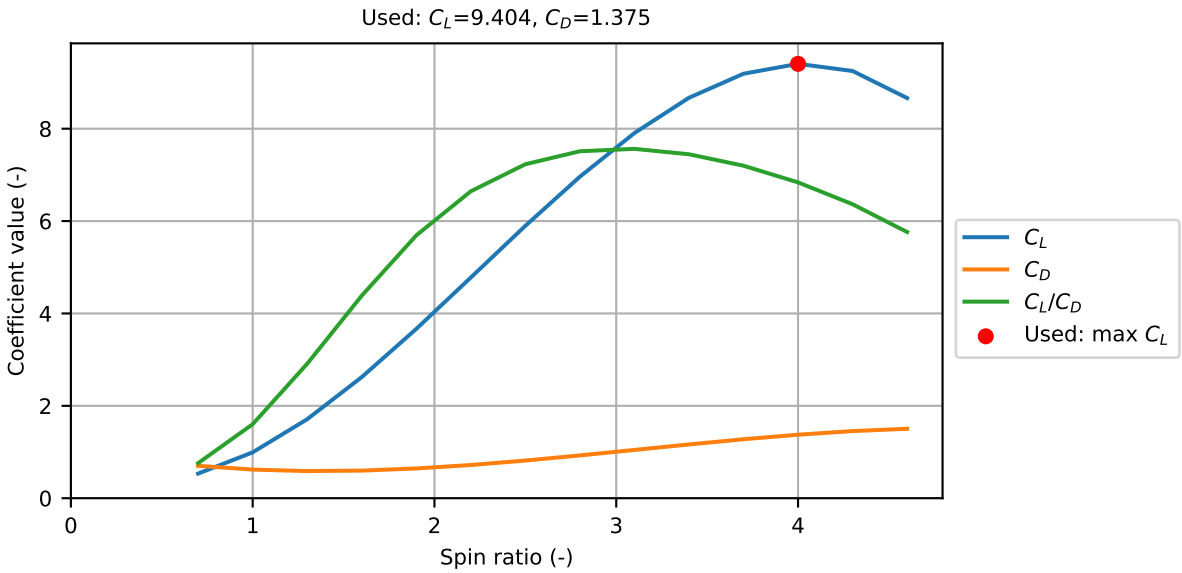

Figure 3.11: Rotor sails lift, drag, lift/drag. Based on Reid (1924).

3.2.3. Thrust coefficients

The thrust force coefficient (see subsection 2.1.1) can be used to compare the contribution of the systems. This means that the lift and drag coefficients must be assumed. The maximum found lift coefficient for the controlling parameters of the systems are used for this. Figures 3.7, 3.8, 3.10, and 3.11 indicate these by the red dot. The thrust force coefficients for the different WASP systems against apparent wind angle are shown in Figure 3.12. The figure shows that the wing sails produce a significantly lower thrust compared to the suction wing and rotor sail at optimum angles. This shows that a wing sail creates less thrust force per area, which means that these systems would have to be larger in order to create the same thrust. However, what this figure does not show, is that the lift/drag is much smaller for a wing sail, which makes it more efficient. Furthermore, a negative thrust at an apparent wind angle of 0° and a positive thrust at 180° is observed for the rotor sail and suction wing, which are caused by the assumption of a maximum possible lift coefficient, leading to relatively high drag coefficients. As seen, the maximum thrust is not generated at 90° but at a slightly higher angle. This is because the drag coefficient becomes positive for the thrust after 90°, as illustrated in Figure 2.2.

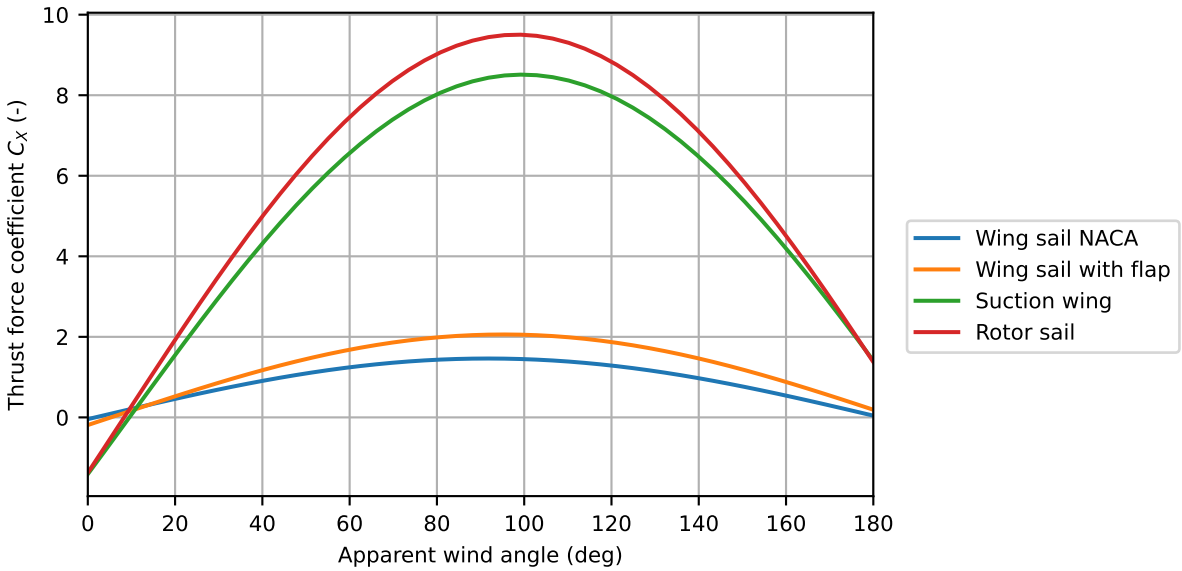

Figure 3.12: Thrust force coefficients for analysed WASP systems.

This comparison provides useful insights, but relying only on the thrust force coefficient has limitations. When assuming maximum lift, the resulting side force is also maximised. As a result, at an AWA of roughly 45°, the systems would generate side force equal to the thrust force. This is an unrealistic scenario, since in practice, the systems are controlled to maximise thrust while keeping side forces within acceptable limits. Although the rotor sail delivers the highest thrust under ideal conditions, this advantage may reduce in suboptimal conditions. Figures 3.10 and 3.11 show that the suction wing is more efficient across its controllable range. This suggests that, in terms of operability over a broader range of wind angles, the suction wing could outperform the rotor sail.

3.2.4. Regression analysis

Figure 3.13 shows the area of installed wing sails, suction wings, and rotor sails against the Gross Tonnage (GT) of the vessel (IWSA, 2025). The WASP area gives an idea of the size of the system and the GT gives an idea of the size of the vessel. This figure shows multiple insights:

- The rotor sails are the most installed WASP systems across various vessel sizes.
- The suction wings are mainly installed on smaller vessels.
- The wing sails are larger compared to rotor sails on the same vessel.

Furthermore, the information can be used as a guideline for the size of the WASP system to be installed on the Boskalis vessel. The following chapter will discuss that the Triumph is chosen for further analysis, which is shown in this figure.

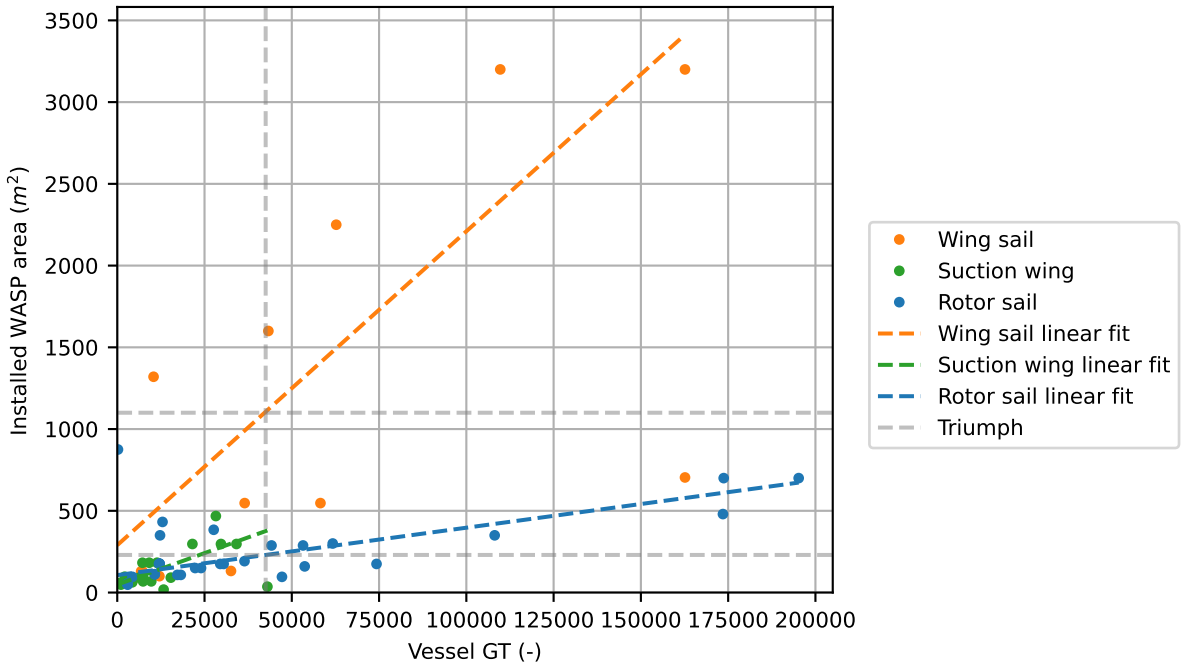

Figure 3.13: Installed frontal area of WASP systems on various vessel sizes, expressed in Gross Tonnage. Based on IWSA (2025).

3.2.5. Specific WASP system selection

Both vessel types from subsection 3.1.3 are negative affected by the installation of an additional piece of equipment. Therefore, the WASP systems are preferred to be as small as possible. The WASP analysis showed that this either has to be a suction wing or a rotor sail. The system-specific analysis shows these systems have similar performance characteristics, with both systems having each their own strengths and weaknesses. However, literature has proven the rotor sails to be more mature, and more savings have been reported (see Table 3.1). For this reason, the rotor sails are chosen for further analysis.

4

Specific vessel selection

The previous chapter gives an analysis of the existing self-propelled Boskalis fleet for the suitability of the application of WASP. The result of this analysis indicates that the HMTV and subsea rock installation fleets are suitable vessel types for WASP application. The chapter also gives an analysis of existing WASP systems, which gives as a result that the rotor sails are chosen for further calculations. The findings in this chapter support the decision of the T-class HMTV Boskalis vessels for further calculations.

First, information on PPP models from the literature review is summarised. This will form a basis for the understanding of required parameters for the development of a PPP, and forms a basis for the assessment of validity of the developed model.

4.1. Existing PPP models

The goal of the PPP to be developed is to determine the fuel consumptions and emissions during a typical voyage, and how a WASP system could influence this, as discussed in chapter 1. The general required information for the development of a PPP is discussed in subsection 2.3.1.

Furthermore, section 2.2 describes the alterations of the efficiencies of the components in the propulsion chain when applying WASP. Relating this to the propulsion chain given in Figure 2.8, the following insights have been given:

- The wake fraction changes due to a leeway angle.
- The thrust deduction factor changes due to a leeway angle and a propeller loading.
- The open water efficiency changes due to leeway angle and propeller loading.
- The relative rotative efficiency could change due to leeway angles and propeller loading.
- Engine efficiency decreases if the engine operational point is deviating from most optimal operating point.

The analysis of existing PPPs gives the following insights:

- Required ship and WASP system parameters (subsection 2.3.1)
- The number of considered DoFs depend on the goal of the calculations and the quality of input information
- Since the WASP system effectively takes over part of the total vessel resistance, this resistance must first be determined.
- The possible leeway and heel angles caused by the WASP will influence the resistance of the vessel. To calculate this, a force in multiple DoFs balance should be found between the ship and rudder hydromechanics, and the WASP system aerodynamics.

- The coefficient data on modern WASP system is limited, and the aspect ratio has an influence on the performance of the WASP system.

4.2. Specific vessel

The results in Figure 3.5 shows that the HMTV fleet scores higher according to the chosen criteria. Furthermore, Boskalis' HMTV fleet is considerably larger compared to the subsea rock installation fleet. Applying WASP on an HMTV gives the opportunity to have a larger impact on the entire Boskalis fleet. However, the discussion with Boskalis' professionals on the placement of WASP systems on this vessel type seems inconclusive. Integrating an additional piece of equipment may compromise the operational versatility. The top of the floaters are often discussed to be a straightforward option, but here, mooring winches and other types of equipment are installed. Consequently, placement of a WASP system on top of the floaters would require an innovative design.

The placement of the WASP systems on the decks of the subsea rock installation vessels is lower compared to the HMTV vessels. A short conversation with the operations manager already gave promising results about the placement of the systems. This is due to the fact that this vessel mainly will have the same mission and operational profile. This makes it more feasible to find a permanent location for the WASP systems.

4.2.1. Activity data

The activity data of the vessel types shows the potential effectivity of a WASP system. The Rockpiper is a representative vessel for the subsea rock installation fleet, and the Boka Vanguard for the HMTV fleet. The daily activities of these vessels are shown in Figure 4.1. It should be noted that only the transit time is clearly presented in this figure. The other activities are labelled as other activities due to confidentiality reasons. This figure shows that generally, an HMTV will be more often in transit mode compared to a subsea rock installation vessel. Although the lengths of the data sets differ, the figure is considered sufficiently representative for the purposes of this comparison.

The Rockpiper also operates in DP mode during rock dumping operations. The potential applicability of WASP systems during DP operations presents an interesting research topic. Understanding whether, and under what conditions, WASP could be integrated into DP control strategies may offer insights into its operational usefulness for these ship types, but this will not be further considered.

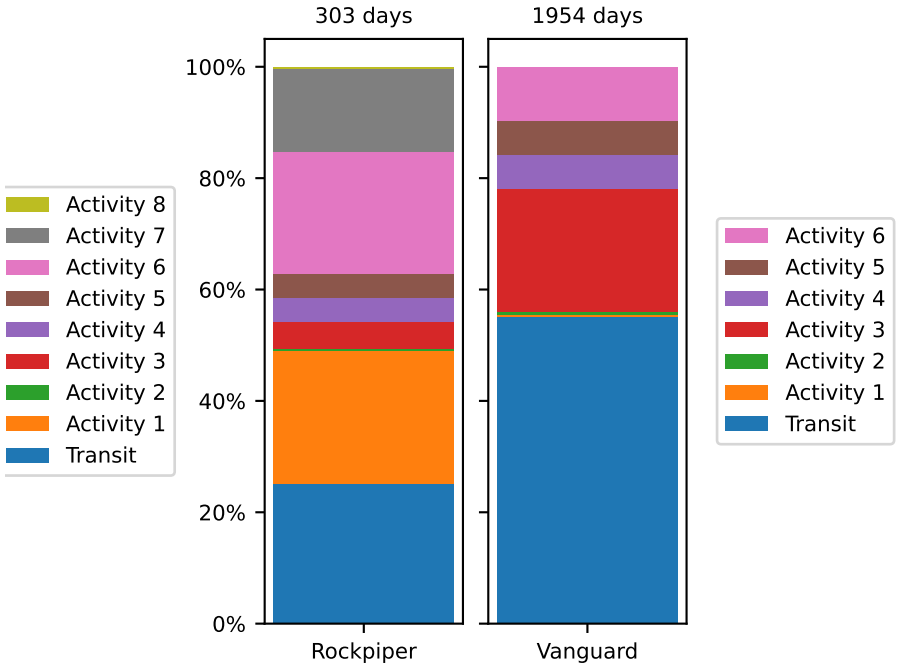

Figure 4.1: Daily activities of the Rockpiper and the Boka Vanguard (Boskalis, 2026c).

4.2.2. Potentially available information

A preliminary check on the potentially available information gives insight into modelling efforts for different vessels. On most of the Boskalis vessels, the crew members keep daily reports. These reports contain average operational data for one day. The data found in these report consist of information about the location and routing of the vessel, general engine data, and bunkering information.

Aside from the daily reports, it is currently unclear how much additional data is available or what the quality of that data will be. A short research in the internal documents gave the insight that, in general, a younger vessel will have more information and data available compared to an older vessel.

4.2.3. Specific vessel type selection

Even though the placement of the WASP systems would be more straightforward on a subsea rock installation vessel, the goal of this study is not to find the optimal placement, but to assess the potential of WASP within Boskalis. Furthermore, the results indicate that the HMTV would be more interesting according to the MCDA, the impact on the entire Boskalis fleet, and the transit time. The HMTV vessel will be picked for further analysis in this research.

Innovative concepts are being explored to overcome spatial and operational constraints associated with WASP installations (Lv et al., 2022). Recent examples, such as rotor sails fitted on a deck carrier vessel (HANSA, 2024), show that even special ship types can accommodate WASP systems when appropriate design modifications are made. Despite these developments, installing a rotor sail on an HMTV remains challenging. These vessels are required to be versatile to handle a wide range of cargo types. This leaves limited options for the installation of additional equipment. However, one vessel class stands out as having relatively few placement constraints: the T-class vessels.

4.3. T-class vessels

The T-class fleet consists of three very similar vessels: the Triumph, the Trustee, and the Target. These vessels are converted Suezmax oil tankers, originally built around the 1990s, and converted to HMTV around 2007–2008. During this period, the vessels bow and stern were cut, and a stronger middle section was fitted, because the tanker hull structure was not sufficiently strong for heavy marine transport. The conversion from the MV Marble to the Triumph is illustrated in Figure 4.2. The T-class vessels have a bow and stern which are not used for cargo transport, unlike the other HMTV, which makes the potential placement of rotor sails less complicated compared to other vessels within the HMTV fleet.

The T-class vessels have a relatively straightforward propulsion system layout: a two-stroke marine diesel engine, directly driving an Fixed Pitch Propeller (FPP). There is no shaft generator mounted.

(a) Marble in 2007. **(b)** Triumph in 2010.

Figure 4.2: Conversion of the Marble tanker to Triumph HMTV (Cargo Vessels International, 2010).

4.3.1. Triumph main data

The Triumph is one of the vessels within the T-class fleet and will be used for further reference. The main particulars are given in Table 4.1. The engine is a two-stroke MAN B&W S70MC6.

Table 4.1: Triumph main data.

Length overall	216.79 (m)
Breadth moulded	44.50 (m)
Depth moulded	14.00 (m)
Summer draft	10.44 (m)
Displacement	76023.220 (t)
Deadweight	54000 (t)
Gross Tonnage	42515 (-)
Trial speed	15.00 (kn)
Original build year	1992
Year of conversion	2008
Engine Maximum Continuous Rating (MCR)	13364 (kW) at 85 rpm

4.3.2. Triumph with WASP

The dimensioning of the potential WASP is considered in a straightforward manner. The GT of the Triumph, given in Table 4.1, is used in Figure 3.13 to determine the dimensions of rotor sails. Then, existing systems are analysed, and systems with a similar frontal area are picked. According to the regression analysis, the area for the rotor sails on the Triumph would be 229.9 m^2. With this frontal area, the Triumph is assumed to have two Norsepower rotor sails with the dimensions $28 \times 4\,\mathrm{m}$, equal to 224 m^2. A simple sketch of these rotor sails is given in Figure 4.3. This figure also shows the dimensions of potential wing sails, dimensioned using the same method, indicating the large differences in size.

The effect of the actual placement of the rotor sails is not considered in this study. The place of the sails in Figure 4.3 is purely indicative. These locations have been chosen on the basis of conversations with transport engineers, keeping in mind that these locations will interfere minimally with the versatility of the vessel. Furthermore, the assumption has been made that the equipment at the current placement of the rotor sail (such as mooring winches) could be moved to a different location. For further research, a consideration of the optimal placement could improve the rotor performance (Thies & Ringsberg, 2021).

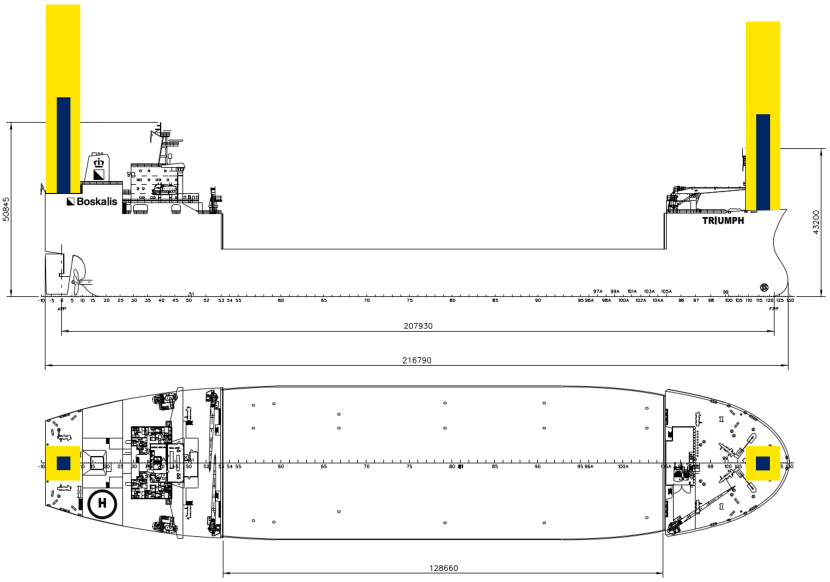

Figure 4.3: An indication of the Triumph with two rotor sails (blue, $28 \times 4\,\mathrm{m}$), and two wing sails (yellow, $55 \times 10\,\mathrm{m}$), drawn to scale (Boskalis, 2025).

However, there are some considerations taken into account regarding rotor placement:

- The largest available rotor sail ($35 \times 5\,\mathrm{m}$) does not provide the sail area required for the Triumph according to the regression analysis, meaning at least two rotors are needed.
- Using two equal-sized rotors placed roughly the same distance from the vessel's centre of gravity results in opposing side forces, which cancel out much of the generated yawing moment.
- A single large rotor is preferable to two smaller ones because one rotor can disrupt the airflow of the other, causing aerodynamic losses (van der Kolk, 2020).
- Installing fewer rotor sails is more cost-efficient (Tillig et al., 2020).

4.3.3. T-class available data

There are multiple different sources to find T-class data for the development of a PPP. Externally, some information can be found about the voyages, speed, and main particulars and technical information of the vessel. The project guide for the engine is also publicly available (MAN Energy Solutions, 2009). Internally, more information is found, such as technical drawings, stability reports, specifics of the propeller, and voyage preparation calculations. No sea trial data is available for the calculation of the resistance of the vessel. The daily report data of the Triumph dates back to January 1st 2024.

4.3.4. T-class voyages

The T-class vessels have been sailing across the North Atlantic Ocean since January 1st, 2024, transporting monopiles from different locations in Europe to different offshore locations near Canada and the United States of America. Figure 4.4 shows the Automatic Identification System (AIS) data of the T-class vessels from January 1st, 2024 to December 27th, 2025. As seen, different routes have been taken over time. This is purely due to weather routing.

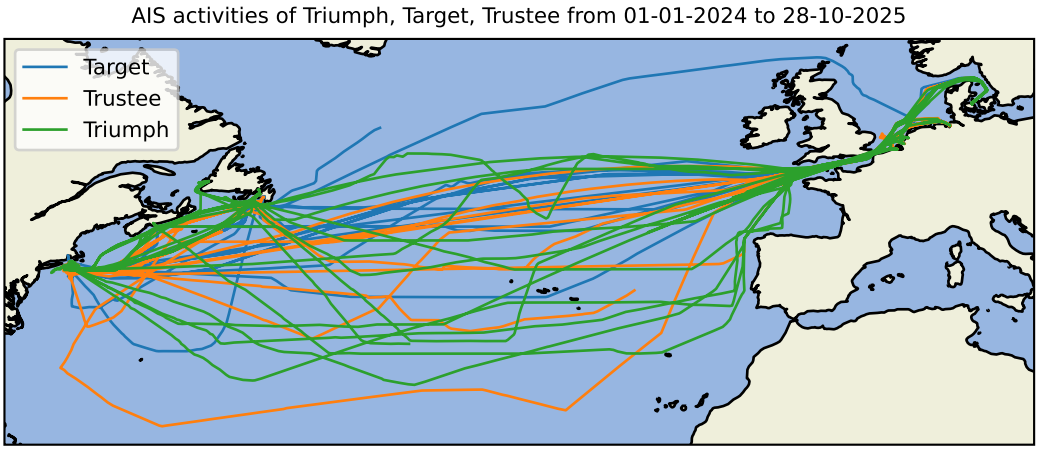

Figure 4.4: T-class routes (Boskalis, 2026c).

5

Model components development

This chapter describes the development of a steady-state 1-DoF model of the Triumph, both with and without WASP. The model is based on data extracted from the daily reports. First, the filtering and interpretation of this data are explained, followed by the development of the individual model components. The resulting steady-state model results are presented in chapter 6.

The first objective is to estimate the vessel's resistance, since no direct resistance data for the Triumph is available. This estimate is derived from the daily reports. After determining the rotor-sail forces across wind conditions, the resistance is used to compute the required propeller thrust during WASP operation. This thrust then provides the engine operating point under WASP. Figure 5.1 illustrates the model components development.

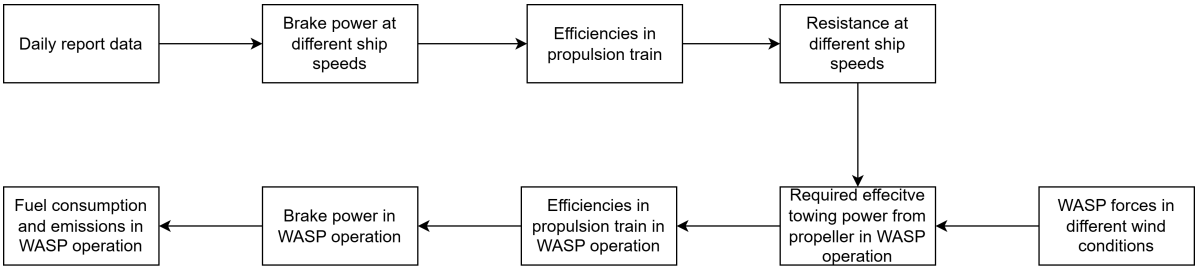

Figure 5.1: Diagram for the model components development process.

Before the model is developed, an important note is made about the convention of the coordinate system. This study adopts the system as defined by Journée and Massie (2008), which presents a North-West-Up (NWU) coordinate system. Other PPPs often adopt a North-East-Down (NED) coordinate system, likely due to the global wind North-East-South-West convention.

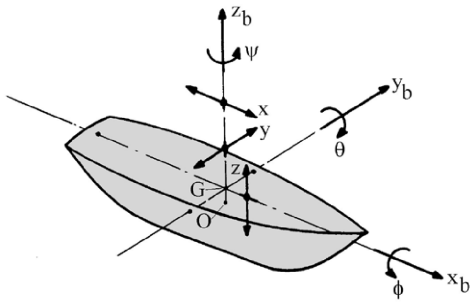

Figure 5.2: Definition of ship motions in six degrees of freedom (Journée & Massie, 2008).

5.1. Daily reports

As discussed in subsection 4.2.2, the crew takes daily reports of general information about the vessel, averaged for one day. The data logged in these reports are the following:

- Date, latitude, longitude, time zone.
- Average ship speed, course, departure information, estimated time of arrival, last port of call, remaining miles, sailed distance.
- Bunkering information, used fresh water, used Low Sulphur Marine Gas Oil (LSMGO), used lubrication oil.
- Average main engine load (% of MCR), main engine running hours, main engine speed (rpm).

Even though the data in these reports is quite useful, it has to be filtered. Mistakes can be made easily while logging this information. Furthermore, many datasets are incomplete. The main engine running hours have been selected as a preliminary data filter. Only data with the main engine running for 24 hours are deemed to be useful. Figure 5.3 shows the data filtering process for the total dataset. This figure illustrates the amount of empty datasets. Some data points show an unrealistic number of running hours per day, indicating possible logging mistakes.

Figure 5.3 shows the same data filtering process, but on the right-hand figure, the y-axis is capped at 26 hours. This figure shows the data sets being filtered above and below 24 running hours. In total, 103 days out of 667 days can be used after this data filter.

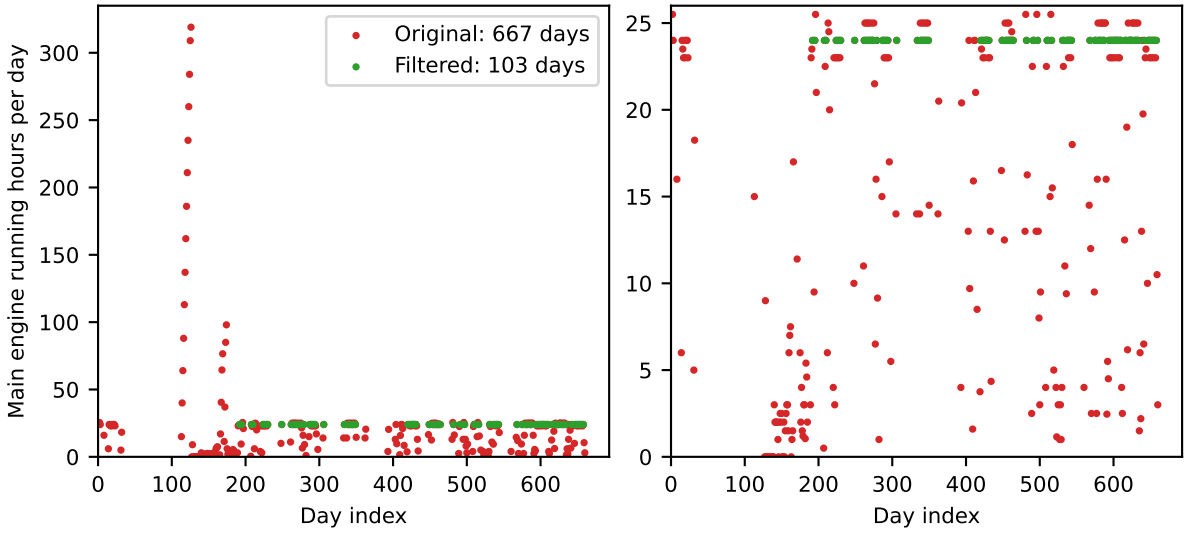

Figure 5.3: Main engine running hours data filter.

5.2. Delivered power coefficient

For ships with Froude numbers between 0.1 and 0.2, the resistance is proportional to the ship speed squared (Equation 5.1) (Klein Woud & Stapersma, 2002). The power required to tow such a vessel at a certain ship speed (the effective towing power) is proportional to the cube of the ship speed (Equation 5.2).

$$R = c_1 \cdot v_s^2 \tag{5.1}$$

$$P_E = R \cdot v_s = c_1 \cdot v_s^3 \tag{5.2}$$

The Froude number of the Triumph is calculated using Equation 5.3. The trial speed ($v_{s,trial}$) as stated in Table 4.1 and an assumed waterline length (L_{wl}) based on technical drawings are used to calculate this number. The estimated value is given in Table 5.2. As seen, the resistance of the Triumph follows the cube law.

$$Fr = \frac{v_{s,trial}}{\sqrt{g \cdot L_{wl}}} = 0.173 \tag{5.3}$$

Because no direct resistance or effective towing power data is available for this vessel, an alternative method is needed to estimate resistance at different ship speeds. The daily reports provide average brake power corresponding to average ship speeds, and this information can be used to establish a relationship between brake power and ship speed using the delivered power coefficient (C_D). This approach relies on several assumptions:

- A constant hull efficiency.
- A constant propeller efficiency.
- A constant relative rotative efficiency.

With all these assumptions in place, the delivered power (power available at the propeller, see Figure 2.8) can be expressed as being proportional to the cube of the ship speed, just as the effective power:

$$P_D = \frac{P_E}{\eta_D} = \frac{c_1 \cdot v_s^3}{\eta_D} = c_2 \cdot v_s^3 = C_D \cdot \rho^{1/3} \cdot \Delta^{2/3} \cdot v_s^3 \tag{5.4}$$

Equation 5.4 shows that the relationship is also influenced by the displacement (Δ). The delivered power may also vary due to hull fouling, weather conditions, or water depth. Especially in HMTV, the type of cargo may also have an influence, due to increased air resistance for cargo with large frontal areas.

Since the Triumph does not have a gearbox, the only conversion from delivered power to brake power is the shaft efficiency (see Figure 2.8). The shaft efficiency is assumed to remain constant at a value of 0.99 for the Triumph (Klein Woud & Stapersma, 2002). This assumption leads to the following relationship between the brake power and the vessel speed:

$$P_B = \eta_S \cdot P_D = \eta_S \cdot c_2 \cdot v_s^3 = \eta_S \cdot C_D \cdot \rho^{1/3} \cdot \Delta^{2/3} \cdot v_s^3 \tag{5.5}$$

$$C_D = \frac{P_B}{\eta_S \cdot \rho^{1/3} \cdot \Delta^{1/3} \cdot v_s^3} \tag{5.6}$$

Where the displacement is calculated based on the summer draft and seawater density is assumed. Equation 5.5 can be rewritten for C_D, shown in Equation 5.6. Now, different values for P_B and v_s could be used to calculate a representative C_D:

- Using the MCR and trial speed.
- Using the most common engine load and corresponding ship speed from the daily reports.
- Calculating C_D for every daily report index, and taking a mean value.
- Calculating C_D for every daily report index, and use a least-squares fitting.

It is important to quantify which values represent the actual case with the highest accuracy. A higher accuracy for the delivered power coefficient ultimately leads to a higher accuracy for the estimated resistance. This can be illustrated by calculating C_D for every data point, and plotting the C_D using the methods described above in the same plot, while calculating the error (R^2). This is shown in Figure 5.4.

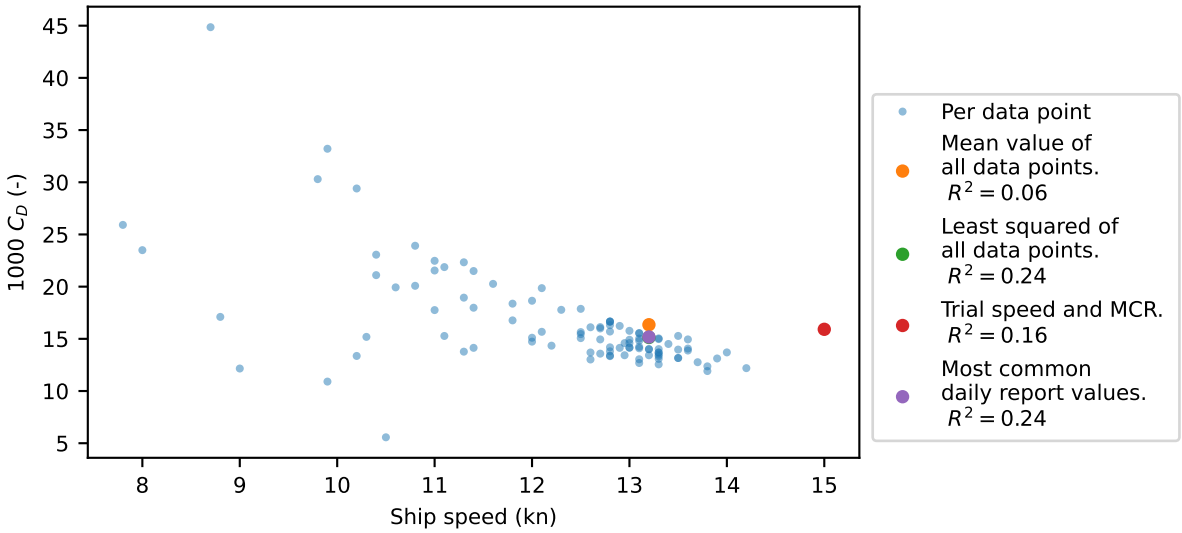

Figure 5.4: C_D values using different calculation methods.

The low R^2 values in Figure 5.4 indicate that the chosen C_D values might not represent the relationship from Equation 5.5 sufficiently to use in further calculations. The figure also shows that some C_D points are diverging from the more common data points. These deviant points might be due to rough weather conditions, other external factors, or simply due to logging errors. Therefore, the data will be filtered even further to acquire a representative C_D value.

For the second filtering step, an acceptable error margin is first defined. Subsequently, multiple candidate values for C_D are tested to determine which value results in the largest number of data points falling within this margin. This is carried out as an iterative procedure, where each trial value of C_D is evaluated based on how many observations it classified as valid. The outcome of this process is shown in Figure 5.5.

A C_D value is identified that retains a sufficiently large subset of the measured data while remaining within the prescribed error bounds. It should be noted that this error margin is computed using only the data points that passed the second filter. The figure demonstrates that the selected C_D produces a reasonable approximation of the vessel's brake power around its most frequently observed operating speed from the daily reports.

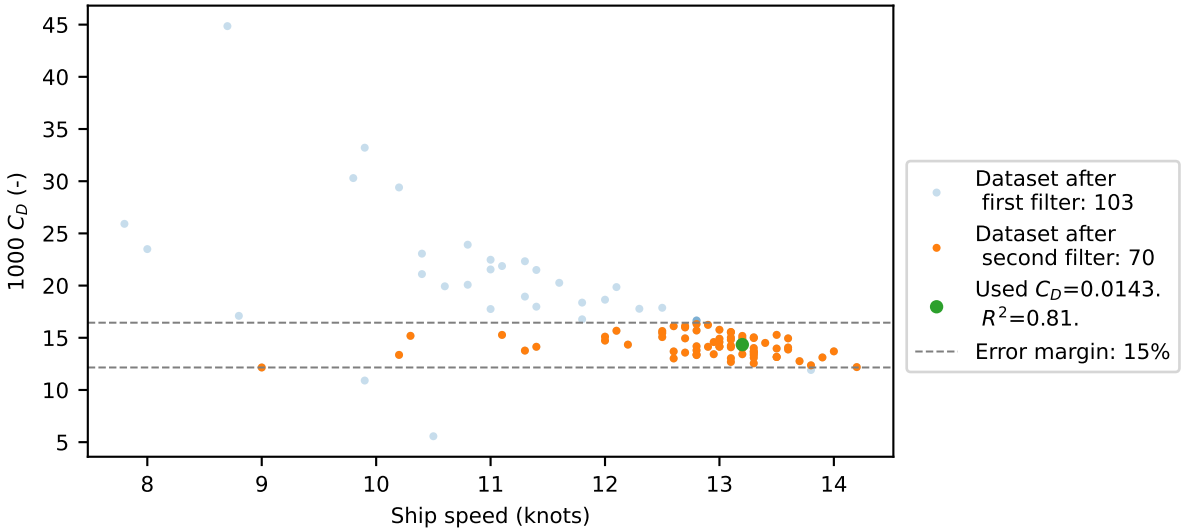

Figure 5.5: C_D value filter.

The delivered power coefficient is used to describe a relationship between the engine brake power and the ship speed. This is shown in Figure 5.6. This forms a basis for the calculations of the ship resistance. For this, the relative rotative efficiency, propeller efficiency, and hull efficiency have to be estimated. A diagram for this process is shown in Figure 5.7.

The daily report data analysis also gave insight into the actual operations of the ship. The most important insights are listed below. The mean ship speed will be used for further calculations.

- The most common engine load is at 65% of the MCR
- The mean ship speed at this engine load is 13.2 knots
- The mean engine rotational speed at this engine load is 71.9 rpm
- The ship sails on Marine Gas Oil (MGO)

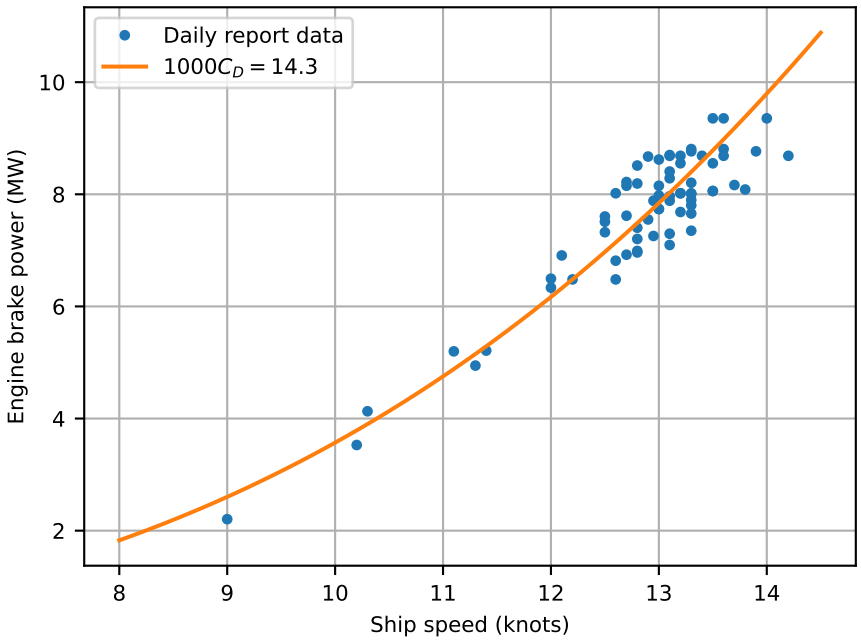

Figure 5.6: Engine brake power against ship speed.

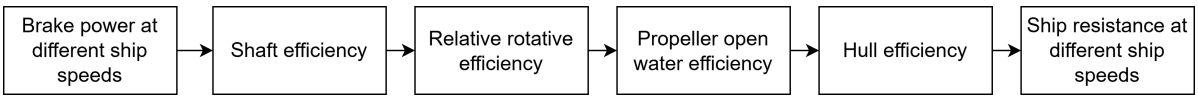

Figure 5.7: Diagram showing steps from engine brake power to ship resistance.

The relation between the brake power of the engine and the ship speed has been established. A constant shaft efficiency is assumed, which means the next step is to determine the relative rotative efficiency. This parameter is however calculated using an empirical method, which includes the calculation of the hull efficiency. Therefore, first, the propeller open water efficiency will be discussed.

5.3. Propeller open water diagram

An internal document is available for the design parameters of the Triumph propeller. This document is from 1987, and the propeller type has not been changed since then. The parameters for this 'Meridian Propeller', designed by Stone Manganese Marine Limited, are given in Table 5.1. This table includes information about the originally designed thrust and torque values of the propeller.

Table 5.1: Meridian propeller design parameters.

Parameter	Value
Diameter (D_p)	$8050\,\mathrm{mm}$
Mean pitch (P_p)	$5510\,\mathrm{mm}$
Expanded surface area (A_e)	$29.640\,(\mathrm{m}^2)$
Number of blades	$4\,(-)$
Calculated moment of inertia	$105570\,(\mathrm{kg\,m}^2)$
Estimated moment of inertia of entrained water	$26530\,(\mathrm{kg\,m}^2)$
Ship speed	$14.85\,\mathrm{kn}$
Max. shaft power	$14197\,\mathrm{kW}$
Propeller rotational speed	$89.90\,\mathrm{rpm}$
Gear ratio	1:1
Mean propeller thrust	$1557482\,\mathrm{N}$
Mean propeller torque	$1479546\,\mathrm{Nm}$

The open-water diagram is given in this document, so an approximation must be made to determine the propeller efficiency. This is done by assuming a Wageningen B-series propeller. Using the parameters listed in Table 5.1, the required propeller characteristics can be calculated:

$$A_e/A_0 = \frac{29.640}{\pi \cdot 4.025^2} \approx 0.6 \tag{5.7}$$

$$P_p/D_p = \frac{5510}{8050} \approx 0.7 \tag{5.8}$$

The Meridian propeller is approached using the Wageningen B4–60 with $P/D = 0.7$. The open water diagram can be created by using an interpolation function of the model test results of the Wageningen B-series propeller (van Lammeren et al., 1969). The method for this is described in Carlton (2018). The open water diagram of the approached propeller is shown in Figure 5.8.

The ship characteristics can be implemented into the open water diagram, which is used to calculate the advance coefficient, thrust, torque, and propeller efficiency (Klein Woud & Stapersma, 2002). The procedure follows from engine brake power to propulsion power (see Figure 2.8). The following equation to calculate the torque coefficient (K_Q) of the vessel, to be matched with the propeller, is used (Prof. Dr. Ir. Kuiper, 2003):

$$K_{Q,ship} = \frac{P_O}{2\pi \cdot \rho \cdot D_p^2 \cdot v_A^3} J^3 = \frac{P_B \cdot \eta_S \cdot \eta_R}{2\pi \cdot \rho \cdot D_p^2 \cdot (v_s \cdot (1-w))^3} J^3 \tag{5.9}$$

In which the brake power is calculated using Equation 5.5. The determination of the wake fraction (w) and relative rotative efficiency (η_R) will be described in section 5.4. The intersection of $K_{Q,ship}$ and $K_{Q,prop}$ gives the K_T, K_Q, η_O, and the J. The result is shown in Figure 5.8. The advance coefficient is used to calculate the propeller rpm (Equation 5.10). The thrust and torque coefficients are used to calculate the thrust and torque of the propeller (Equations 5.11 and 5.12, respectfully).

$$J = \frac{v_A}{D_p \cdot n_p} \quad \rightarrow \quad n_p = \frac{v_A}{J \cdot D_p} \tag{5.10}$$

$$T = K_T \cdot \rho \cdot n_p^2 \cdot D_p^4 \tag{5.11}$$

$$Q = K_Q \cdot \rho \cdot n_p^2 \cdot D_p^5 \tag{5.12}$$

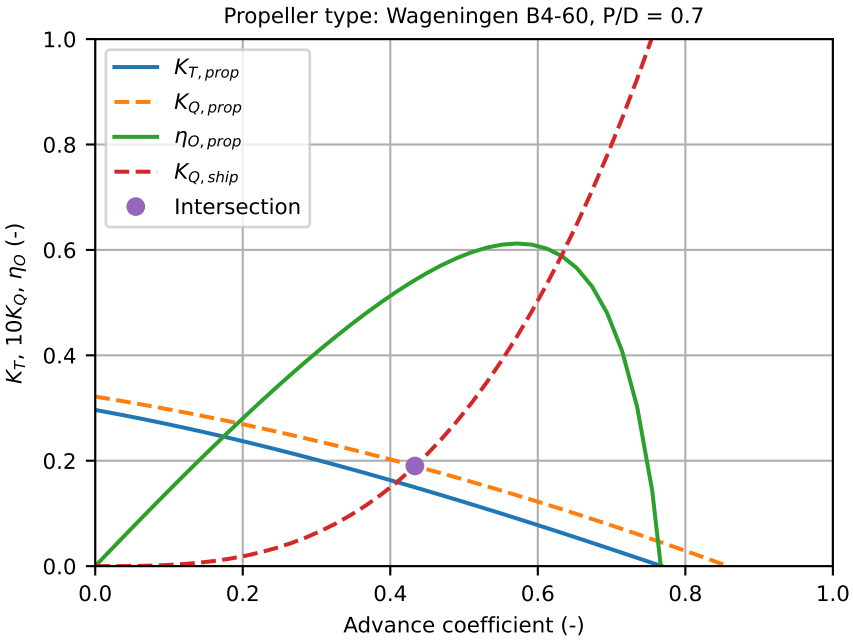

Figure 5.8: Open water diagram of the Meridian propeller, matching of vessel and propeller.

5.4. Remaining parameters

The remaining parameters for the approximation of the resistance of the vessel are the relative rotative efficiency (η_R), the wake factor (w), and the thrust factor (t). Because these parameter values are not available in the Boskalis database, an alternative method must be used to approximate them.

The wake, thrust, and relative rotative efficiency all can be calculated using Holtrop and Mennen (1982). This empirical method is well-known for its reliable results in the design phase of a vessel for these types of vessels (Bertram, 2012). However, several parameters must first be defined before the calculations can be performed.

The waterplane area of the Triumph can be calculated by using the stability booklet. This booklet contains information about the displacement of the vessel (Δ) for different draft values. The waterplane area (A_{WP}) is then calculated by dividing the displacement by the draft for a small strip:

$$A_{WP} = \frac{\Delta_2 - \Delta_1}{\rho * (T_2 - T_1)} \tag{5.13}$$

The Longitudinal Centre of Buoyancy (LCB) is also given for different draft values. The LCB for the summer draft can be found by linearly interpolating between the two closest draft values. The bulb, tunnel thruster, rudder, and midship dimensions are estimated using internal technical drawings. The wetted surface area is calculated using the empirical formula given in Holtrop and Mennen (1982). The input parameters are given in Table 5.2. The results for the thrust deduction factor, wake fraction, and relative rotative efficiency are also given in this table.

Table 5.2: Input parameters and propulsion factors from Holtrop and Mennen (1982).

Parameter	Value
L_{wl}	$203.7\,(\mathrm{m})$
$T = T_A = T_F$	$10.44\,(\mathrm{m})$
A_{WP}	$7773.0\,(\mathrm{m}^2)$
LCB	$-2.66\,\%$ aft of $1/2\,(L_{pp})$
A_{BT}	$50.15\,(\mathrm{m}^2)$
h_B	$5.12\,(\mathrm{m})$
C_{BTO}	0.005 (-)
d_{BTO}	$2.2\,(\mathrm{m})$
A_T	$0\,(\mathrm{m}^2)$
S	$11003.6\,(\mathrm{m}^2)$
S_{APP}	$163.6\,(\mathrm{m}^2)$
C_{stern}	0 (-)
$(1 + k_2)$	1.75 (-)
C_B	0.784 (-)
C_M	0.991 (-)
$C_P = C_B/C_M$	0.791 (-)
$C_{WP} = A_{WP}/(L_{wl} \cdot B)$	0.858 (-)
w	0.602 (-)
t	0.216 (-)
η_R	1.02 (-)

The results in Table 5.2 show a reasonable thrust deduction factor and relative rotative efficiency. However, the wake fraction seems overestimated. Bertram (2012) describes that empirical formulas, like Holtrop and Mennen (1982), tend to overestimate the wake fraction for full vessels. Given that this fraction normally is in the range between 0.2–0.45 (Wartsila, 2026), this estimated wake fraction is assumed to be too high for further calculations.

The wake fraction can also be estimated using the design information of the Meridian propeller provided in Table 5.1. This table specifies the ship speed, engine power, and corresponding engine rpm for the design point of the propeller. Using these values, the propeller open-water characteristics can be revisited following the same methodology described in section 5.3. In this case, however, the engine rpm ($60 \cdot n_p$) is already known. Therefore, the propeller-matching procedure is performed iteratively: successive values of the wake fraction are applied, and for each trial value the resulting propeller advance coefficient is used to compute the corresponding rpm via Equation 5.10. The wake fraction is adjusted until the calculated rpm matches to the design rpm provided in the table. Through this iterative procedure, a representative wake fraction of $w = 0.352$ is obtained. The results of this calculation are summarised in Table 5.3.

Table 5.3: Meridian propeller design and calculated parameters.

Parameter	Meridian	Calculated	Difference
Rotational speed (rpm)	89.90	89.91	0.0 %
Propeller thrust (N)	1557482	1531049	-1.7 %
Propeller torque (Nm)	1479546	1541139	4.0 %

The Meridian propeller thrust and torque in Table 5.3 show some deviations from the calculated values. The results show that there is less torque required to propel the vessel, and more thrust. This may be due to various reasons:

- The Meridian propeller is approached using a Wageningen B-series linear interpolation
- The ship was converted from a tanker to a HMTV, which influenced the hull form
- Hull fouling is influencing the speed profile of the entrained water at the propeller

However, given that no more information is available, the wake fraction value of $w = 0.352$ is used for further calculations. Finally, now that the wake fraction and thrust deduction factor are estimated, the hull efficiency can be calculated using Equation 2.11.

5.5. Resistance estimation

The resistance can be calculated using empirical methods, for instance Holtrop and Mennen (1982), using the parameters from Table 5.2. The resistance according to Holtrop and Mennen (1982) is shown in Figure 5.9. The bulb resistance in this figure is relatively high due to the overestimation of the dimensions of the bulb. Furthermore, the wave-making resistance is relatively low, due to the low Froude number of the vessel.

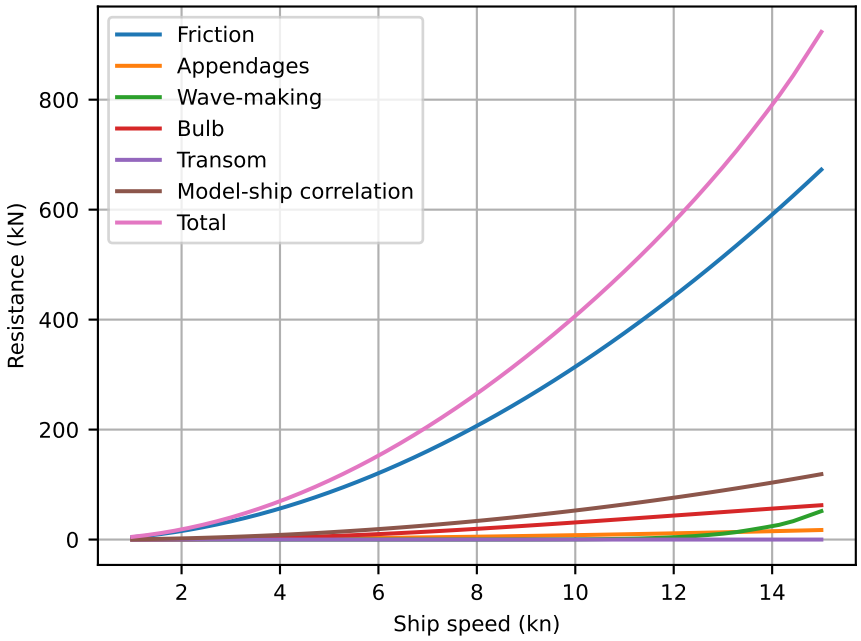

Figure 5.9: Resistance components according to Holtrop and Mennen (1982).

The empirical resistance in Holtrop and Mennen (1982) calculates the still water resistance of the vessel. In real conditions, the ship also encounters influences from the environment, that is wind, waves, and currents. The real resistance is therefore expected to be higher.

The resistance of the vessel can be estimated using Equation 5.1, requiring the constant c_1, calculated using Equation 5.14. The calculated resistance, together with the total resistance from Holtrop and Mennen (1982), is shown in Figure 5.10. This figure shows indeed that the approximated resistance is higher compared to the empirical method. For further calculations, the approximated resistance (blue line in Figure 5.10) will be used.

$$c_1 = \frac{R}{v_s^2} = \frac{P_E}{v_s^3} = \frac{P_D \cdot \eta_R \cdot \eta_O \cdot \eta_H}{v_s^3} = C_D \cdot \rho^{1/3} \cdot \Delta^{2/3} \cdot \eta_R \cdot \eta_O \cdot \eta_H = 17390.2 \tag{5.14}$$

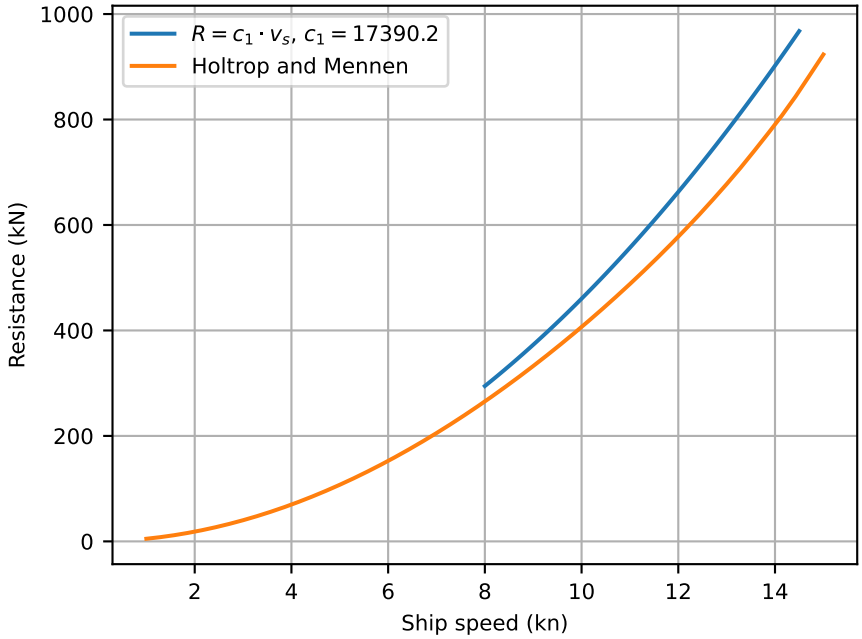

Figure 5.10: Estimated resistance of the Triumph using Holtrop and Mennen (1982) and operational ship data.

5.6. Engine data

The project guide shows the performance curves of the engine as well as the engine layout and load diagrams of the MAN B&W S70MC6 (MAN Energy Solutions, 2009). The Triumph was originally delivered in 1989 and the project guide is from 2009. Therefore, performance differences are expected.

With the assumptions established in this chapter, an additional useful relationship can be derived between the propeller torque and the rotational speed, known as the propeller law (Klein Woud & Stapersma, 2002). This law shows that the propeller torque is proportional to the square of the shaft speed Equation 5.15.

$$M_p \propto n_p^2 \tag{5.15}$$

In this case, since the vessel does not have a gearbox (therefore the engine speed and propeller speed are equal, Equation 5.16) and a constant shaft efficiency is assumed, another relationship can be derived between the engine speed and the engine brake power:

$$n_p = n_e \tag{5.16}$$

$$M_B = \frac{M_P}{\eta_S} \propto n_e^2 \tag{5.17}$$

$$P_B = M_B \cdot n_e \cdot 2\pi = c \cdot n_e^3 \tag{5.18}$$

The constant c can be determined by using the MCR of the engine. This relationship is also described in the project guide of the engine (MAN Energy Solutions, 2009). The engine load diagram, together with the propeller law, is shown in Figure 5.11. The project guide data shows similar behaviour as the propeller law with a small performance difference. This may be due to the time difference between the published date of the engine and the original building date of the Triumph, or due to the digitising of the data from the project guide.

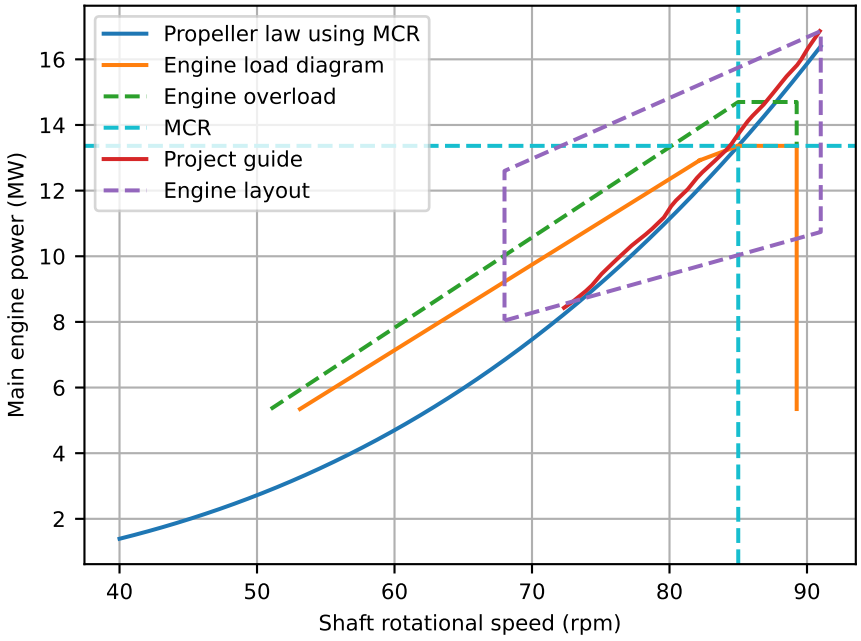

Figure 5.11: MAN B&W S70MC6 engine load diagram. Based on MAN Energy Solutions (2009).

5.7. Specific fuel oil consumption and emission factors

The SFOC of the engine depends on multiple different factors such as weather conditions, stability conditions, fouling, and much more, just as the resistance. The SFOC can be calculated per data point from the daily reports, resulting in a very scattered plot (see Figure 5.12). The data points are only reliable around 13.2 knots, since the other data more or less has been filtered.

Above 50% MCR, a constant SFOC is typical for low speed diesel engines (Klein Woud & Stapersma, 2002). This is also the case for the MAN B&W S70MC6 engine (MAN Energy Solutions, 2009). Therefore, to simplify further calculations, the SFOC is taken as constant. The definition of the specific fuel oil consumption is shown in Equation 5.19 (Klein Woud & Stapersma, 2002).

$$sfc\left(\frac{\mathrm{g}}{\mathrm{kWh}}\right) = \frac{1}{\eta_e \cdot h^L(\mathrm{kJ/kg})} \cdot 1000\left(\frac{\mathrm{g}}{\mathrm{kg}}\right) \cdot 3600\left(\frac{\mathrm{s}}{\mathrm{h}}\right) \tag{5.19}$$

In this equation, h^L is the lower heating value of the fuel, which is a constant. The equation shows that by assuming a constant SFOC, this also means the assumption of a constant engine efficiency η_e. A valid value for the SFOC is however difficult to determine as shown in Figure 5.12. The figure shows constant SFOC values, calculated using different methods:

- A mean value of every daily report data point.
- A median value of ever daily report data point.
- A mean value for the daily report data points only at the calculated mean ship speed of 13.2 knots.
- A mean value from the Project Guide (MAN Energy Solutions, 2009).
- A mean value from the Ship Energy Efficiency Management Plan of the Triumph.

The error (R^2 value) associated with these SFOC values is also shown in Figure 5.12. These results indicate that the accuracy of the fuel consumption estimation would only decrease if the mean value from the daily report data were not used. Furthermore, it is likely that the fuel consumption of the generators is included in the daily report values. This may explain the difference between the MAN specified and the median calculated SFOC value. To minimise the influence of outliers, the median SFOC is used in further calculations.

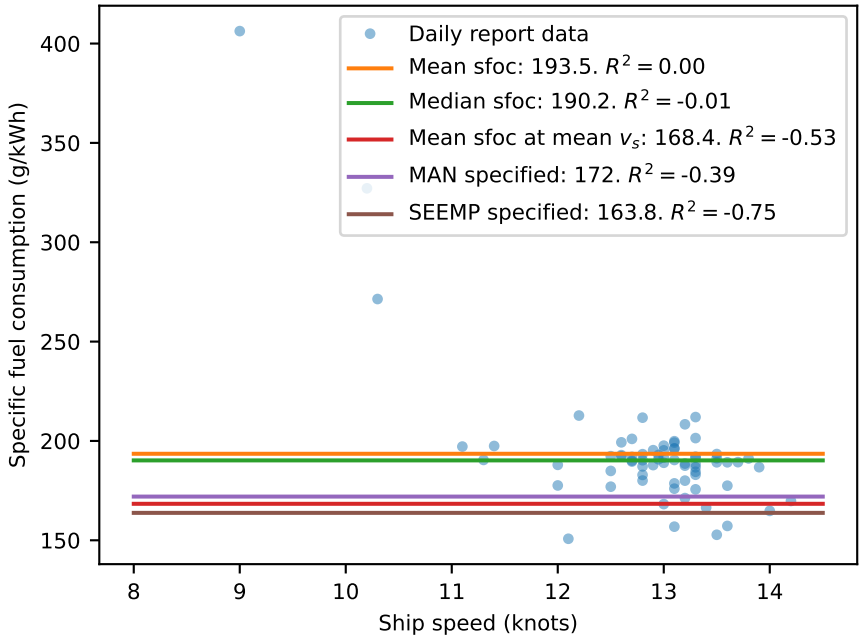

Figure 5.12: Specific fuel oil consumption value comparison.

The emissions are calculated using emission factors as described by the IMO (IMO, 2020). These emission factors relate the emissions to consumed fuel and consumed energy during a voyage. The values for the emission factors are given in Table 5.4 for both the fuel-based and energy-based emission factors. The values for the black carbon emission factors, which depend on the engine load, are given in Table 5.5. The emission factors are taken for MGO, a slow-speed two-stroke marine diesel engine of Tier I, generation I, and the most recent fuel data, which is from 2018.

Table 5.4: Fuel-based and energy-based emission factors for MDO. Based on (IMO, 2020).

Emission type	Factor	Unit
CO_2	3.206	(g/g)
SO_x	0.0014	(g/g)
NO_x	17.0	(g/kWh)
PM_{10}	0.18	(g/kWh)
CH_4	0.010	(g/kWh)
CO	0.044	(g/kWh)
N_2O	0.030	(g/kWh)
NMVOC	0.632	(g/kWh)

Table 5.5: Black carbon emission factors for MDO. Based on (IMO, 2020).

Engine load [%]	<5	10	20	30	40	50	60	70	80	90	100
BC factor ($\times 10^{-5}$) (g/g)	10.0	8.0	6.0	5.0	4.0	4.0	4.0	4.0	3.0	3.0	3.0

Using constant emission factor values can provide a reasonable approximation for CO_2 and SO_x. However, for other emission types, these constants give only indicative results. The calculated emission values will not accurately describe real conditions because of the complex relationship between engine operating behaviour and the resulting emission profile, as discussed in subsection 2.4.1.

5.8. Rotor coefficients

The lift and drag coefficients used in Figure 3.2.2 assume infinite aspect ratio (2D coefficients). This means that the influence of the flow at the end of the rotor is not considered. However, this can lead to an overestimation of the rotor performance, as this section will show.

The 3D coefficients (including aspect ratio and end plate influences) are calculated using the data from Reche-Vilanova et al. (2021) (originally Reid (1924)), by digitising the data given in this study. This gives access to data for 3D lift and drag coefficients for rotor sails with a varying AR from 1.68 to 12.0, and for varying end plate diameters (De/D, ratio of end plate diameter (De) to rotor sail diameter (D), from 1.0 to 3.0). This is shown in Figure 5.13. It should be noted that this data is from model tests, not from real-world application, which may influence the lift and drag coefficients.

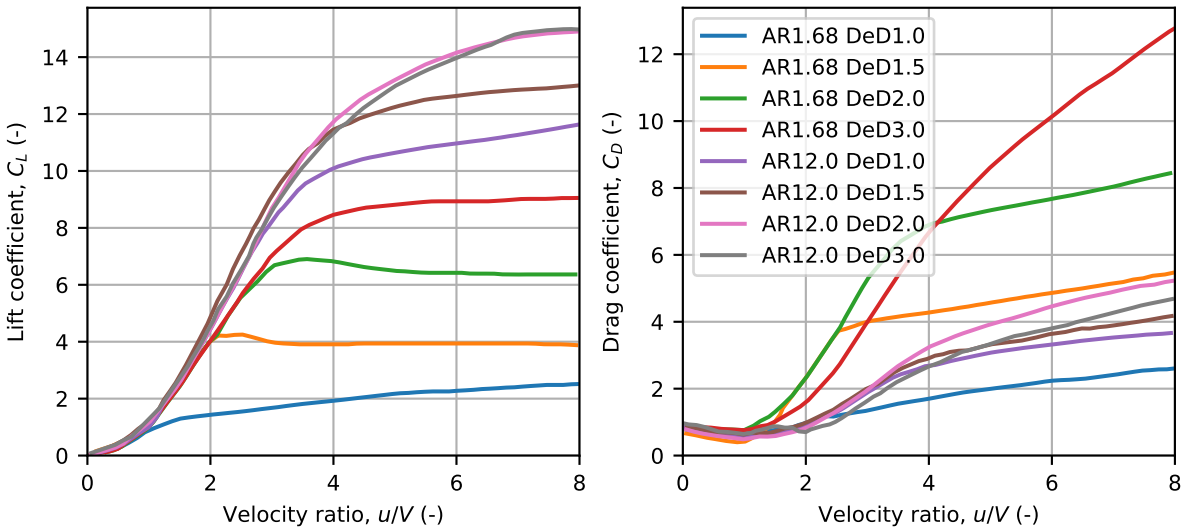

Figure 5.13: 3D lift and drag coefficient for different rotor sail designs. Based on Reche-Vilanova et al. (2021).

The determination of the size of the rotor sails has been discussed in subsection 4.3.2. The Norsepower rotor sail $28 \times 4\,\mathrm{m}$ has an aspect ratio of 7 and an end plate diameter against rotor sail diameter of 1.67 (Norsepower, n.d.). These parameters can be interpolated for using the data in Figure 5.13. This requires a 2-dimensional interpolation function. The python regular grid interpolation function is used for this (SciPy, 2026b).

The values for the lift and drag coefficients are shown in Figure 5.14. This figure also shows the difference between the calculated coefficients in Figure 3.2.2. The large differences between the values (especially the drag coefficient) shows the importance of considering the aspect ratio and end plate configurations of the rotor sail.

The rotor sails are assumed to remain a constant spin ration for further calculations, to simplify the calculations. The spin ratio is assumed to remain at a value of 4, because the gain in extra propulsion above this value is very small compared to the extra power that is required to spin the rotor sail (Eggers, 2016).

This assumption is however not necessarily valid for all operating conditions. van der Kolk (2020) discussed that the spin ratio may vary for apparent wind angle, to find a balance in thrust force and side force, and that the spin ratio for upwind sailing conditions should be lower compared to downwind sailing conditions. Assuming a constant spin ratio of 4 may lead to an overprediction of generated thrust in different apparent wind conditions.

This study treats the apparent wind as uniform and non-disturbed. In reality, the apparent wind will be disturbed by the hull and accommodation, depending on the apparent wind conditions. It also depends on the altitude, as discussed in Smeets (2024). To include these effects, the particular locations of the

systems on the deck should be known. Furthermore, this study does not consider the required power to spin the rotor, or the added air resistance when the rotor is not spinning.

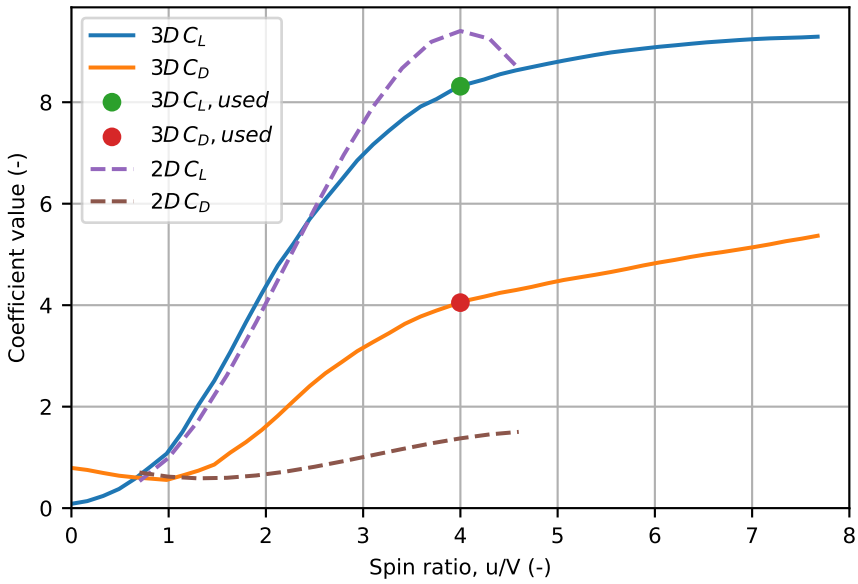

Figure 5.14: Lift and drag coefficients of a $28 \times 4\,\mathrm{m}$ rotor sail.

In section 3.2, the performance of the WASP systems is compared using a thrust force coefficient. The same can be applied to assess the performance of the rotor in 2D and 3D. The deviant lift and drag coefficients shown in Figure 5.14 leads to an altered thrust force coefficient. Figure 5.15 shows that the 3D coefficients have a large impact on the thrust force coefficient. The figure shows that the rotor only delivers a positive thrust force after round 25 degrees of apparent wind angle. Furthermore, the peak of the thrust force shifts more towards a higher degree, due to the higher drag coefficient.

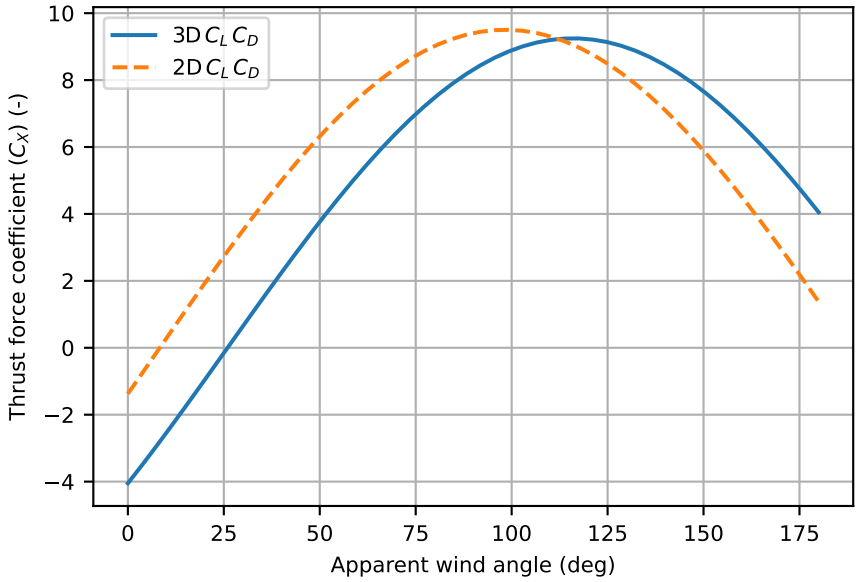

Figure 5.15: Rotor thrust force coefficient of 2D and 3D lift and drag coefficients.

5.9. WASP operation

The required components for calculating the propeller thrust in WASP operations have been determined. The engine operational points during WASP operations can be estimated assuming arbitrary wind conditions, following the method illustrated in Figure 5.1. This section provides an example calculation for the engine operational point in WASP operations, to be later used in the models.

The forces from the installed rotor systems are calculated using Equation 5.20. In this equation, $F_{x,WASP}$ is the thrust force generated by the rotor sail, A_{rotor} is the total-projected rotor sail area, and ρ_{air} is the density of air, taken at $20°\mathrm{C}$ (The Engineering ToolBox, 2003). To calculate the forces, arbitrary values of $AWS = 20\,m/s$ and $AWA = 90°$ are used. These conditions are very favourable for WASP operation and can clearly illustrate the difference in engine operational points implied by WASP systems.

$$F_{x,WASP} = C_x \cdot A_{rotor} \cdot \frac{1}{2}\,\rho_{air} \cdot AWS^2 \tag{5.20}$$

The propulsive force from the propeller is calculated using Equation 5.21. This force is used to calculate the thrust required by the ship propeller (Equation 5.22), which in turn can be used in the open water diagram using Equation 5.23 (Prof. Dr. Ir. Kuiper, 2003).

$$F_{prop,WASP} = R - F_{x,WASP} \tag{5.21}$$

$$T_{prop,WASP} = \frac{F_{prop,WASP}}{1-t} \tag{5.22}$$

$$K_{T,ship,WASP} = \frac{T_{prop,WASP}}{\rho \cdot v_a^2 \cdot D_p^2} \cdot J^2 \tag{5.23}$$

The open water diagram is shown in Figure 5.16. This diagram shows that the propeller efficiency will increase in WASP operation. This is consistent with findings in chapter 2. The efficiency will increase since the thrust from the propeller decreases, while the advance speed at the propeller remains equal.

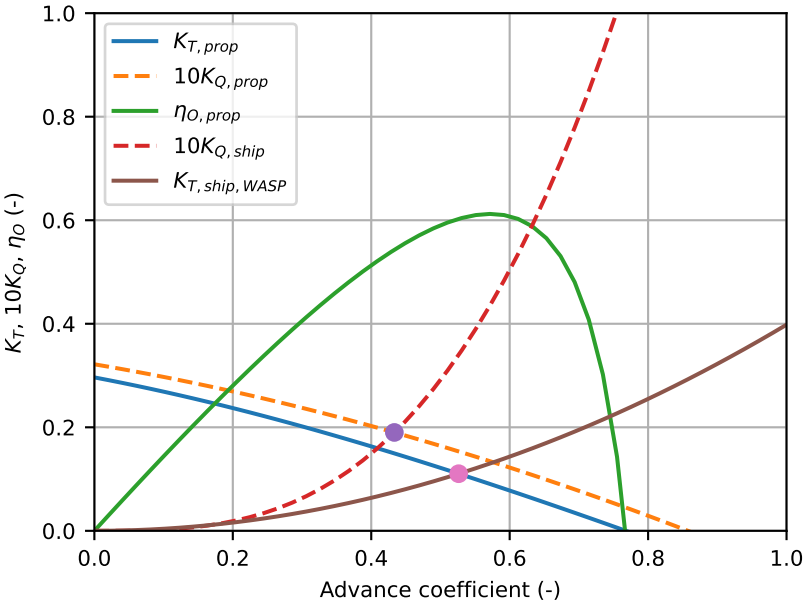

Figure 5.16: Example of propeller open water diagram, with and without WASP.

The open water diagram again is used to match, in this instance, $K_{T,ship,WASP}$ and $K_{T,prop}$, to find the intersection point. This gives $\eta_{o,WASP}$, $K_{Q,WASP}$, and J_{WASP}. These parameters are used to find the propeller rotational speed (Equation 5.24) and propeller torque (Equation 5.25). Together with the relative rotative efficiency and the shaft efficiency, the brake torque is found (Equation 5.26). Finally, this leads to engine brake power (Equation 5.27), which can be plotted in the engine load diagram (Figure 5.17).

$$n_{p,WASP} = \frac{v_A}{J_{WASP} \cdot D_p} \tag{5.24}$$

$$Q_{prop,WASP} = K_{Q,WASP} \cdot \rho \cdot n_{p,WASP} \cdot D_p \tag{5.25}$$

$$M_{B,WASP} = \frac{Q_{prop,WASP}}{\eta_R \cdot \eta_S} \tag{5.26}$$

$$P_{B,WASP} = M_{B,WASP} \cdot n_{p,WASP} \cdot 2\pi \tag{5.27}$$

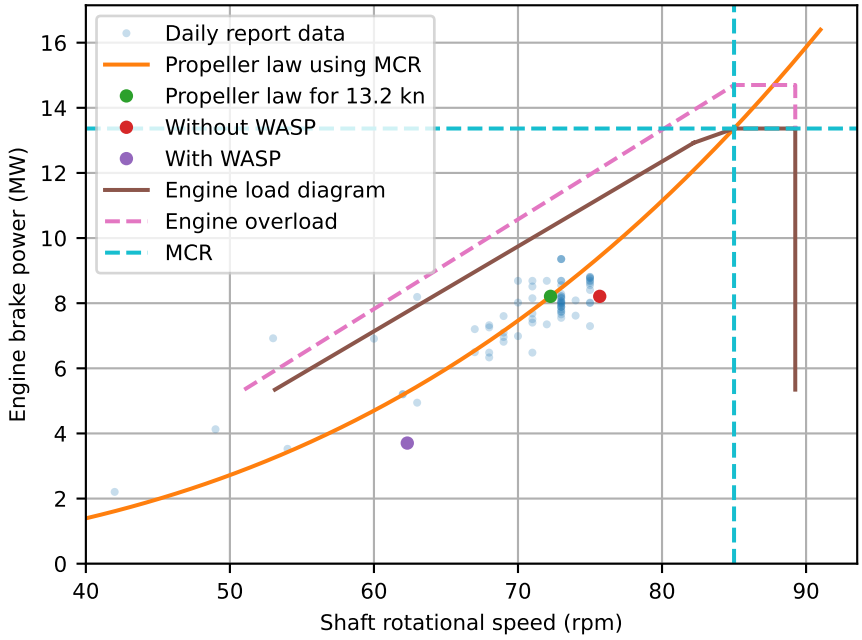

Figure 5.17: Example of engine loads in base and WASP operation using arbitrary wind conditions.

Figure 5.17 shows the engine load diagram, with various stationary engine operating points. The daily report data deviates from the propeller law. A plausible reason for this is due to external factors, for instance, hull fouling and weather conditions. Logging errors might also explain outliers. The figure also shows the data point for a ship speed of 13.2 knots according to the propeller law. The 'without WASP' data point is equal in power, but lies at a higher rpm value. This indicates that the model underpredicts the engine torque. The reason for this underprediction may be due to the estimation of the thrust deduction factor, wake fraction, and propeller characteristics, as discussed in section 5.4.

Furthermore, the figure shows the engine operating point for WASP operations. As seen, in these wind conditions, the WASP system is able to take much of the required ship thrust at 13.2 knots. This is a result of the assumed favourable wind conditions.

5.10. Assumptions

The development of the components discussed in Figure 5.1 have been discussed. A steady-state model can be developed using this information. This is discussed in the next chapter. The assumptions in this chapter are summarised below.

- Resistance:
  - Square relation with ship speed (Klein Woud & Stapersma, 2002).
  - No added resistance due to WASP side forces or rudder angles. This would require a multiple DoF model (Tillig & Ringsberg, 2019).
  - No added resistance due to the projected area of the rotor. Air resistance is by far the smallest of the vessel resistance components (Carlton, 2018). Furthermore, from the frontal view, the vessel already exposes approximately $960\,\mathrm{m}^2$ of above-water frontal area ($670\,\mathrm{m}^2$ from the bow and $290\,\mathrm{m}^2$ from the superstructure). The rotor adds $112\,\mathrm{m}^2$, corresponding to roughly 12% extra frontal area. Although this suggests that the rotor could have some effect on the resistance when not operated, it is expected to contribute only marginally to the total resistance of the vessel.
- Efficiencies:
  - Constant engine efficiency. This assumption is reasonable down to 50% of the MCR (MAN Energy Solutions, 2009)
  - Constant shaft efficiency of 0.99.
  - Estimated relative rotative efficiency of 1.02, assumed to be constant. The value is reasonable, and for small values, the leeway angles during WASP operations does not have a noticeable effect on this parameter (Schot & Eggers, 2019).
  - Varying propeller efficiency, calculated using an approximated propeller design. The increasing propeller efficiency during WASP operations is as expected according to the literature.
  - Approximated and constant thrust deduction factor and wake fraction. The propeller loading has an effect on these parameters, which are omitted in this study. For the leeway effects, larger vessels are less sensitive to changes in the wake fraction (Schot & Eggers, 2019).
- Rotor operations:
  - Lift and drag coefficients for a finite AR (3D coefficients) calculated using interpolation of data from model tests. The 2D and 3D coefficient indicate deviant results, mainly in the drag coefficient.
  - Constant spin ratio of 4. In practice, the spin ratio may vary for AWA, resulting in lower values, thus lower thrust contribution (see section 5.8).
  - Undisturbed and uniform wind flow at the rotor is assumed. In reality, the turbulent wind layer slows down toward the hull surface because turbulent mixing couples the free stream to the boundary layer and its surface skin friction (Smeets, 2024). This creates a vertical wind-speed gradient. For TWS values of 6 kn or higher, the influence of this gradient is largely confined to the lowest 1–2 m above the surface (Bethwaite, 2008). However, the wind flow may also be disturbed by the equipment on deck, the cargo, or the superstructure, which is also not considered.

- The power required to spin the rotors is not considered in this study. In reality, the power will be delivered by the auxiliary engines. This may lead to an overprediction in fuel consumption. To check this, the required rotor power is calculated using the following equations (Seddiek & Ammar, 2021):

$$U_{rot} = C_{rot} \cdot V_a \tag{5.28}$$

$$P_{con} = \left(\left(\frac{0.455}{\log(Re)^{2.58}} - \frac{1700}{Re} \right) \cdot \rho_a \cdot \frac{U_{rot}^2}{2} \cdot A_r \right) \cdot U_{\mathrm{rot}} \tag{5.29}$$

$$Re = \frac{\rho_A \cdot C_{rot} \cdot V_a \cdot L_{Re}}{\mu} \tag{5.30}$$

  Where U_{rot} is the rotational speed of the rotor sail, C_{rot} is the rotation coefficient (spin ratio), V_a is the AWS, P_{con} is the consumed rotor power, ρ_a is the air density, A_r is surface area of the rotor, Re is the Reynolds number, L_{Re} is the characteristic length of the rotor (the diameter), and μ is the air dynamic viscosity. Using a wind speed of $20\,\mathrm{m/s}$, the consumed power of a single rotor is approximately 25 kW. This is roughly 0.3% of the most common main engine power. The consumed power increases for higher wind speeds, with maximum values around 80–90 kW per rotor for the considered rotor sail size (Seddiek & Ammar, 2021; Tillig & Ringsberg, 2020; Viken, 2022).

Given these assumptions, the results obtained in this study should be interpreted as quantitative outcomes with a certain degree of accuracy. While they may not represent exact real-world values, they are sufficiently reliable to describe and analyse the underlying trends.

6

Steady-state model

This chapter discusses the further development of a 1-DoF steady-state model using the components in the previous chapter. This agrees with a 'level 1' PPP according to the ITTC guidelines shown in Figure 2.17. First, a representative voyage with wind conditions is determined. After this, the steady-state model results are discussed. The results from the steady-state model are used to develop and verify the development of a time-domain model, discussed in chapter 7.

6.1. Simulated voyage

As discussed in chapter 4, the T-class vessels have been sailing across the North Atlantic Ocean between North America and Europe regularly. The daily report data of the Triumph during these voyages has made it possible to create a ship model that estimates the performance of this vessel on this route.

A generic route between Europe and North America has been chosen to simulate the performance of the Triumph with WASP. This route is shown in Figure 6.1. Weather routing has not been considered in this instance. The waypoints of this route are given in Table 6.1.

Table 6.1: Simulated route waypoints.

Longitude (°)	Latitude (°)
7.911	53.960
4.615	53.789
3.129	52.754
1.357	50.736
-4.774	49.297
-28.633	47.701
-56.146	43.149
-66.241	41.024
-71.225	41.042

The length of this voyage is approximately 3419 nautical miles. The duration of the voyage is calculated by dividing the route length by the constant ship speed (see Equation 6.1). The voyage is estimated to be 259 hours.

$$t_{totalVoyage}\,(hours) = \frac{3149}{13.2}\,\frac{nm}{kn} \approx 259\,hours \tag{6.1}$$

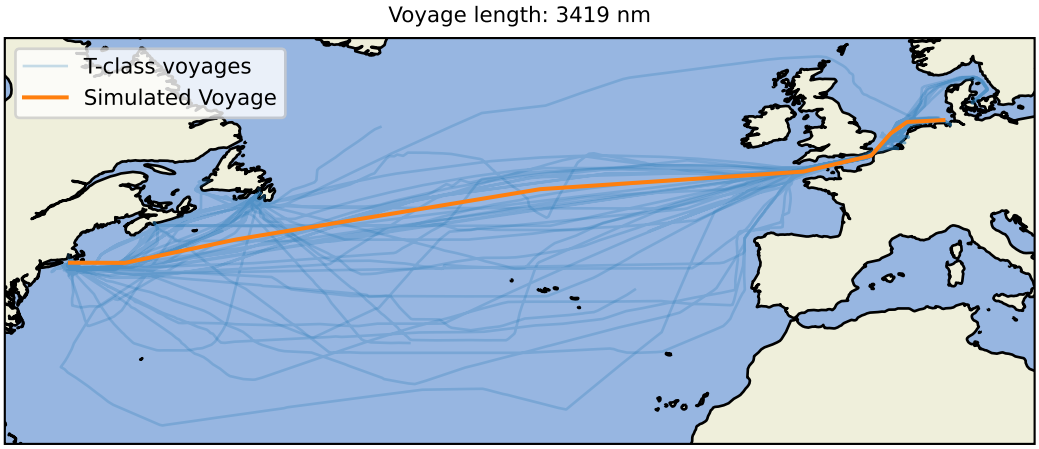

Figure 6.1: Simulated voyage (Boskalis, 2026c).

6.2. Available data

Now that a generic route has been established, the wind conditions during a typical voyage have to be acquired. The most accurate data would be to use actual measured wind data from the vessels. The T-class vessels do have wind data sensors available, which measure apparent wind conditions, but this data is not logged. Furthermore, the heavy marine transport department calculates wind conditions for all the voyages of all the vessels in the HMTV fleet. The most probable maximum for a duration of three hours with a probability of 95% is calculated every fifteen minutes. These conditions are used to calculate the possible accelerations that could result from these wind conditions. It would be incorrect to use these calculations for the assessment of the performance of a WASP system, since these values are probable maxima.

The analysis of available data has made it clear that there are no wind conditions data ready to use for the assessment of the WASP performance. Therefore, this study adopts statistics for this route. The IMO created guidelines for the Energy Efficiency Design Index (EEDI) calculation for innovative energy efficiency technologies, including WASP (IMO, 2013). The document describes that the available effective power of a WASP system can be calculated using Equation 6.2.

$$(f_{eff} \cdot P_{eff}) = \left(\frac{0.5144 \cdot V_{ref}}{\eta_T} \sum_{i=1}^{m} \sum_{j=1}^{n} F(V_{ref})_{i,j} \cdot W_{i,j} \right) - \left(\sum_{i=1}^{m} \sum_{j=1}^{n} P(V_{ref})_{i,j} \cdot W_{i,j} \right) \tag{6.2}$$

In this equation, $f_{eff} \cdot P_{eff}$ is the available effective power of a WASP system. These two factors are combined since the product of availability and power is a result of a matrix operation. The V_{ref} is the reference ship speed in knots, converted to meters per second using the factor 0.5144. The factor η_T is the total efficiency of the drive train of the considered ship. Furthermore, $F(V_{ref})$ is the force matrix of a wind propulsion system for a given ship speed, and $W_{i,j}$ is the global wind probability matrix. An example of the lay-out of a wind probability matrix is given in Figure 6.2. At last, the required power to operate the wind propulsion system is accounted for using $P(V_{ref})$.

wind angle [°] / wind speed [m/s]	0	5	…	355
<1	$w_{1,1}$	$w_{1,2}$	…	$w_{1,72}$
<2	$w_{2,1}$	$w_{2,2}$	…	$w_{2,72}$
<3	$w_{3,1}$	$w_{3,2}$	…	$w_{3,72}$
⋮	⋮	⋮	⋱	⋮
≥25	$w_{26,1}$	$w_{26,2}$	…	$w_{26,72}$

Figure 6.2: Lay-out of the global wind probability matrix (IMO, 2013).

An equation for the determination of the effective force can be determined from Equation 6.2:

$$f_{eff} \cdot F_{eff} = \sum_{i=1}^{m} \sum_{j=1}^{n} F(V_{ref})_{i,j} \cdot W_{i,j} \tag{6.3}$$

It should be noted that the losses due to the operation of the rotor sail are not considered in this equation by only considering the effective force. To use this equation, a matrix should be derived for the available rotor forces for different wind conditions, and a wind condition probability matrix for the route should be found.

6.3. True wind conditions

The wind probability matrix is obtained using the MARIN Blue Route application (MARIN, 2025), a tool developed to evaluate the performance of generic WASP-equipped vessels. Within this application, a route can be defined for which the corresponding true wind conditions along the voyage are computed. The resulting wind rose plots, shown in Figure 6.3, present the probability of occurrence of each wind condition for both directions of the voyage. These probabilities are provided on an annual basis, which is advantageous for this study, as it enables the performance assessment of the Triumph to be based on representative yearly averages.

The information from Blue Route is extracted twice: one for the voyage from Europe to North America, and one for the returning voyage. Figure 6.3 shows that the trip from EU-NA is not very favourable for WASP since the most probable true wind conditions are headwinds. The probability of apparent headwinds will only increase for a ship sailing into these true headwinds. However, the NA-EU route shows promising true wind conditions, consisting of high probability values for tailwinds, favourable for the apparent wind conditions of a wasp-equipped vessel.

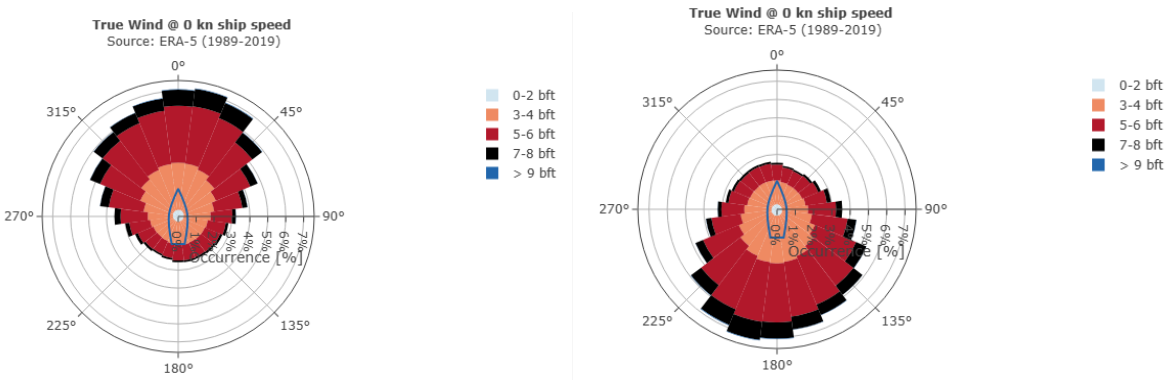

(a) EU-NA voyage **(b)** NA-EU voyage

Figure 6.3: True wind on modelled route (MARIN, 2025).

The statistics from Blue Route are given from 0–$25\,(m/s)$ with a step of $1\,m/s$, and from $0°$–$355°$ with a step of $5°$. This is the same lay-out as indicated in Figure 6.2. One thing that should be noted is that the data from Blue Route adopts the NED-coordinate system, while this study makes use of the NWU-coordinate system. That means that the true wind angles should be converted from NWU to NED. The probability of occurrence for different wind conditions for the different routes in the NED-coordinate system are shown in Figure 6.4.

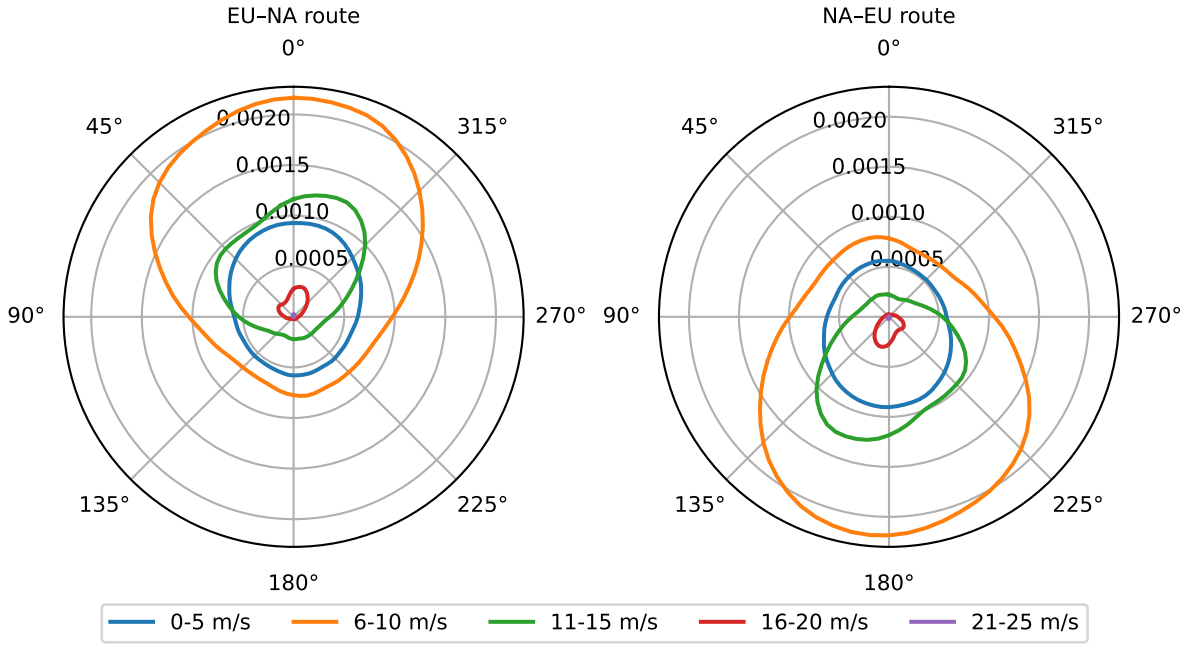

Figure 6.4: Probability of occurrence of true wind conditions on the simulated voyage. Based on MARIN (2025).

6.4. Rotor sails thrust force

The WASP forces for the true wind conditions discussed in section 6.3 should be calculated to estimate the performance of the rotor sails on both routes. The thrust force coefficient for the rotor sail in different true wind conditions is shown in Figure 6.5a. This figure shows that the rotor sail will generate negative forces for true headwinds with angles up to $30°$ from the bow. This is due to the created drag of the sail, recognised in Figure 5.15.

These negative forces are a particular issue for the EU-NA route, where the most probable wind conditions are headwinds, as shown in Figure 6.4. Under these conditions, Equation 6.3 gives negative thrust for the EU-NA route. However, in practice, the operator would stop the rotor sail in conditions were it produces negative thrust. Therefore, the negative values from the force matrix are disregarded, resulting in a force matrix only containing positive thrust values. Mind that in the real case, the rotors would still produce drag even if they are not spinning, due to the exposed area. The extra drag is however not considered. Furthermore, it is assumed that the rotor sails will not produce any thrust with wind conditions of Beaufort scale 8 or higher (Kuo, 2020). The rotor forces for wind speeds of 18 m/s or higher are therefore set to zero.

The thrust force of the rotor sail in different true wind conditions is shown in Figure 6.5b. This figure indicates no negative rotor sail forces, as discussed. Furthermore, the wind speeds go up to 17 m/s in this figure. As seen, the TWA of the maximum thrust force is not equal to the TWA of the maximum thrust coefficient. This is due to the fact that the force increases with the AWS squared, which is higher for beam winds compared to tailwinds.

The components for Equation 6.3 have been determined. This means that the forces can be calculated. The following values have been found:

- No WASP: $f_{eff} \cdot F_{eff} = 0\,\mathrm{N}$
- WASP on route Europe-North America (EU-NA): $f_{eff} \cdot F_{eff} = 22301.1\,\mathrm{N}$
- WASP on route North America-Europe (NA-EU): $f_{eff} \cdot F_{eff} = 33575.7\,\mathrm{N}$

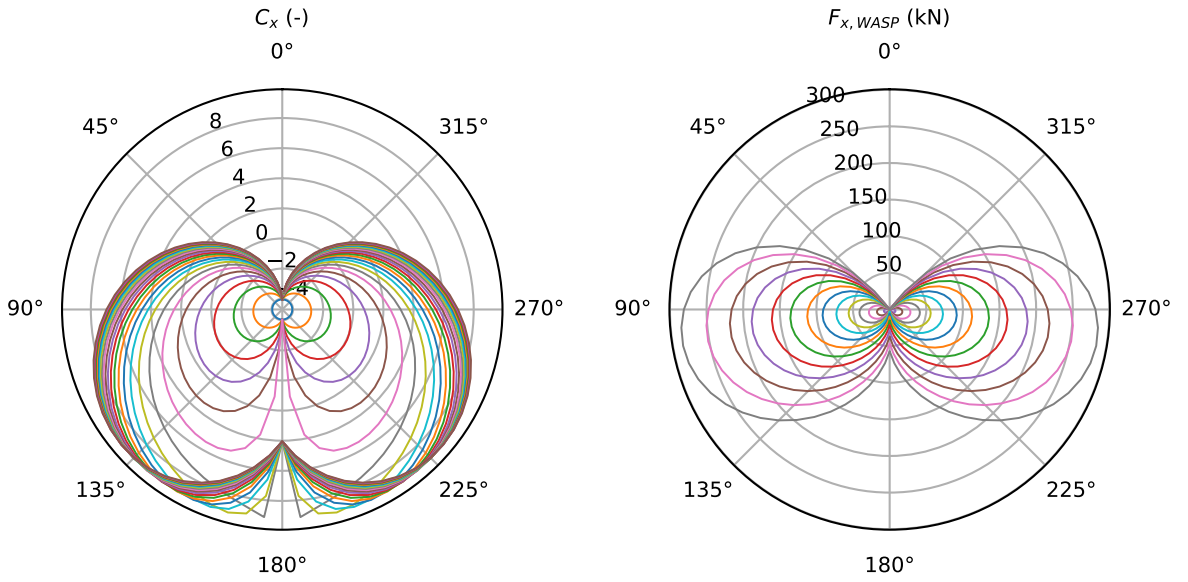

(a) Force coefficient (-). The lines indicate increasing wind speeds, 0–25 m/s.

(b) Rotor thrust forces (kN). The lines indicate increasing wind speeds, 0–17 m/s. Negative forces are not considered.

Figure 6.5: Force coefficients and values for different true wind conditions.

6.5. Stationary engine points

The stationary engine operating points, using the same methodology as described in section 5.9, are calculated using these rotor sail forces, as shown in Figure 6.6. This plot indicates that the engine has to deliver less power, which means that the WASP forces are creating positive thrust.

Even though the wind conditions for NA-EU are more favourable, the engine operating point does not strongly differ from the EU-NA route. This is due to the apparent wind speed. On the EU-NA route, a TWA below $90°$ or above $270°$ is more probable compared to other TWA values. For these angles, the ship speed is causing the AWS to be higher, leading to higher forces. On the NA-EU route, a TWA of $90°$–$270°$ is more probable, giving the opposite result.

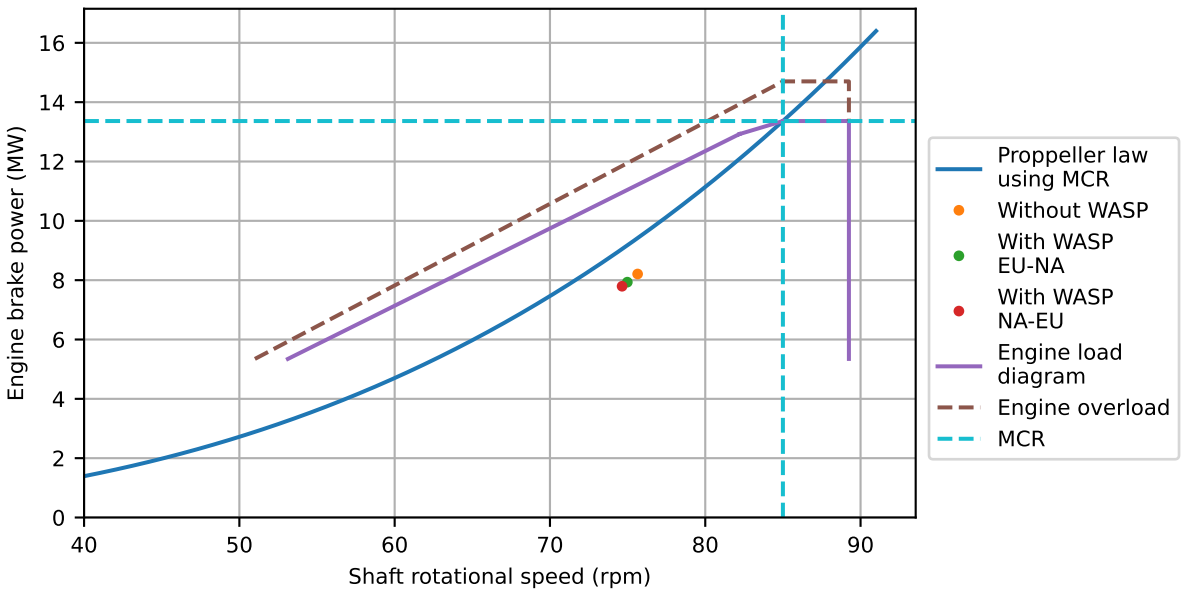

Figure 6.6: Engine load during WASP operation, steady-state model.

6.6. Fuel consumption and emissions

The reduced engine load would consequently lead to a reduced fuel consumption, since the engine efficiency is assumed to be constant. The fuel consumption is calculated using the SFOC described in section 5.7. The fuel consumption for the voyages is shown in Figure 6.7. This shows that the route from EU-NA would lead to less fuel savings compared to the route NA-EU, because the latter has more favourable wind conditions.

The emissions are calculated using the emission factors presented in section 5.7. The results in Figure 6.7 show the absolute values for the considered emissions and indicate a reduction in all emission types. The relative reductions in CO_2 and SO_x emissions correspond directly to the fuel savings, as these emissions are directly proportional to the fuel consumption. For the remaining emission types, the assumed linear relationship with fuel consumption leads to relative reductions identical to the fuel savings. However, as discussed in subsection 2.4.1, the emission formation mechanisms indicate that the relationships for these emissions are not directly proportional in reality. Therefore, Figure 6.7 reports only the relative CO_2 and SO_x emissions.

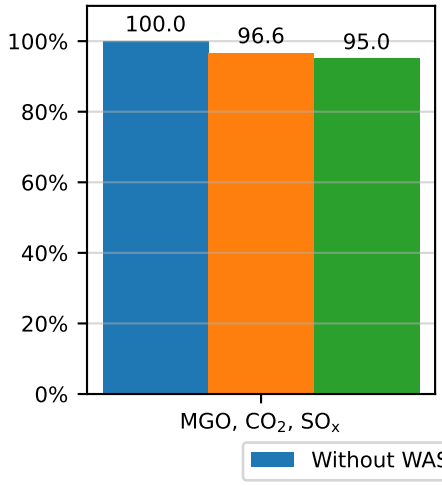

	No WASP	WASP EU–NA	WASP NA–EU
MGO (t)	404.37	390.81	384.01
CO_2 (t)	1296.40	1252.95	1231.14
SO_x (t)	0.57	0.55	0.54
BC (kg)	16.17	15.63	15.36
NO_x (t)	36.14	34.93	34.32
PM_{10} (t)	0.38	0.37	0.36
CH_4 (kg)	21.26	20.55	20.19
CO (kg)	93.54	90.41	88.83
N_2O (kg)	63.78	61.64	60.57
NMVOC (t)	1.34	1.30	1.28

Figure 6.7: Relative and absolute emissions, steady-state model.

The results indicate that applying WASP will lead to fuel savings and emission reductions on both voyages. The savings on the NA-EU route are higher compared to the EU-NA route due to more favourable wind conditions.

7

Time-domain model

The time domain model is created with Python using the components in the steady-state model. This model is based on the model presented in de Vos (2015), with adjustments, such that a rotor sail force could be introduced. The diagram in Figure 7.1 shows the different components and their relation in the model. The blue components are present in de Vos (2015), and the green components are added in this study. It should be noted that the disturbance factor, which can be used to change the ship resistance, is shown in the diagram in dotted lines. This factor is included in the model, but not considered during calculations.

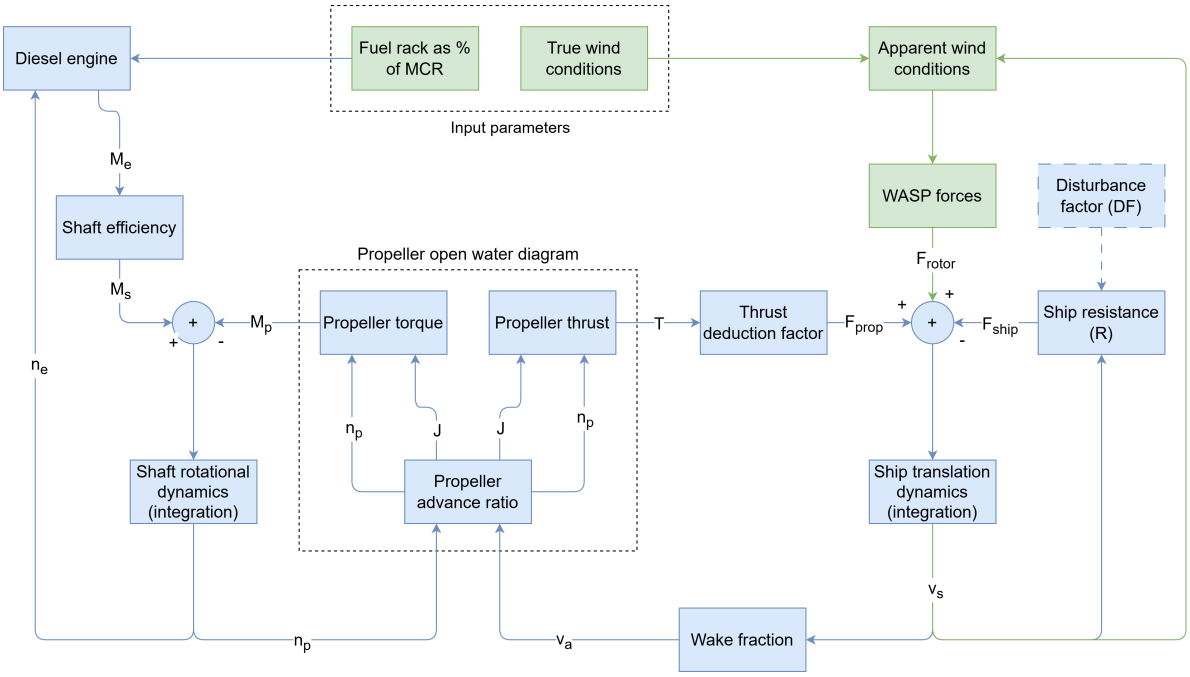

Figure 7.1: Diagram of time simulation model. The blue components are present in de Vos (2015), the green components are added in this study.

The diagram in Figure 7.1 essentially shows the same calculation steps as explained in chapter 5. The ship resistance is calculated using the cube law. The wind conditions and ship speed lead to the apparent wind conditions, and subsequently, the WASP forces. The propeller open water diagram is used to determine the propeller thrust and torque from the advance ratio and the shaft rotational speed. The differences with the steady-state model are the ship translation and shaft rotational dynamics, and the addition of a diesel engine block.

The ship translational dynamics block is the block that integrates the dynamics of the ship resistance, the rotor sail thrust force, and the propeller thrust force. The ship is accelerating if the sum of these forces are not equal to zero. When assuming that the mass and added mass of the vessel remain constant, the change in momentum can be expressed using Equation 7.1 (Kuo, 2020).

$$\frac{dv_s}{dt} = \frac{F_{prop} + F_{rotor} - F_{ship}}{m_{ship}} \tag{7.1}$$

In this equation, m_{ship} is thus the mass of the ship, plus the added mass in surge direction. This added mass is assumed to be 8% of the displacement of the vessel (Δ) (Journée & Massie, 2008).

$$m_{ship} = \Delta \cdot 1.08 \tag{7.2}$$

The diesel engine block calculates the engine torque due to the present engine rotational speed and the fuel rack, which is an input setting, and modelled to be a percentage of the MCR of the engine (Equation 7.3). This only holds for constant engine efficiency, which is assumed in this study, as discussed in section 5.10.

$$P_B = M_B \cdot 2\pi \cdot n_e \quad \rightarrow \quad M_B = \frac{P_B}{2\pi \cdot n_e} \tag{7.3}$$

The shaft rotational dynamics accounts for differences in the shaft and the engine torque. A non-zero value leads to an acceleration of the shaft. Equation 7.4 holds if the total mass moment of inertia I_{tot} remains constant (Stapersma & Vrijdag, 2017), which is assumed in this study.

$$\frac{dn}{dt} = \frac{M_{shaft} - M_{prop}}{2\pi \cdot I_{tot}} = \frac{M_{eng} \cdot \eta_s - M_{prop}}{2\pi \cdot I_{tot}} \tag{7.4}$$

In this equation, the total moment of inertia contains the shaft, propeller, and the entrained water in the propeller. The propeller values I_p have been given in the Meridian propeller data (see Table 5.1). Furthermore, internal documentation contains information about the propeller shaft and the intermediate shaft weights m_s and diameter D_s. The total moment of inertia is calculated using Equation 7.5 (Leijendeckers & Beke, 2004).

$$I_{tot} = I_p + I_s = I_p + \left(\frac{1}{2} \cdot m_s \cdot \left(\frac{D_s}{2} \right)^2 \right) \tag{7.5}$$

7.1. Differential equation solver

The shaft rotational speed and the ship speed are solved numerically using an ordinary differential equation solver. The SciPy function `solve_ivp` is used in this study (SciPy, 2026a). The solver numerically integrates a system of Ordinary Differential Equations (ODE)s with a variable time step. The required initial conditions are determined using the steady-state model.

The solver can integrate a system of equations using different methods, which can be categorised as explicit and implicit. The user must select either an explicit or an implicit integration method. The explicit methods are suited for non-stiff problems, while the implicit methods are suited for stiff problems. When an explicit method is applied to a stiff system, the algorithm is forced to keep the variable time step small because it cannot find a stable solution. A simple way to find the nature of the system is therefore solving the system during a test run using different methods and analysing the variable time step size. Figure 7.2 shows this process. In this figure, the 'RK23' and 'RK45' are explicit Runge-Kutta methods of the order 3 and 5, respectively. Radau and the Backward Differentiation Formula (BDF) are implicit methods of order 5 and of variable order, respectively. Figure 7.2 shows that this system of equations is stiff, and an implicit method should be used. The BDF method is used because of its low computational cost (Butcher, 2000).

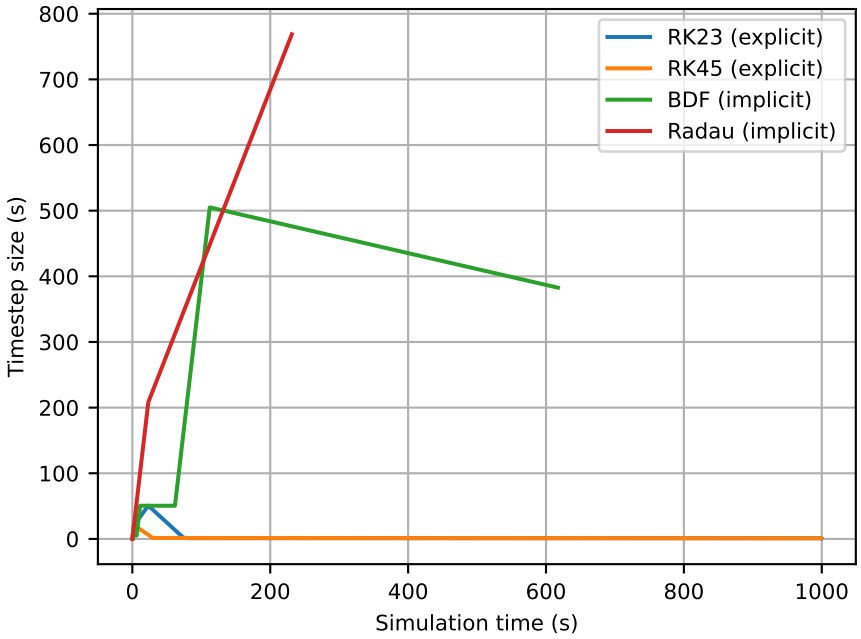

Figure 7.2: Solving the system of ODEs in the time-domain model using different integration methods. The BDF method is used for further modelling.

7.2. Time domain model verification

The time-domain model must be verified against the results of the steady-state model, and its dynamic behaviour should align with physical expectations. Several preliminary checks are performed to ensure this, including:

1. Consistency with stationary behaviour (no WASP).
2. Convergence between steady-states under changing rotor sail forces.
3. Propeller law behaviour with variable fuel rack (no WASP).
4. Propeller law behaviour in WASP operations.

Test 1: Consistency with stationary behaviour, no WASP

The model should reproduce the same brake power as in the steady-state model in stationary conditions. Without disturbances, the ship speed should remain constant. This first check is shown in Figure 7.3. This figure shows that for zero WASP forces, the ship speed and shaft rotational speed are constant.

Test 2: Convergence between steady-states under changing rotor sail forces

When the initial condition corresponds to zero rotor sail forces and the final condition to a non-zero rotor sail force, the model should converge from the initial steady-state to the final steady-state. Figure 7.3 shows that the initial conditions are zero AWS and an AWA of $90°$. The wind speed slowly increases to 20 m/s, keeping the AWA at $90°$. This final condition is identical to the condition described in section 5.9. The required engine power at the final condition is calculated using the steady-state model. The shaft rotational speed converges correctly from the initial condition to the final condition.

The results for test 2 in Figure 7.3 shows that the ship speed is decreasing during the first part of the simulation. This is caused by the fact that the fuel rack is not adjusted according to the amount of available WASP force. Instead, the fuel rack is slowly decreasing from the initial to the final condition. This is causing a decrease in ship speed. A changing fuel rack according to the available WASP force, designed to keep a constant ship speed, would be a more accurate modelling method.

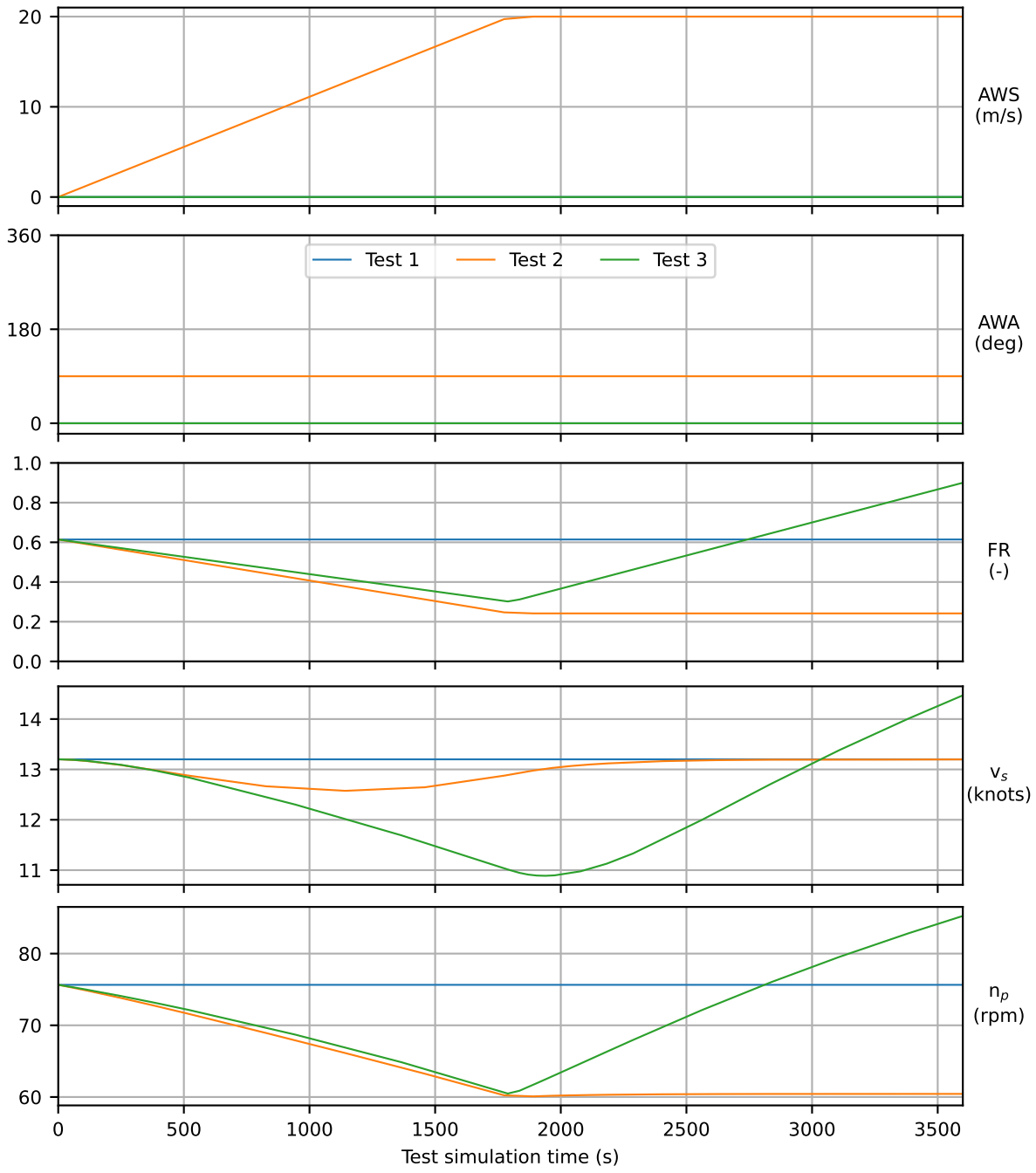

Figure 7.3: Time-domain model test outputs.

Test 3: Propeller law behaviour with variable fuel rack, no WASP

In normal operation (without WASP forces), the engine operational points should follow the propeller law (as described in section 5.6), because the efficiencies in the propulsion chain (Figure 2.8) remain constant.

The fuel rack is varied through simulation time (see Figure 7.3), leading to varying engine operational points. This behaviour is indicated in Figure 7.4. The figure shows the propeller law using the MCR points of the engine, as well as the propeller law constructed with the initial conditions of the simulation. The engine operating points are indeed following the propeller law of the initial condition with some deviations. These deviations may be explained by the influence of the ship translational dynamics on the propeller loading.

The efficiencies in Figure 7.4 shows that the efficiencies remain constant through the test simulations. However, the sudden change in engine power leads to a jump in the propeller thrust, causing a jump in efficiency.

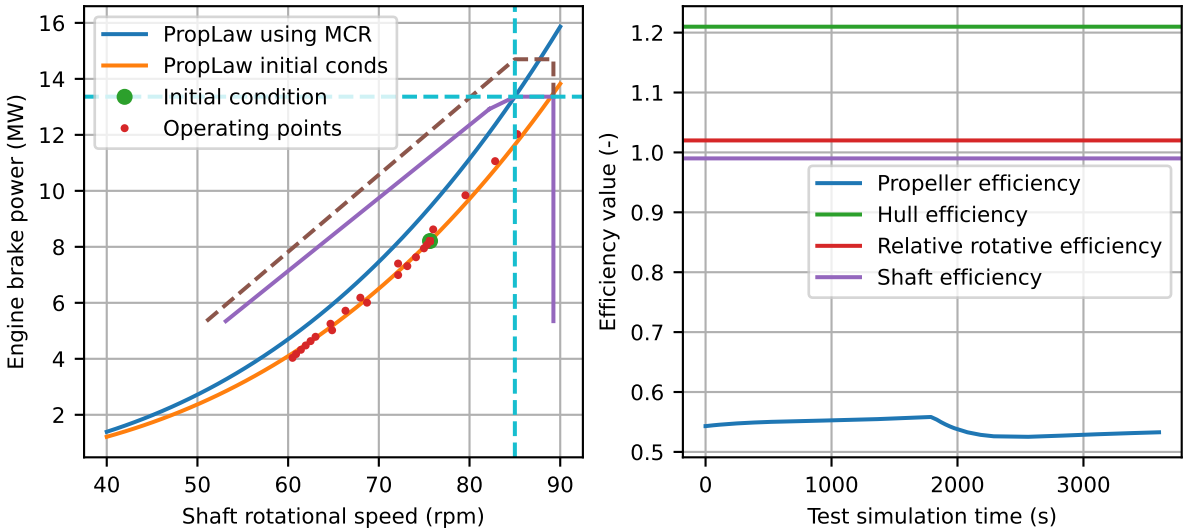

Figure 7.4: Propeller law check and efficiency values during normal operation (test 3).

Test 4: Propeller law behaviour in WASP operations

For variable rotor sail forces, the engine operating points should not follow propeller law, because the propeller efficiency increases. The conditions of test 2 are used to check this behaviour. The results are shown in Figure 7.5. As seen, the engine operational points do not follow the propeller law due to the increased propeller efficiency.

The use of a constant propeller efficiency by Plessas and Papanikolaou (2025) discussed in subsection 2.2.5 is now certain, because the engine operational points in both normal and WASP operations lie on the same curve in the engine diagram, as shown in Figure 2.15a.

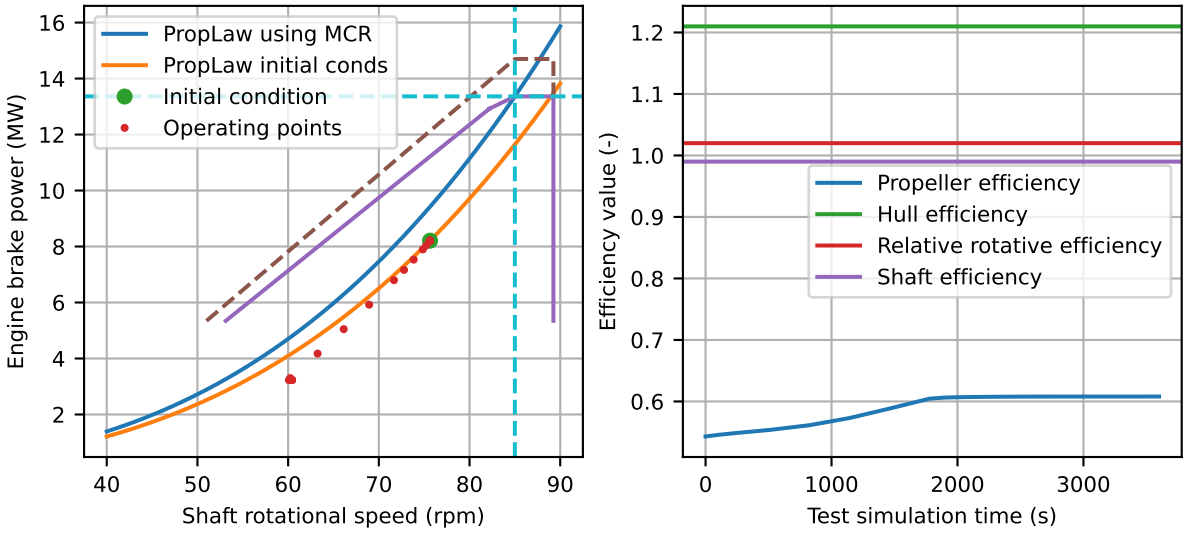

Figure 7.5: Propeller law check and efficiency values during WASP operation (test 4).

7.3. Input parameters

The previous subsection discussed multiple checks for verifying the behaviour of the model. This shows that the model behaves as expected. The next step is to recreate the voyage from Figure 6.1 in this time simulation model. First, the input wind conditions must be determined.

The Marin Blue Route data in Figure 6.3 shows that the most common wind speeds are in 5–6 Beaufort. To create a varying wind speed for the input of the model, an API wind spectrum is created around a mean wind speed value of 10.9 m/s (the mean wind speed of Beaufort 5 and 6 (see KNMI (2026))) using OrcaFlex software, internally available at Boskalis (OrcaFlex, 2026). This spectrum gives a signal for a varying wind speed over one hour, with a time step of 0.1 seconds. This signal is shown in Figure 7.7. The signal is repeated for the voyage duration given in Equation 6.1.

The varying wind speed signal produces AWS values that occasionally fall outside the Beaufort 5–6 range, as shown in Figure 7.7. However, the majority of the values remain within this envelope. This signal is considered adequate for use in further calculations.

The wind angles are determined using the true wind probability matrix defined in Equation 6.3. Only the values for a wind speed of 8, 9, 10, 11, 12, and 13 m/s (approximately the wind speeds within Beaufort 5–6) are considered. The probabilities for every wind speed at a certain angle are now summed and normalised with the total probability of the considered wind speeds. Therefore, a new matrix is found: a matrix which contains the probability values of Beaufort 5–6 wind speeds at varying angles. The method for this is schematically shown in Figure 7.6.

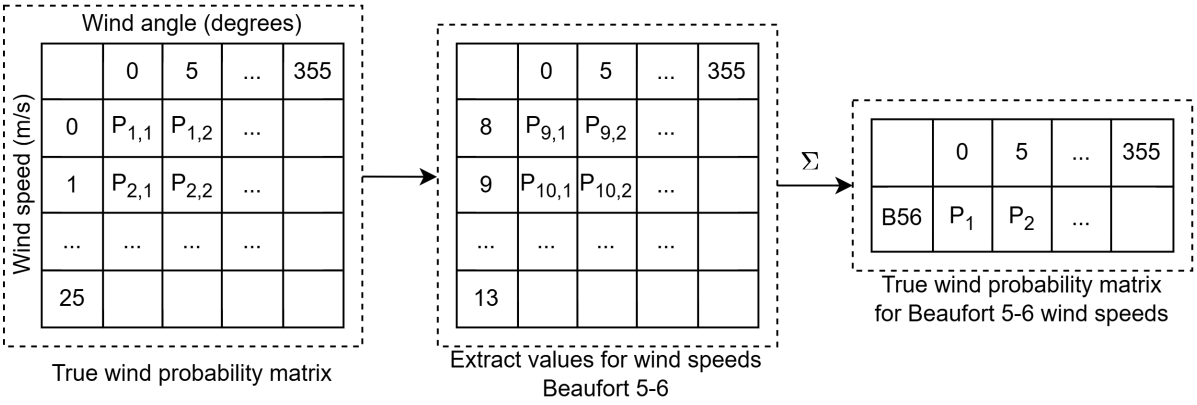

Figure 7.6: Finding wind angle probability values for Beaufort 5–6 wind speeds.

This new matrix gives the probability of occurrence of a certain wind angle during a voyage with Beaufort 5–6 wind speeds. To model different wind angles during a voyage, the assumption has been made that the vessel will start sailing with a TWA of zero degrees, and encounter every possible TWA during the voyage. The time that a certain angle has been encountered is the probability value of that wind angle times the total voyage time. For instance, if the voyage time is one hour and the probability of a zero degree TWA is 5% during that voyage, then the vessel will encounter a zero-degree TWA for $0.05 \cdot 3600 = 180$ seconds. After this time, the TWA shifts to 5 degrees, and so on, until 355 degrees. This finally adds up to a slowly varying wind speed during the voyage. The values for the TWA for the EU-NA and the NA-EU route are shown in Figure 7.7. This figure shows that the TWA for the NA-EU route will be sideways for longer periods compared to the EU-NA route, which is a result of the wind rose plot shown in Figure 6.3. The true wind conditions are converted to apparent wind conditions using the ship speed during the simulation.

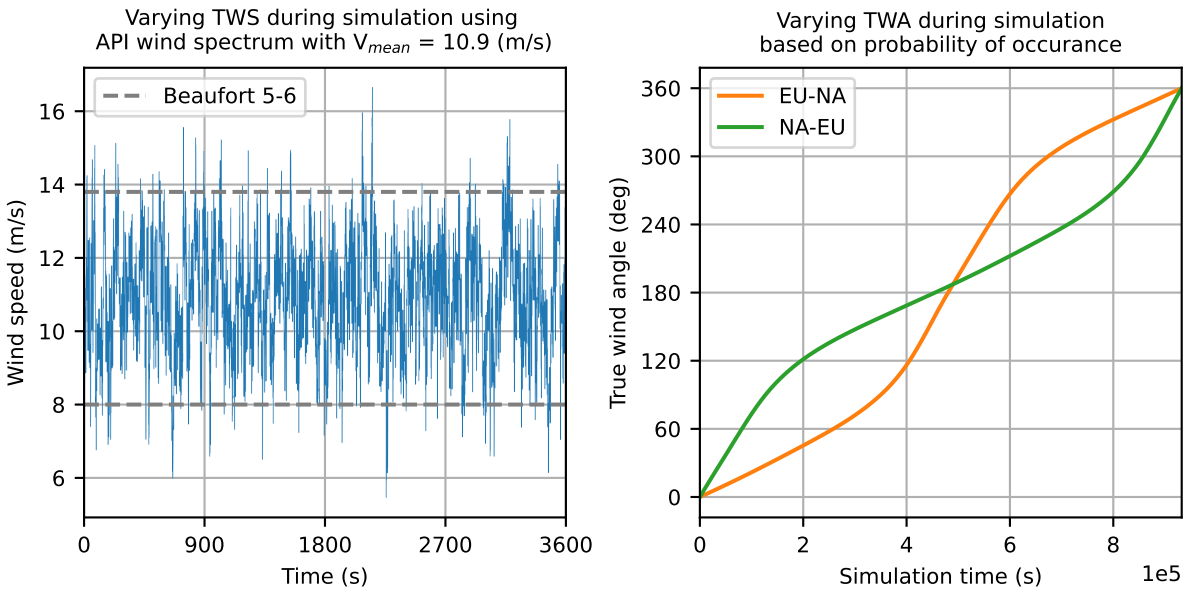

Figure 7.7: Time-domain model input signals.

It should be noted that the assumption of a desired constant ship speed of 13.2 knots is assumed during these simulations. A positive rotor force causes a reduction in fuel rack, resulting in a constant ship speed of 13.2 knots. Like the steady-state model, negative WASP forces are excluded from the calculation, because it is still assumed that the ship operator will turn the rotor sails off when creating negative thrust forces. Furthermore, a disturbance factor is present in the model (see Figure 7.1), but is not regarded during simulations.

To maintain a ship speed of 13.2 kn, the required fuel rack setting for each wind angle is first determined using the steady-state model. In the time-domain simulation, the fuel rack adjustment is applied at the moment the wind angle changes. This approach imitates an operator responding to variations in WASP-induced thrust and ensures that the vessel speed remains approximately constant throughout the simulation. A more sophisticated approach would be to incorporate a Proportional-Integral-Derivative (PID) controller for regulating the engine response. However, this is not pursued here in order to maintain modelling simplicity.

7.4. Model outputs

The model is run for the total time of the voyage duration shown in Equation 6.1. The model outputs for the EU-NA and NA-EU route are shown in Figures 7.8 and 7.9, respectively.

The two plots show similar behaviour. The true wind speeds input signals are identical for the two calculations. The true wind angle input signal from Figure 7.7 is recognised. As shown, these true wind conditions are converted into apparent wind conditions. The WASP force F_{wasp} resulting from these apparent wind conditions shows high values for favourable wind conditions and low values for unfavourable wind conditions. Furthermore, the created rotor sail forces correspond to the polar plot of the rotor thrust forces in the steady-state model, as indicated in Figure 6.5b. The F_{wasp} line shows that the negative wasp forces are not regarded in the calculations.

The time step size can be recognised from the input wind signal. The ODE equation solver takes a small time step when the F_{wasp} becomes greater than zero. This is shown by the density of the TWS input signal. This results in a varying ship speed and shaft rotational speed. To avoid too large time steps, the maximum time step value is set to 1000 seconds.

The fuel rack setting is adjusted in response to the WASP force: a higher WASP contribution results in a lower required fuel rack position. This adjustment keeps the vessel operating close to the target mean speed of 13.2 kn. The reduced fuel rack input also leads to a corresponding reduction in the shaft rotational speed.

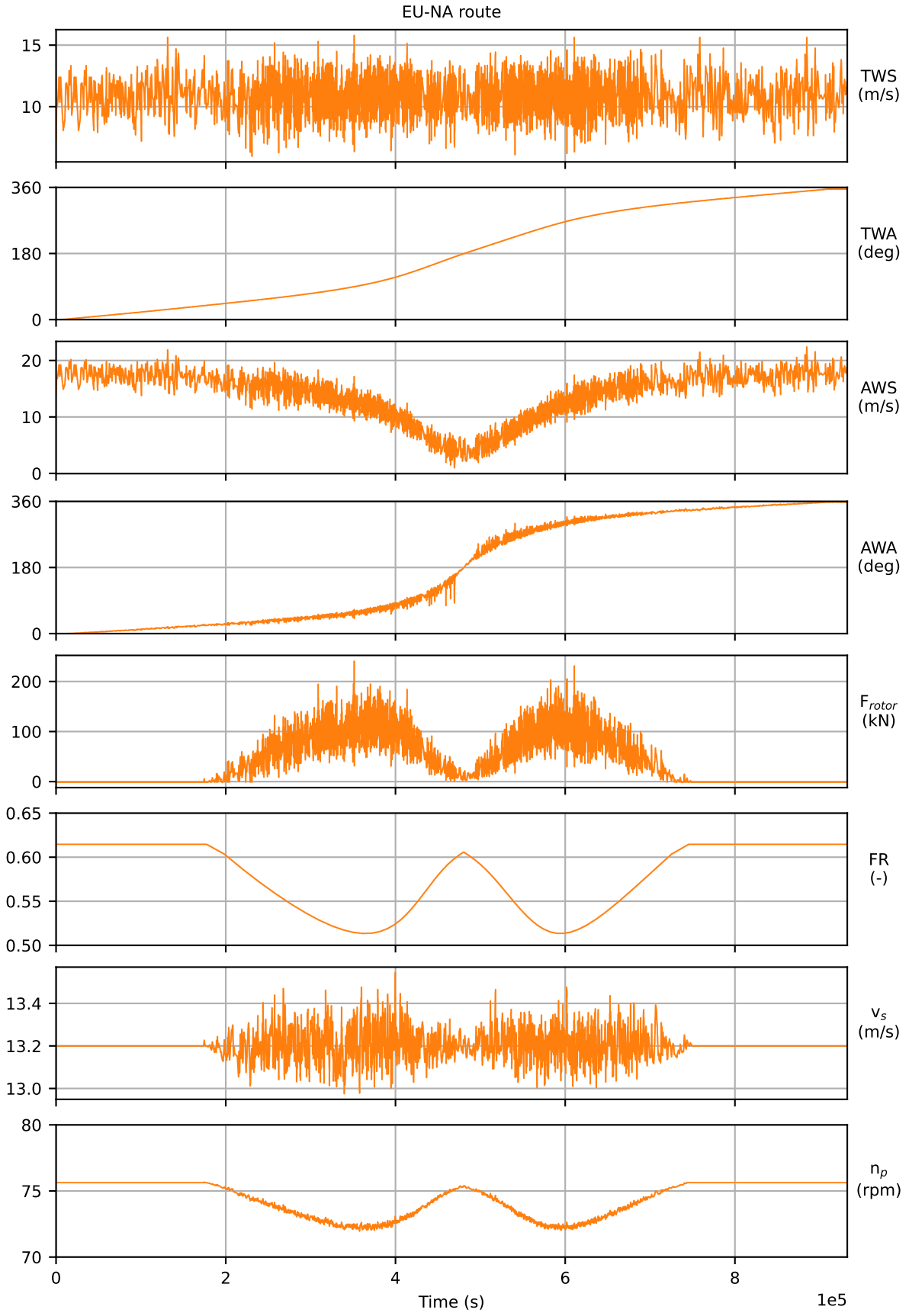

Figure 7.8: Ship model output for the EU-NA route.

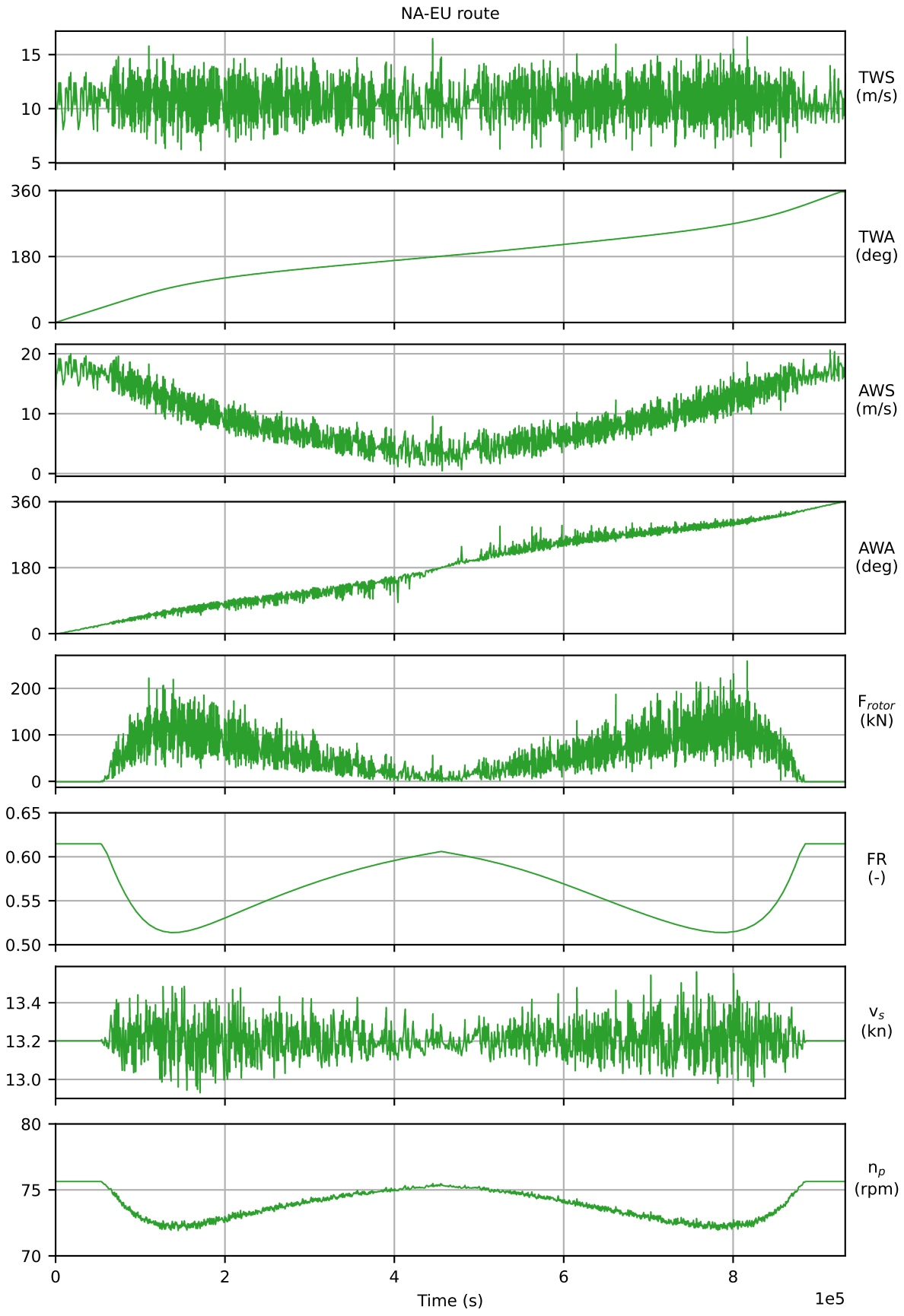

Figure 7.9: Ship model output for the NA-EU route.

7.5. Engine operations

To check the validity of the assumed constant engine efficiency, which is valid down to 50% MCR (MAN Energy Solutions, 2009), but will rapidly decrease below this value (Klein Woud & Stapersma, 2002), the engine load diagrams in the time-domain model are shown in Figure 7.10. As seen, the operational points come close to, but do not exceed, the limit below 50% MCR.

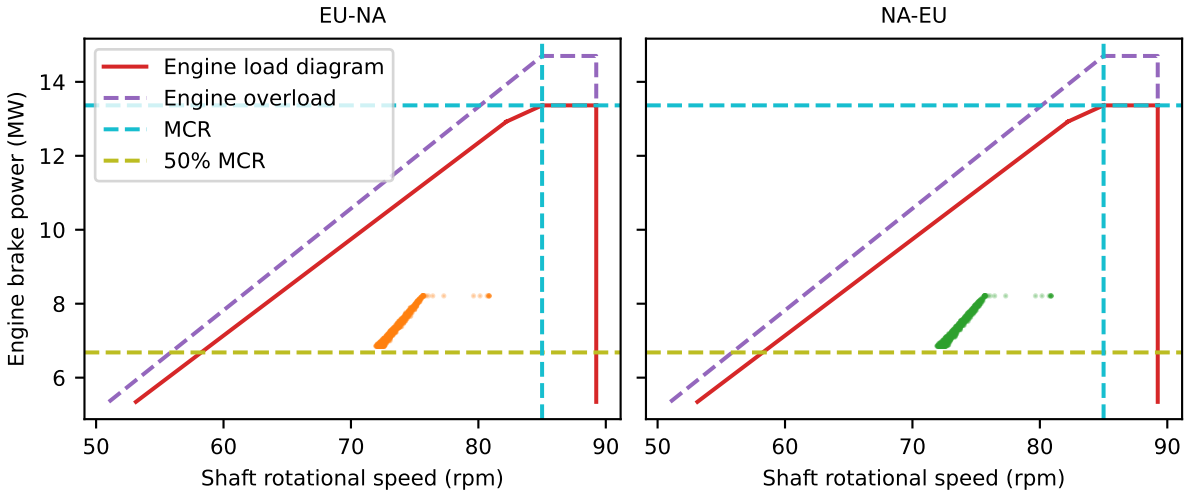

Figure 7.10: Engine load during the time-domain simulation.

Sudden changes in wind speed introduce variations in the WASP forces, which in turn cause small fluctuations in propeller rpm, as observed in the simulations. Because the vessel operates with a directly driven FPP, these variations are transmitted directly to the engine. If sufficiently large, such fluctuations could lead to issues such as thermal overloading of the cylinder liners (Kuo, 2020). To assess this risk, the simulated rpm changes per second are compared to MAN load-up program for engines with FPP (MAN Diesel, 2009), shown in Figure 7.11a. This guideline recommends increasing the engine speed from 80% to 90% MCR rpm over 30 minutes, corresponding to 0.00472 rpm/s. Although intended for engines with an 80 cm bore and above, MAN indicates that following this program is also beneficial for smaller-bore engines such as the S70MC6 (70 cm). The comparison in Figure 7.11b should therefore be viewed only as an indicative reference. The high initial peaks in Figure 7.11b result from model initiation issues. These are also observed in Figure 7.10. Overall, the accelerations caused by the WASP forces remain well below levels that would meaningfully affect engine rpm. Consequently, significant engine load or thermal issues due to the WASP system are not expected.

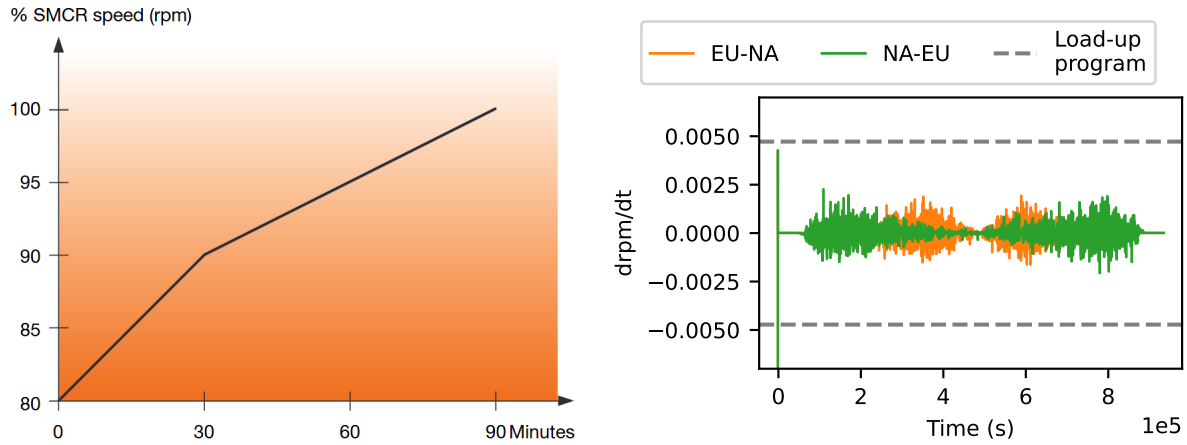

(a) Recommended FPP load-up program (MAN Diesel, 2009).

(b) Variations in shaft rotational speed over time during simulations.

Figure 7.11: Variations in shaft rotational speed compared to the recommended engine load-up program.

7.6. Consumed fuel and emissions

The consumed fuel is not included in the engine block. However, the consumed brake power at every time step is calculated, and the model assumes a constant SFOC. This information can be used to calculate the total consumed fuel during a voyage. First, the fuel mass flow per second can be calculated using the SFOC and the brake power of the engine using Equation 7.7 (Klein Woud & Stapersma, 2002). Then, the total consumed fuel can be calculated by integrating this value over the total simulation time (Equation 7.8). In Python, the NumPy trapezoidal function is used for this (NumPy, 2026).

$$P_B = FR \cdot P_{MCR} \tag{7.6}$$

$$sfoc = \frac{\dot{m_f}}{P_B} \quad \rightarrow \quad \dot{m_f}\left(\frac{g}{s}\right) = sfoc\left(\frac{g}{kWh}\right) \cdot \frac{P_B}{1000}\,(kW) \cdot \frac{1}{3600} \tag{7.7}$$

$$m_f\,(g) = \int_{t_0}^{t_1} \dot{m_f}\,dt \tag{7.8}$$

The relative fuel consumptions for the vessel without WASP, and on the EU-NA route and the NA-EU route with WASP, are shown in Figure 7.12. These relative savings are higher compared to the steady-state model calculations, shown in Figure 6.7. This is due to the fact that the WASP forces in the steady-state model include probabilities of low wind speeds. The time domain model only includes wind speeds approximately within Beaufort 5–6, which results in higher WASP forces. This indicates that the time-domain model may lead to more accurate results during specific weather conditions.

The emissions are calculated using the same method described in section 5.7. Therefore, the first step is to determine the total energy consumed during the voyages. This is done using the relationship between SFOC, fuel consumption, and effective work ($\mathrm{W_e}$) (Klein Woud & Stapersma, 2002), as expressed in Equation 7.9. The corresponding emissions are obtained by applying the conversion factors from Table 5.4. The absolute values for the emissions resulting from the time-domain simulation are shown in Figure 7.12.

$$sfc = \frac{\dot{m_f}}{P_B} = \frac{m_f}{W_e} \quad \rightarrow \quad W_e\,(kWh) = \frac{m_f}{sfoc}\,\frac{(g)}{(g/kWh)} \tag{7.9}$$

The black carbon emissions depend on the engine power during the voyage. This means that the factor must be determined using the same method as for the consumed fuel. The black carbon emission factor is converted from gram/gram to gram/second using Equation 7.10. The black carbon emissions are calculated using Equation 7.11.

$$\dot{BC}_{emission}\left(\frac{g}{s}\right) = BC_{factor}\left(\frac{g}{g}\right) \cdot \dot{m_f}\left(\frac{g}{s}\right) \tag{7.10}$$

$$BC_{emission} = \int_{t_0}^{t_1} \dot{BC}_{emission}\,dt \tag{7.11}$$

The relative CO_2 and SO_x emission savings are related to the steady-state model emissions in Figure 6.7. These relative emissions show higher values compared to the steady-state model because of the higher wind speed input into the time-domain model.

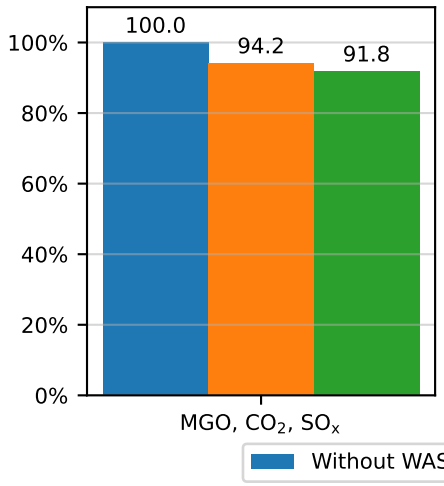

	WASP EU-NA	WASP NA-EU
MGO (t)	380.76	371.41
CO_2 (t)	1220.71	1190.73
SO_x (t)	0.53	0.52
BC (kg)	15.23	14.86
NO_x (t)	34.03	33.20
PM_{10} (t)	0.36	0.35
CH_4 (kg)	20.02	19.53
CO (kg)	88.08	85.92
N_2O (kg)	60.05	58.58
NMVOC (t)	1.27	1.23

Figure 7.12: Relative and absolute emissions, time-domain model.

The time-domain model results show the same general trends as the steady-state model results. The higher fuel savings and emission reductions are caused by the assumed wind conditions. This shows that the time-domain model may give more accurate results for specific voyages. Moreover, the thrust forces created by the WASP systems, leading to a variation in propeller loading and subsequently a variation in engine loading, are not expected to be significantly high to cause problems.

8

Conclusion and discussion

This chapter presents the conclusions drawn from the research, structured around the sub-questions introduced in chapter 1. The discussion hereafter reflects on the limitations of this study and its relevance to the field. Finally, recommendations for further research are given.

8.1. Conclusion

In this section, the main conclusions from the literature review are first summarised. After this, the sub-questions are answered based on the findings in this study, after which the main research question is addressed.

The analysis of current literature shows that the application of WASP is growing consistently and is gaining popularity due to an increasing amount of reported fuel savings. This topic is currently trending in the academic world. The research on WASP is more present in hydromechanics and aerodynamics compared to the marine engineering field. Especially study on emissions due to WASP are limited.

For the Boskalis fleet, which vessel class is most suitable for integrating WASP, and which technology is optimal for that case, based on explicit criteria?

The properties of the vessels in the Boskalis fleet make it more difficult to apply WASP compared to merchant vessels. However, the development of various forms of WASP systems allows for more possibilities. The HMTV and subsea rock installation fleet contain appropriate vessel types for WASP application. Rotor sails generate the highest force per square meter, which makes it suitable for application within Boskalis, since a low footprint of the equipment is desired for these types of vessels.

Which specific vessel within the selected class is most suitable to develop a case study?

The selection of the HMTV fleet for further analyses is mainly due to the operational profile of these vessel types. Within the HMTV fleet, the T-class vessels are most suitable for WASP application, because the discussion of placement on these vessels are the lowest for the entire HMTV fleet.

What are the expected changes in the propulsion efficiencies when integrating WASP, and how can each of these changes be estimated?

Integrating WASP into a vessel induces changes to the hydromechanics and marine operations of a vessel. Some of these effects are more pronounced compared to others. Although a 1-DoF method can capture the primary influences on ship resistance and propulsion, a 3-DoF method is needed at minimum for more advanced analyses. The development of such a complex model requires accurate and complete input data.

Which input data are required to parameterise the propulsion chain estimates and to determine the vessel's wind-assisted engine operations, and how can these inputs be calculated for the selected case vessel?

The available data of the T-class vessels at Boskalis do not allow for accurate modelling of fuel consumption and emissions. However, a 1-DoF model that predicts the engine power for given ship speeds with acceptable accuracy can be developed with the available data. The operational fuel consumption of the vessel shows large scattered data, which makes it difficult to assess the accuracy of this estimation. The WASP force coefficients can be estimated using published literature. An estimation of the actual forces require wind input data.

Using a representative operating profile and data from previous questions, what is the predicted impact of WASP on the engine operations of the vessel?

WASP appears applicable on the Triumph, indicating trends to significantly decrease fuel consumption and emissions. These findings may help reduce internal barriers to the adoption of WASP technologies within Boskalis. Furthermore, the thrust forces created by the rotor sail are not expected to create problems for the engine. The induced WASP forces are insufficient to cause substantial vessel accelerations, and the resulting fluctuations in engine rpm remain well within acceptable limits.

Based on the impact on engine operations, what differences are predicted in exhaust emissions with and without WASP using the IMO emission factors?

The CO_2 and SO_x emissions decrease linearly with fuel consumption. Other emission types appear to decrease as well, due to the use of constant emission factors in this study. This assumption omits the complex relationship between the engine operating parameters and emission profiles.

What is the impact on fuel consumption and emissions when retrofitting an existing heavy marine transport vessel with wind-assisted ship propulsion?

Within the Boskalis fleet, the T-class vessels seem suitable for the application of rotor sails, and the resulting impact will be positive in terms of fuel and emission savings during a typical voyage. These findings are relevant given the increasingly stringent environmental regulations to decarbonise maritime operations, making WASP a viable option to reduce fuel consumptions and emissions, and enhancing fleet sustainability.

8.2. Discussion

This study evaluates the potential of WASP across the Boskalis fleet and quantifies expected reductions in fuel consumption and emissions. The modelling framework combines validated methods from literature with operational ship data and is directly transferable to the sister vessels with only minor parameter adjustments. External applicability is conditional, as the approach assumes a quadratic relationship between ship speed and total resistance and a propulsion train consisting of a two-stroke engine with a fixed-pitch propeller. Under these assumptions, the model provides a plausible and methodologically sound basis for estimating WASP benefits in terms of fuel savings.

The MCDA results indicate that vessels in the HMTV fleet have the highest potential for the application of WASP. This outcome aligns with expectations, as these vessels typically operate over long distances and have transport-oriented mission profiles. These characteristics are commonly associated with successful WASP integration in the literature. The results of the model development further demonstrated it is capable of capturing the relationship between engine power and vessel speed around the vessel's most common operating point with an acceptable level of accuracy. Additionally, the fuel-saving estimates generated by both the steady-state and the time-domain models fall within the range of values typically reported for ship propulsion assisted by rotor sails. Together, these findings support the conclusion that the addition of rotor sails is likely to provide a net positive thrust contribution under representative operating conditions.

The results should be interpreted with caution due to the number of assumptions required throughout the analysis. The criteria used in the MCDA were developed based on the author's understanding and discussions with Boskalis professionals. Consequently, the relative importance assigned to each criterion reflects the priorities of a single operator; other companies may weigh these factors differently, which could influence the ranking of vessel types. In addition, the selected case vessel is relatively old, raising questions about the practical feasibility of installing a new technology. Several important aspects, such as costs, structural integration, ship stability, rotor system sizing and placement, and

operational constraints, were also beyond the scope of this study and therefore not considered, but are important aspects.

Developing the performance prediction model required simplifying assumptions. Many efficiencies were assumed constant, while propeller efficiency was estimated using characteristics of a similar propeller type. The accumulated effect of these assumptions is visible in the mismatch between the modelled and actual engine operating points given in the daily reports. Also, the specific fuel oil consumption data from the daily reports showed that this is particularly difficult to estimate accurately. Moreover, the resistance model does not account for the added resistance or course-keeping corrections associated with WASP, which is consistently reported in the literature. The rotor dimensions are realistic based on existing systems, but their aerodynamic coefficients were approximated, and a constant spin ratio was assumed. This is an unrealistic simplification for real-world operations. The model also omits rotor-power consumption, a non-uniform flow of apparent wind at the rotor sails, and potential negative rotor forces, which all can significantly affect net performance. Furthermore, the calculations do not relate in-cylinder combustion behaviour and emissions.

Further research could enhance the prediction model developed for the Triumph, beginning with relatively simple improvements to the current 1-DoF model. A more representative rotor operation, instead of a constant spin ratio, would already increase accuracy of the findings. In addition, a more systematic investigation of the practical considerations associated with WASP installations, such as feasible sail placement, structural integration, and operational implications, would help clarify which retrofits are realistic for vessels of this type. An analysis of the operational use of the currently developing amount of innovative WASP system designs could also help adoption within Boskalis. By presenting a clear picture of the possibilities, the inevitable discussion on the impact of WASP systems on the versatility of the deck layout may be positively influenced. Research on modelling of engines and emissions could further enhance the accuracy of the emission profiles during WASP operations.

While many of these limitations could be mitigated through relatively straightforward additions, achieving more reliable results ultimately requires access to more detailed operational and design data. A more comprehensive assessment of data availability at the start of the research could have reduced development time and enabled a stronger focus on refining the model, thereby improving the accuracy and robustness of the conclusions. The analysis would have benefited from a concise overview of the available data per vessel. To reduce modelling efforts in future research, it is recommended that Boskalis provides such an overview.

The findings of this study indicate that the HMTV fleet represents a particularly promising option for the adoption of WASP. The modelling results, supported by insights from the literature, show that rotor sail installations have the potential to reduce fuel consumption and associated emissions under representative operating conditions. For Boskalis, this implies that the current fleet configuration may be overlooking an opportunity to achieve measurable reductions in both operational costs and environmental impact. Implementing WASP on a heavy marine transport vessel would also extend the application of these technologies beyond the merchant shipping sector, where most existing installations are currently concentrated. Demonstrating successful integration on a special-purpose vessel could lower the barrier to adoption, both within Boskalis and across the broader offshore and heavy-transport industries, by providing a concrete example. More broadly, the results underline that the feasibility of WASP should not be considered exclusive to traditional merchant vessels; other vessel types may also offer favourable conditions for achieving meaningful fuel and emission reductions.

8.3. Future research

For more accurate performance predictions, a transition toward at least a 3-DoF model (level II in Figure 2.17) would ultimately be necessary. Such an approach, however, requires significantly more detailed input data. Given the age of the Triumph, it is uncertain whether sufficient data quality or availability can be achieved to justify this level of modelling effort. A more comprehensive analysis might therefore be better undertaken on a different vessel within the HMTV fleet, preferably a younger ship with more complete design and operational data, allowing greater confidence for results.

The literature review also highlighted an additional research gap that extends beyond the scope of this study: the effect of WASP on the emission characteristics of diesel engines. While this thesis assumes a

linear relationship between fuel consumption and emissions, a present study indicates dynamic engine loading due to WASP, which may influence in-cylinder conditions, and consequently, the formation of emissions. A deeper understanding in this field would improve the accuracy of emission estimates and contribute to more comprehensive evaluations of WASP technologies.

While WASP may be a solution to decrease fuel consumption and pollutant emissions, this innovation plays a small role in the global energy transition. Research on technologies and innovations that improve the overall energy efficiency of the maritime sector, which may apply to ship design, ship structures, marine engineering, ship hydromechanics, or operations management, must be sustained, and application of these should be expanded. The industry could reduce its environmental footprint through continuous development, testing, and adoption of these innovations. This will meet increasingly stringent international regulations and contribute to a cleaner future.

References

Airfoil Tools. (2025). *NACA 0015*. Retrieved August 5, 2025, from http://airfoiltools.com/airfoil/details?airfoil=naca0015-il

BAR Technologies. (2025). *BAR Technologies – Simulation driven marine innovation*. BAR Technologies. https://www.bartechnologies.uk/

Bertram, V. (2012). *Practical ship hydrodynamics* (2nd ed). Elsevier/Butterworth-Heinemann.

Bethwaite, F. (2008). *Higher Performance Sailing: Faster Handling Techniques* (1st ed). Bloomsbury Publishing Plc.

Boskalis. (2025). *Fleet and equipment*. Retrieved May 8, 2025, from https://boskalis.com/about-us/fleet-and-equipment

Boskalis. (2026a). *Boskalis AI*. https://ai.boskalis.com/

Boskalis. (2026b). *Emissions*. Retrieved February 24, 2026, from https://boskalis.com/sustainability/environmental-and-social/emissions

Boskalis. (2026c). *Internal data*.

Buitendijk, M. (2020). *First voyage for ship equipped with Ventifoil wind-assist system*. SWZ Maritime. https://swzmaritime.nl/news/2020/02/19/first-voyage-for-ship-equipped-with-ventifoil-wind-assist-system/

Buitendijk, M. (2023). *VIDEO: Pyxis Ocean sets sail with two WindWings fitted*. SWZ Maritime. https://swzmaritime.nl/news/2023/08/21/video-pyxis-ocean-sets-sail-with-two-windwings-fitted/

Buitendijk, M. (2024a). *Boskalis commissions new cable-laying vessel Boka Ocean*. SWZ Maritime. https://swzmaritime.nl/news/2024/02/26/boskalis-commissions-new-cable-laying-vessel-boka-ocean/

Buitendijk, M. (2024b). *Jumbo equips heavy-lift vessel with Econowind sails*. SWZ Maritime. https://swzmaritime.nl/news/2024/09/18/jumbo-equips-heavy-lift-vessel-with-econowind-sails/

Butcher, J. C. (2000). Numerical methods for ordinary differential equations in the 20th century. *Journal of Computational and Applied Mathematics*, *125*(1), 1–29. https://doi.org/10.1016/S0377-0427(00)00455-6

Cargo Vessels International. (2010). *Triumph*. https://www.cargo-vessels-international.at/MARBLE_IMO8902967.pdf

Carlton, J. (2018). *Marine propellers and propulsion*. Butterworth-Heinemann.

Charlou, M., Babarit, A., & Gentaz, L. (2023). A new validated open-source numerical tool for the evaluation of the performance of wind-assisted ship propulsion systems (N. Moës & E. Guilmineau, Eds.). *Mechanics & Industry*, *24*, 26. https://doi.org/10.1051/meca/2023026

Charrier, B., Constans, J., Cousteau, J.-Y., Daïf, A., Malavard, L., & Quinio, J.-L. (1985). Fondation Cousteau and windship propulsion 1980 – 1985 system Cousteau. *Journal of Wind Engineering and Industrial Aerodynamics*, *20*(1–3), 39–60. https://doi.org/10.1016/0167-6105(85)90011-X

Chica, M., Hermann, R. R., & Lin, N. (2023). Adopting different wind-assisted ship propulsion technologies as fleet retrofit: An agent-based modeling approach. *Technological Forecasting and Social Change*, *192*, 122559. https://doi.org/10.1016/j.techfore.2023.122559

Chisnell, M. (1992). *Chisnell on instrument techniques*. Thomas Reed Publications.

de Vos, P. (2015). *Design of a New Ship Propulsion System Fundamentals course* [Accepted author manuscript]. https://pure.tudelft.nl/ws/files/132924793/Design_of_a_new_Ship_Propulsion_System_fundamentals_course_final_version.pdf

DNV. (2025). *How WAPS can help to comply with GHG regulations* (White paper). Retrieved May 22, 2025, from https://www.dnv.com/maritime/publications/waps-white-paper-download/

Econowind. (2025). *Why wind? | Wind Power*. https://econowind.nl/why-wind/

Econowind. (2026). *Econowind main page*. Retrieved February 25, 2026, from https://econowind.nl/

Eggers, R. (2016). Operational performance of wind assisted ships. *Proc. 10th Symposium on High-Performance Marine Vehicles (HIPER)*. https://www.marin.nl/en/publications/operational-performance-of-wind-assisted-ships

FinOcean. (2024). *WASP market update* (Presentation). https://www.ama-andros.gr/wp-content/uploads/2024/09/Market-Update-on-WASP-August-2024.pdf

Google. (2026). *NotebookLM*. Google NotebookLM. https://notebooklm.google/

HANSA. (2024). *First Chinese rotor sail system goes into operation*. https://hansa.news/first-chinese-rotor-sail-system-goes-into-operation/

Heywood, J. (2018). *Internal combustion engine fundamentals*. McGraw-Hill Education.

Holtrop, J., & Mennen, G. (1982). An approximate power prediction method. *International Shipbuilding Progress*, *29*(335), 166–170. https://doi.org/10.3233/ISP-1982-2933501

Hüllein, A. S. (2022). *Evaluating the Potential and Viability of Wind-Assisted Ship Propulsion (WASP) for Vessels in the Norwegian Aquaculture Industry* [Master's thesis, NTNU]. https://ntnuopen.ntnu.no/ntnu-xmlui/handle/11250/3021061

IMO. (2013). *Guidance on Treatment of Innovative Energy Efficiency Technologies for Calculation and Verification of the Attained EEDI* (MEPC.1/Circ.815).

IMO. (2017). *Historic Background*. Retrieved February 24, 2026, from https://www.imo.org/en/ourwork/environment/pages/historic%20background%20ghg.aspx

IMO. (2020). *Fourth IMO GHG Study*. https://www.imo.org/en/ourwork/environment/pages/fourth-imo-greenhouse-gas-study-2020.aspx

IMO. (2024). *Reduction of GHG emissions from ships* (MEPC 81/INF.39). https://www.wind-ship.org/archived-site/wp-content/uploads/2023/01/MEPC-81-INF.39-White-paper-on-wind-propulsion-Comoros-France-Solomon-IWSA.pdf
White paper on wind propulsion.

IWSA. (2025, April). *Vessel List*. Retrieved August 25, 2025, from https://www.wind-ship.org/vessel-list/

IWSA. (2026). *Market Intelligence*. IWSA. Retrieved February 24, 2026, from https://www.wind-ship.org/market-intelligence/

Journée, J. M. J., & Massie, W. W. (2008). *Offshore Hydromechanics*. Delft University of Technology.

Khan, L., Macklin, J., Peck, B., Morton, O., & Souppez, J.-B. R. G. (2021). A Review Of Wind-Assisted Ship Propulsion For Sustainable Commercial Shipping: Latest Developments And Future Stakes: Wind Propulsion Conference. *Proceedings of the Wind Propulsion Conference 2021*. https://doi.org/10.3940/rina.win.2021.05

Kisjes, A. (2017). *Wind Propulsion for Merchant Vessels* [Master's thesis, TU Delft]. https://repository.tudelft.nl/record/uuid:a681c8e6-552e-45a1-8657-893123a8e06b

Klein Woud, J., & Stapersma, D. (2002). *Design of propulsion and electric power generation systems*. IMarEST.

KNMI. (2026). *Windschaal van Beaufort*. https://www.knmi.nl/kennis-en-datacentrum/uitleg/windschaal-van-beaufort

Kolodziejski, M., & Sosnowski, M. (2025). Review of Wind-Assisted Propulsion Systems in Maritime Transport. *Energies*, *18*(4), 897. https://doi.org/10.3390/en18040897

Kramer, J., Sverre Steen, & Luca Savio. (2016). Drift Forces – Wingsails vs Flettner Rotors. *High-Performance Marine Vehicles*. https://www.researchgate.net/publication/308674535_Drift_Forces_-_Wingsails_vs_Flettner_Rotors

Kuo, T. (2020). *Dynamic Simulation of a Wind Assisted Ship Propulsion System and its Time Domain and Frequency Domain Analysis* [Master's thesis, TU Delft]. https://repository.tudelft.nl/record/uuid:767d77ad-d7da-4586-b239-a54ed5009567

Lade, T. (2022). *Vindskip is the world's greenest deep-sea car carrier | Business Norway*. Business Norway. https://businessnorway.com/solutions/vindskip-the-worlds-greenest-deep-sea-car-carrier

Laursen, R., Patel, H., Sofiadi, D., Zhu, R., Nelissen, D., van Seters, D., & Pang, E. (2023). *Potential of wind-assisted propulsion for shipping* (EMSA/OP/43/2020). European Maritime Safety Agency. https://www.emsa.europa.eu/publications/item/5078-potential-of-wind-assisted-propulsion-for-shipping.html

Leijendeckers, P., & Beke, C. (2004). *Poly-technisch zakboek* (Versie 2004). Reed Business Information.

Lele, A., & Rao, K. V. S. (2016). Ship propulsion strategies by using wind energy. *2016 International Conference on Emerging Technological Trends (ICETT)*, 1–6. https://doi.org/10.1109/ICETT.2016.7873693

Lisitsin, O. (2020). *Aircraft Wing Design Process: From Ailerons to Flaps*. Engre. https://engre.co/blogs/articles/from-ailerons-to-flaps-the-main-stages-of-design-of-an-aircraft-wing/

LR. (2024). *Applying wind-assisted propulsion to ships* (Energy Efficiency Retrofit Report 2024). https://www.lr.org/en/knowledge/research-reports/2024/applying-wind-assisted-propulsion-to-ships/

Lu, R., & Ringsberg, J. W. (2020). Ship energy performance study of three wind-assisted ship propulsion technologies including a parametric study of the Flettner rotor technology. *Ships and Offshore Structures*, *15*(3), 249–258. https://doi.org/10.1080/17445302.2019.1612544

Lv, J., Lin, Y., Zhang, R., Li, B., & Yang, H. (2022). Assisted Propulsion Device of a Semi-Submersible Ship Based on the Magnus Effect. *Polish Maritime Research*, *29*(3), 33–46. https://doi.org/10.2478/pomr-2022-0023

MAN Diesel. (2009). *Load-up program* (Service Letter No. SL09-503/JAP). https://www.man-es.com/docs/default-source/service-letters/sl2009-503.pdf?sfvrsn=2b95b1dc_4

MAN Energy Solutions. (2009). *MAN B&W S70MC6* (Project guide No. 198 66 92-7.0). https://engine.od.ua/ufiles/MAN-S70mc6.pdf

MARIN. (2025). *Blue Route*. Retrieved September 10, 2025, from https://blueroute.application.marin.nl/

Microsoft. (2026). *Chat | M365 Copilot*. https://m365.cloud.microsoft/chat/?auth=2

Norsepower. (n.d.). *Norsepower Rotor Sail Solution* (Brochure). https://www.scribd.com/document/358708934/Norsepower-General-Brochure-1

Norsepower. (2026). *Norsepower main page*. Retrieved February 25, 2026, from https://www.norsepower.com/

NumPy. (2026). *Numpy.trapezoid*. https://numpy.org/devdocs/reference/generated/numpy.trapezoid.html

OceanWings. (2026). *Wind Assisted Propulsion Systems*. Retrieved January 5, 2026, from https://www.oceanwings.com

OrcaFlex. (2026). *Wind spectra*. Retrieved February 2, 2026, from https://www.orcina.com/webhelp/OrcaFlex/Content/html/Windspectra.htm

Patowary, K. (2021). *Flettner Rotor: Sailing Ships Without Sails*. Amusing Planet. https://www.amusingplanet.com/2021/02/flettner-rotor-sailing-ships-without.html

Plessas, T., & Papanikolaou, A. (2025). Multi-Objective Optimization of Ship Design for the Effect of Wind Propulsion. *Journal of Marine Science and Engineering*, *13*(1), 167. https://doi.org/10.3390/jmse13010167

Prof. Dr. Ir. Kuiper, G. (2003). *Resistance and propulsion*. TU Delft.

Rakopoulos, C. D., Dimaratos, A. M., Giakoumis, E. G., & Rakopoulos, D. C. (2009). Evaluation of the effect of engine, load and turbocharger parameters on transient emissions of diesel engine. *Energy Conversion and Management*, *50*(9), 2381–2393. https://doi.org/10.1016/j.enconman.2009.05.022

Rakopoulos, C. D., & Giakoumis, E. G. (2009). *Diesel Engine Transient Operation*. Springer London. https://doi.org/10.1007/978-1-84882-375-4

Reche-Vilanova, M., Bingham, H. B., Psaraftis, H. N., Fluck, M., & Morris, D. (2023). Preliminary Study on the Propeller and Engine Performance Variation with Wind Propulsion Technologies. *Wind Propulsion Conference*. https://orbit.dtu.dk/en/publications/preliminary-study-on-the-propeller-and-engine-performance-variati

Reche-Vilanova, M., Hansen, H., & Bingham, H. B. (2021). Performance Prediction Program for Wind-Assisted Cargo Ships. *Journal of Sailing Technology*, *6*(01), 91–117. https://doi.org/10.5957/jst/2021.6.1.91

Reid, E. G. (1924). *Tests of Rotating Cylinders* (Technical notes No. NACA-TN-209). NACA. Langley Memorial Aeronautical Laboratory. https://ntrs.nasa.gov/api/citations/19930080991/downloads/19930080991.pdf

Schot, J. J. A., & Eggers, R. (2019). The Effect of Leeway Angle on the Propeller Performance. *Wind Propulsion*. https://doi.org/10.3940/rina.win.2019.04

SciPy. (2026a). *Scipy.integrate.solve_ivp*. https://docs.scipy.org/doc/scipy/reference/generated/scipy.integrate.solve_ivp.html

SciPy. (2026b). *Scipy.interpolate.RegularGridInterpolator*. https://docs.scipy.org/doc/scipy-1.16.2/reference/generated/scipy.interpolate.RegularGridInterpolator.html

Seddiek, I. S., & Ammar, N. R. (2021). Harnessing wind energy on merchant ships: Case study Flettner rotors onboard bulk carriers. *Environmental Science and Pollution Research*, *28*(25), 32695–32707. https://doi.org/10.1007/s11356-021-12791-3

Shi, W. (2013). *Dynamics of Energy System Behaviour and Emissions of Trailing Suction Hopper Dredgers* [Doctoral dissertation, TU Delft]. https://repository.tudelft.nl/record/uuid:e613a11d-65bd-4ce0-bbb9-6821cc455de3

Smeets, M. (2024). *VentoFoil Adoption Model* [Master's thesis, TU Delft]. https://repository.tudelft.nl/record/uuid:61556e5d-987c-46aa-9c3c-4b7bfe74f339

Stapersma, D., & Vrijdag, A. (2017). Linearisation of a ship propulsion system model. *Ocean Engineering*, *142*, 441–457. https://doi.org/10.1016/j.oceaneng.2017.07.014

Taherdoost, H., & Madanchian, M. (2023). Multi-Criteria Decision Making (MCDM) Methods and Concepts. *Encyclopedia*, *3*(1), 77–87. https://doi.org/10.3390/encyclopedia3010006

The Engineering ToolBox. (2003). *Air Density, Specific Weight, and Thermal Expansion Coefficients at Varying Temperatures and Pressures*. Retrieved November 3, 2025, from https://www.engineeringtoolbox.com/air-density-specific-weight-d_600.html

Thies, F., & Ringsberg, J. W. (2021). Performance Prediction and Design of Wind-Assisted Propulsion Systems. *International Conference on Wind Propulsion*. https://doi.org/10.3940/rina.win.2021.06

Tillig, F., & Ringsberg, J. W. (2019). A 4 DOF simulation model developed for fuel consumption prediction of ships at sea. *Ships and Offshore Structures*, *14*, 112–120. https://doi.org/10.1080/17445302.2018.1559912

Tillig, F., & Ringsberg, J. W. (2020). Design, operation and analysis of wind-assisted cargo ships. *Ocean Engineering*, *211*, 107603. https://doi.org/10.1016/j.oceaneng.2020.107603

Tillig, F., Ringsberg, J. W., Psaraftis, H. N., & Zis, T. (2020). Reduced environmental impact of marine transport through speed reduction and wind assisted propulsion. *Transportation Research Part D: Transport and Environment*, *83*, 102380. https://doi.org/10.1016/j.trd.2020.102380

Traut, M., Gilbert, P., Walsh, C., Bows, A., Filippone, A., Stansby, P., & Wood, R. (2014). Propulsive power contribution of a kite and a Flettner rotor on selected shipping routes. *Applied Energy*, *113*, 362–372. https://doi.org/10.1016/j.apenergy.2013.07.026

van Lammeren, W., van Manen, J., & Oosterveld, M. (1969). The Wageningen B-Screw Series. *The Society of Naval Architects and Marine Engineers, Annual Meeting*. https://www.marin.nl/en/publications/the-wageningen-b-screw-series

van der Kolk, N. (2020). *Sailing Efficiency and Course Keeping Ability of Wind Assisted Ships* [Doctoral dissertation, Delft University of Technology]. https://doi.org/10.4233/UUID:8707309F-B9A3-4E09-916D-8FB64328A138

Vance, J., Woodward, J., Stilwell, J., & Davies, E. (2026). Ship. In *Encyclopedia Brittanica*. https://www.britannica.com/technology/ship

Viken, W. H. (2022). *A method for evaluating the potential for retrofitting Wind Assisted Ship Propulsion from a ship owner perspective* [Master's thesis, NTNU]. https://ntnuopen.ntnu.no/ntnu-xmlui/handle/11250/3021064

Viola, I. M., Sacher, M., Xu, J., & Wang, F. (2015). A numerical method for the design of ships with wind-assisted propulsion. *Ocean Engineering*, *105*, 33–42. https://doi.org/10.1016/j.oceaneng.2015.06.009

Wartsila. (2026). *Wake fraction coefficient*. WÄRTSILÄ Encyclopedia of Marine and Energy Technology. Retrieved January 25, 2026, from https://www.wartsila.com/encyclopedia/term/wake-fraction-coefficient

Werner, S., Trodden, D., Alterskjær, A., Eggers, R., Kim, Y., Yuling, G., Zhang, X., & Kume, K. (2024). Report of the Wind Powered and Wind Assisted Ships Committee. *ITTC*, *1*. https://ittc.info/media/12050/00-cover-vol1.pdf

Whitcomb, C. A. (1998). Naval Ship Design Philosophy Implementation. *Naval Engineers Journal*, *110*(1), 49–63. https://doi.org/10.1111/j.1559-3584.1998.tb02385.x

A

Fleet analysis: vessel subdivision

Type	Subtype	Name	Length (m)	Service speed (kn)
Backhoe dredger	Small	HH 47	30.0	7.0
	Medium	Kreeft	52.0	9.0
		Zeekoe	56.4	6.0
	Large	Aquila	85.9	9.0
Crane vessel	Vessel	Bokalift 1	216.0	12.5
		Bokalift 2	231.0	11.0
		Giant 7	137.0	12.5
	Crane barge	Taklift 7	72.6	7.0
		Asian Hercules III	106.4	7.0
		Asian Hercules II	91.4	7.0
Cutter dredger	Small	Cyrus ii	107.0	11.5
		Ursa	105.4	11.3
		Taurus II	112.6	11.0
	Large	Helios	152.0	11.5
		Krios	152.0	11.5
Diving support vessel	Offshore	Komodo	70.9	10.0
		Kamara	70.9	13.5
		Boka Atlantis	115.4	11.0
		Boka Da Vinci	115.4	11.0
		Boka Polaris	113.6	10.0
	Inland	Falcon	20.0	5.3
		Jan van Gent	41.5	9.5
		Smit Ranger	12.9	17.0
Subsea rock installation vessel		Rockpiper	158.6	12.0
		Seapiper	147.2	11.5
		Seahorse	162.0	13.0

Type	Subtype	Name	Length (m)	Service speed (kn)
Hopper dredger	Small	Deo-Gloria	70.8	8.4
		Sospan Dau	72.8	8.0
		Shoalway	90.0	11.0
		Strandway	92.1	11.0
		Causeway	92.1	11.0
		Coastway	97.7	12.5
		Waterway	97.7	12.5
		Shoreway	97.5	13.0
		Crestway	97.5	13.0
		Freeway	92.1	11.0
	Medium	Medway	121.3	11.5
		Beachway	120.4	11.5
		Gateway	143.5	15.4
		Willem van Oranje	143.5	15.4
	Large	Oranje	201.0	15.4
		Queen of NL	230.7	16.0
		Fairway	230.7	16.0
		Prins der Nederlanden	201.0	15.4
Multi-purpose	Small	Ndurance	99.0	11.5
		Ndeavor	99.0	9.7
		Spirit	90.0	9.0
		Boka Atlantic	115.4	10.0
	Medium	Boka Pride	130.0	10.0
		Sea1 Spearfish	120.9	10.0
		Sub C	138.5	10.0
Multipurpose tugs	Supply tug	Manta	75.5	12.0
		Nicobar	70.9	9.0
		Bear	73.5	10.0
	Construction tug	Boka Pioneer	82.2	10.0
		Boka Falcon	93.4	10.0
		Boka Fulmar	93.4	10.0
Ocean going tugs	Small	Union Topaz	33.0	10.0
		Union Onyx	33.0	10.0
		Terramare 1	30.1	11.0
		Wrestler	40.7	9.0
		Fighter	40.7	9.0
		Warrior	40.7	10.0
		Boxer	40.7	9.0
	Large	Boka Glacier	75.0	11.0
		Boka Summit	75.0	11.0
		Boka Expedition	75.0	11.0
		Boka Alpine	75.0	11.0
		Boka Sherpa	75.0	11.0
		Princess	67.4	10.0
		Sovereign	67.4	12.0
Supply vessel		Boka Southern Ocean	133.6	11.0
		Boka Topaz	106.6	11.0
		Boka Tiamat	98.1	11.0

Type	Subtype	Name	Length (m)	Service speed (kn)
Semi-sub HMTV		Boka Vanguard	275.0	14.5
		Mighty Servant 3	181.2	15.0
		Blue Marlin	224.8	13.0
		Forte	216.8	14.0
		White Marlin	216.7	14.5
		Black Marlin	217.8	14.5
		Transshelf	173.0	15.5
		Target	216.8	15.0
		Trustee	216.8	15.0
		Triumph	216.8	15.0
Survey vessel	Other	Ocean Endeavour	77.1	8.0
		Ocean Observer	80.4	8.0
		Kommandor	68.5	8.0
	Drilling	Gard Horizon	75.0	9.0
		Horizon Geodiscovery	83.9	10.0
		Horizon Geobay	87.0	10.0
		Horizon Geodrill	81.6	10.0
		Horizon Prospector	78.3	10.0
		Ocean Reliance	85.4	8.0
		Ocean Resolution	79.2	8.5
		Ocean Vantage	68.0	9.0
		Quest Horizon	65.0	10.0
		Kommandor Susan	83.7	10.0
	Crane/a-frame	Braveheart Spirit	73.2	10.0
		Horizon Nomad	60.0	10.0
		Horizon Zenith	68.0	10.0
		RV Ocean Researcher	69.4	8.0
		Horizon Surveyor	40.2	10.0
		Ocean Geograph	73.0	10.0

B

MCDA

Score: 0-4	Effectiveness				Operational interference				FOM
Ship type and subtype	Sailing speed	Free airflow	Sailing time	Wind conditions	Free deck space	Manoeuvrability	Height restriction	Versatility impact	Total
Weight	4	4	4	4	2	2	2	2	
Hopper dredgers - small	2	2	3	3	1	1	1	3	52
Hopper dredgers - medium	2	2	3	3	1	1	2	3	54
Hopper dredgers - large	1	2	3	2	2	3	2	3	52
Cutter dredger - small	2	0	1	2	0	1	2	2	30
Cutter dredger - large	2	0	1	2	0	1	3	2	32
Backhoe dredger - small	4	2	1	1	1	1	3	2	46
Backhoe dredger - medium	4	3	1	1	3	2	2	2	54
Backhoe dredger - large	3	3	1	1	1	2	3	0	44
Semi sub HMTV	1	4	3	2	4	4	4	0	64
Multi-purpose tugs - construction	3	1	2	2	1	1	0	0	36
Multi-purpose tugs - supply	3	1	2	2	1	1	0	0	36
Ocean going tugs - small	3	1	2	2	3	1	0	0	40
Ocean going tugs - large	2	2	3	2	3	1	0	0	44
Crane vessel - barge	4	0	2	2	0	1	4	0	42
Crane vessel - vessel	2	3	2	2	1	2	4	0	50
Subsea rock installation vessel	2	3	3	2	2	2	3	3	60
Diving support vessel - offshore	2	1	2	2	1	1	2	0	36
Diving support vessel - inland	3	1	2	1	1	1	1	0	34
Supply vessel	2	1	2	2	1	1	2	0	36
Survey vessel - crane/a-frame	3	2	2	2	1	1	2	0	44
Survey vessel - drilling	3	1	2	2	1	1	4	2	48
Survey vessel - other	4	2	2	2	2	1	2	2	54
Multi purpose - small	3	2	2	2	1	2	3	0	48
Multi purpose - medium	3	2	2	2	1	2	3	0	48

C

MCDA results

FOM	Normalised FOM	Ship name
64	1.00	Semi sub HMTV
60	0.94	Subsea rock installation vessel
54	0.84	Hopper dredgers — medium
54	0.84	Backhoe dredger — medium
54	0.84	Survey vessel — other
52	0.81	Hopper dredgers — small
52	0.81	Hopper dredgers — large
50	0.78	Crane vessel — vessel
48	0.75	Survey vessel — drilling
48	0.75	Multi purpose — small
48	0.75	Multi purpose — medium
46	0.72	Backhoe dredger — small
44	0.69	Backhoe dredger — large
44	0.69	Ocean going tugs — large
44	0.69	Survey vessel — crane/a-frame
42	0.66	Crane vessel — barge
40	0.62	Ocean going tugs — small
36	0.56	Multi—purpose tugs — construction
36	0.56	Multi—purpose tugs — supply
36	0.56	Diving support vessel — offshore
36	0.56	Supply vessel
34	0.53	Diving support vessel — inland
32	0.50	Cutter dredger — large
30	0.47	Cutter dredger — small